

THE NATURAL MODE SHAPES AND FREQUENCIES
OF GRAPHITE/EPOXY CANTILEVERED PLATES AND SHELLS

by

EDWARD FRANCIS CRAWLEY

S.B., Massachusetts Institute of Technology
(1976)

SUBMITTED IN PARTIAL FULFILLMENT
OF THE REQUIREMENTS FOR THE
DEGREE OF MASTER OF SCIENCE


at the

MASSACHUSETTS INSTITUTE OF TECHNOLOGY

June, 1978

© Edward Francis Crawley 1978

Signature of Author 
Department of Aeronautics and Astronautics
April 19, 1978

Certified by  Thesis Supervisor

Accepted by  Chairman, Departmental Graduate Committee

Archives
MASSACHUSETTS INSTITUTE
OF TECHNOLOGY

JUL 6 1978

LIBRARIES

THE NATURAL MODE SHAPES AND FREQUENCIES
OF GRAPHITE/EPOXY CANTILEVERED PLATES AND SHELLS

by

Edward Francis Crawley

Submitted to the Department of
Aeronautics and Astronautics on April 19, 1978
in partial fulfillment of the requirements for
the degree of Master of Science.

ABSTRACT

The natural mode shapes and frequencies of graphite/epoxy and graphite/epoxy/aluminum cantilevered plates and cylindrical shell sections are investigated. A single assumed mode partial Ritz analysis is used to determine the frequencies of orthotropic cantilever plates. The results suggest a method for preliminary design and frequency nondimensionalization. The assumed stress hybrid shell element RS40 which includes the effects of transverse shear is used to model a set of laminated cantilevered plates and shells. When this set of plates and shells was then built and tested, the frequencies predicted by RS40 showed reasonable agreement with experimental values, and the predicted and observed mode shapes were in excellent agreement.

Thesis Supervisor: James W. Mar
Title: Professor of Aeronautics
and Astronautics

Acknowledgement

The author would like to express his deep appreciation to Professor J. W. Mar for his support and help throughout this work, and for his understanding and instruction in the area of composite materials. To Professor T.H.H. Pian for his advice and interest in finite element analysis, and to Professor J. Dugnudji for his encouragement and help the author extends his gratitude.

Acknowledgement must also be given to Dr. S. W. Lee, the author of element RS40, without whose contribution this work would not have been possible. The author is also grateful to Professor J. Kerrebrock for his wise advice and support, and for supplying the motivation for this work.

Special thanks must go to three undergraduates in the Department of Aeronautics and Astronautics, Laura Dugan, Dwight Shih and Marc Regelbrugge for their craftsmanship and skill in the fabrication of the test specimens used, and to A. R. Shaw for his tremendous practical advise and experience. The author also thanks Ms. N. Ivey for her help in typing the manuscript.

The author wishes to acknowledge the support of the Fannie and John Hertz Foundation for their graduate fellowship. This work was also supported by the U.S. Air Force Materials Laboratory under Contract No. F33615-77-C-5155 with

Dr. Steven Tsai as Technical Monitor, and by the Office of Scientific Research under Contract No. AFOSR-77-3335 with Mr. Narendra S. Khot as Technical Monitor.

When as in silk my Julia goes,
Then, then, me thinks, how sweetly flows
The liquefaction of her clothes.

Next, when I cast mine eyes, and see
That brave vibration, each way free
O, how that glittering taketh me!

Robert Herrick

(1591 - 1674)

or

Midnight shakes the memory
As a madman shakes a dead geranium.

T. S. Eliot

TABLE OF CONTENTS

<u>Chapter No.</u>		<u>Page No.</u>
1	Introduction	9
2	Partial Ritz Analysis for Frequency Determination	11
3	Finite Element Analysis	23
4	Experimental Equipment and Procedures	35
5	Comparison of Experimental and Finite Element Results	41
6	Conclusions	47
 <u>Appendices</u>		
A	Material Properties	49
B	Cure Cycles	50
 <u>References</u>		51

LIST OF TABLES

<u>Table No.</u>		<u>Page No.</u>
1	Comparison of the Frequencies Calculated Using MLP3K and RS40 with Ritz Solutions	52
2	Frequencies Calculated Using RS40 for a 3" x 3" x .0416" Plate	53
3	Frequencies Calculated Using RS40 for a 6" x 3" x .0816" Hybrid Plate	54
4	Calculated and Observed Frequencies of Aluminum Plates	55
5	Calculated and Observed Frequencies of 3" x 3" 8-PLY Graphite/Epoxy Plates	56
6	Calculated and Observed Frequencies of 6" x 3" 8-PLY Graphite/Epoxy Plates	57
7	Calculated and Observed Frequencies of 6" x 3" Graphite/Epoxy/Aluminum Plates	58
8	Calculated and Observed Frequencies of 6" x 3" Cylindrical Shell Sections	59
9	Observed Frequencies Compared to Frequencies Calculated Using Original and Modified Material Properties	60

LIST OF ILLUSTRATIONS

<u>Figure No.</u>		<u>Page No.</u>
1	Typical Specimen Tested	61
2	Flow Diagram for Program "Shell Vibes"	62
3	Convergence Curves for RS40 and MLP3K	63
4	Experimental Test Setup	64
Mode Shapes for the Following Plates:		
5-9	Aluminum 3" x 3"	65-69
10-14	$[0_2/\pm 30]_s$ 3" x 3"	70-74
15-19	$[0/\pm 45/90]_s$ 3" x 3"	75-79
20-24	$[\pm 45/\mp 45]_s$ 3" x 3"	80-84
25-29	Aluminum 6" x 3"	85-89
30-34	$[0_2/\pm 30]_s$ 6" x 3"	90-94
35-39	$[0/\pm 45/90]_s$ 6" x 3"	95-99
40-44	$[\pm 45/\mp 45]_s$ 6" x 3"	100-104
45-49	$[0_4/A1]_s$ 6" x 3"	105-109
50-54	$[0/\pm 45/90/A1]_s$ 6" x 3"	110-114
55-59	$[\pm 45/\mp 45/A1]_s$ 6" x 3"	115-119
Mode Shapes for the Following Cylindrical Shell Sections with Radius of Curvature 5":		
60-64	$[0_2/\pm 30]_s$ 6" x 3"	120-124
65-69	$[0/\pm 45/90]_s$ 6" x 3"	125-129
70-74	$[\pm 45/\mp 45]_s$ 6" x 3"	130-134

CHAPTER I

INTRODUCTION

Advanced composite materials and in particular Graphite/Epoxy are finding increasing use in aerospace vehicles including rotary wing aircraft, high performance fighters and the space shuttle.¹ Among their advantages they give to the designer the ability to tailor the elastic and aeroelastic characteristics of a structure without changing its physical dimensions. Such tailoring is now being considered in the design of high aspect ratio wings,² and of gas turbine compressor and fan blades.³ In some cases this tailoring takes the form of shifting one or several of the natural frequencies of a structure. In other cases the change is desired in a given mode shape or deflection.

This study will investigate the natural mode shapes and frequencies of laminated cantilever plates and cylindrical shell sections, which can be thought of as being representative of fan blades and low aspect ratio wings (Fig. 1). The purposes of this study are to develop a simple method for understanding the vibratory behavior of laminated plates which can be used to make preliminary design estimates and which can serve as a basis for nondimensionalizing test data. The second goal is to model the laminated plates and shell more exactly using the assumed stress hybrid finite shell element RS40, and to investigate the effects of transverse shear stiffness on the

natural frequencies using this element. The final goal is to build a set of laminated plates and shells and test them for natural frequency and mode shape to check the accuracy of the finite element analysis.

In Chapter II the free vibration of a specially orthotropic cantilevered plate is analyzed using a single assumed mode partial Ritz analysis. A form of the solution is derived which expresses the bending and torsional frequencies of orthotropic plates in terms of plate stiffnesses and known values for the frequencies of isotropic plates. The form of the solution is then extended to chordwise frequencies, and is suggested as a basis for the nondimensionalization of finite element and experimental data.

Chapter III discusses the finite element analysis performed using two separate elements; an assumed stress hybrid shell element RS40 and a multilayered plate element MLP3K. The software used to implement these elements, as well as their convergence properties and frequency results are presented. The frequencies are nondimensionalized using the method of Chapter II, and correlated to the isotropic frequencies.

The selection and fabrication of the test articles are presented in Chapter IV, along with the experimental techniques and procedures used. Finally in Chapter V the experimental and finite element results are compared and discussed.

CHAPTER II

Partial Ritz Analysis for Frequency Determination2.1 Motivation

Before beginning either a detailed finite element analysis or an actual design of a laminated cantilevered plate it would be desirable to have some feel for the effect of ply stacking sequence and orientation on the mode shapes and frequencies. Ideally this could be done by an exact solution of the governing partial differential equation, but since the exact solution for the natural modes of a specially orthotropic plate have been found only for plates with 2 or 4 sides simply supported, we must use an approximate method. In this case a Partial Ritz (also called Kantorovich method)⁴ technique will be used which assumes a mode shape only in the chordwise direction, thus reducing the governing partial differential equation to an ordinary differential equation. By using only one assumed mode, the approximate form and functional dependence of the frequencies will be determined.

2.2 Partial Ritz Analysis

We will consider the transverse vibration of a uniform specially orthotropic cantilever plate representative of a symmetric laminated plate with no bending-twisting coupling ($D_{16} = D_{26} = 0$). Under these conditions the strain energy and kinetic energy are given as:⁵

$$V = \frac{1}{2} \iint_A \left\{ D_{11} \left(\frac{\partial^2 w}{\partial x^2} \right)^2 + 2D_{12} \frac{\partial^2 w}{\partial x^2} \frac{\partial^2 w}{\partial y^2} + D_{22} \left(\frac{\partial^2 w}{\partial y^2} \right)^2 + 4D_{66} \left(\frac{\partial^2 w}{\partial x \partial y} \right)^2 \right\} dA \quad (2.1)$$

$$T = \frac{1}{2} \iint_A \bar{\rho} h \left(\frac{\partial w}{\partial t} \right)^2 dA \quad (2.2)$$

Applying Hamilton's principle and letting the harmonic displacements of free vibration take the form

$$w(t) = w \sin \omega t \quad (2.3)$$

we find the following equilibrium condition for free vibration:

$$\pi = \frac{1}{2} \iint_A \left\{ D_{11} \left(\frac{\partial^2 w}{\partial x^2} \right)^2 + 2D_{12} \left(\frac{\partial^2 w}{\partial x^2} \frac{\partial^2 w}{\partial y^2} \right) + D_{22} \left(\frac{\partial^2 w}{\partial y^2} \right)^2 + 4D_{66} \left(\frac{\partial^2 w}{\partial x \partial y} \right)^2 - \omega^2 \bar{\rho} h w^2 \right\} dA = \text{stationary value} \quad (2.4)$$

Let us assume a single mode in the chordwise direction, so that the displacement everywhere can be written:

$$w(x, y) = \bar{w}(x) + y \theta(x) \quad (2.5)$$

where Eq. 2.5 approximately represents the bend and twist of a prismatic bar. Substituting the assumed mode shape into the

equilibrium expression (Eq. 214) yields:

$$\pi = \frac{1}{2} \int_0^l \int_{-\frac{c}{2}}^{\frac{c}{2}} \{ D_{11} (\bar{w}'' + y\theta'')^2 + 4D_{66} (\theta')^2 - \omega^2 \bar{\rho} h (\bar{w} + y\theta)^2 \} dy dx = \text{stationary value} \quad (2.6)$$

Note that the stiffnesses D_{22} and D_{12} have been eliminated because no curvature is allowed in the chordwise (y) direction. Performing the integration in the y direction, it is convenient to define the following integrals, the limits of integration of which go from $-c/2$ to $c/2$:

$$\begin{aligned} a_1(x) &= \int D_{11} dy & \omega^2 m_1(x) &= \int \omega^2 \bar{\rho} h dy \\ a_2(x) &= \int D_{11} y dy & \omega^2 m_2(x) &= \int \omega^2 \bar{\rho} h y dy \\ a_3(x) &= \int D_{11} y^2 dy & \omega^2 m_3(x) &= \int \omega^2 \bar{\rho} h y^2 dy \\ a_4(x) &= \int D_{66} dy & & \end{aligned} \quad (2.7)$$

For a plate symmetric about the mid chord point ($y = 0$) which is our case, $a_2 = m_2 = 0$ (Fig. 1). In this case the expression for the potential energy reduces to:

$$\pi = \frac{1}{2} \int_0^l \{ a_1 (\bar{w}'')^2 + a_3 (\theta'')^2 + 4a_4 (\theta')^2 - \omega^2 m_1 \bar{w}^2 - \omega^2 m_3 \theta^2 \} dx = \text{stationary value} \quad (2.8)$$

Applying the variation principle to Eq. 2.8 such that

$$\delta\pi = 0 \quad (2.9)$$

Performing the required integration by parts, and gathering like terms, we end up with:

$$\begin{aligned} \delta\pi = & \int_0^{\ell} \{ [a_1 \bar{w}'''' - m_1 \omega^2 \bar{w}] \delta \bar{w} \\ & + [a_3 \theta'''' - 4a_4 \theta'' - \omega^2 m_3 \theta] \delta \theta \} dx \\ & + [a_1 \bar{w}'''] \delta \bar{w}' \Big|_0^{\ell} - [a_1 \bar{w}'] \delta w \Big|_0^{\ell} \\ & + [a_3 \theta'''] \delta \theta' \Big|_0^{\ell} - [a_3 \theta'' - 4a_4 \theta'] \delta \theta \Big|_0^{\ell} = 0 \end{aligned} \quad (2.10)$$

which yield the governing uncoupled ordinary differential equations and boundary conditions for a plate unsupported along $y = \pm \frac{c}{2}$. In the case of a uniform plate clamped at $x = 0$ and free at $x = \ell$, the appropriate equations and boundary conditions are:

$$D_{11} c \bar{w}'''' - \omega^2 \bar{\rho} h c \bar{w} = 0 \quad (2.11)$$

$$D_{11} \frac{c^3}{12} \theta'''' - 4D_{66} c \theta'' - \omega^2 \bar{\rho} h \frac{c^3}{12} \theta = 0 \quad (2.12)$$

Boundary conditions at $x = 0$

$$\delta \bar{w} = \delta \bar{w}' = 0 \quad \delta \theta = \delta \theta' = 0 \quad (2.13)$$

at $x = \ell$

$$w'' = w''' = 0$$

$$\theta'' = (D_{11} \frac{c^3}{12} \theta''' - 4D_{66} c \theta') = 0 \quad (2.14)$$

Equation 2.11 can be easily recognized as being similar to the equation of vibration of a prismatic bar, differing only by a factor of $1/(1 - \nu_{12}\nu_{21})$ in the coefficient for the first term. For a laminated plate, Eq. 2.12 could be written

$$\frac{E_{11}I}{(1 - \nu_{12}\nu_{21})} \bar{w}'''' - \omega^2 m \bar{w} = 0 \quad (2.15)$$

The resulting natural frequencies as expressed in Eq. 2.11 are given as

$$\omega_n = \frac{k_n}{\ell^2} \sqrt{\frac{D_{11}}{\rho}} \quad n = 1, 2, 3, \dots \quad (2.16)$$

Here k_n is the n th eigenvalue of Eq. 2.11 subject to the boundary conditions in Eq. 2.13 and 2.14, and where $\rho = \bar{\rho}h$ in the usual notation for plates. Upon examination of Eq. 2.12,

the terms in the equation governing torsional deflections represent the warping stiffness, the St. Venant torsion stiffness ($4D_{66}c = GJ$ for an isotropic plate) and the torsional polar inertia about $y = 0$ respectively. The solution of this equation will be discussed next.

2.3 Procedure for solution of the Torsional Equation

The solution of Eq. 2.12 for the allowable values of ω is straight forward in principle. To nondimensionalize the problem, let

$$\tilde{x} = \frac{x}{\ell}$$

so that primes now indicate differentiation with respect to \tilde{x} . Now Eq. 2.12 and the associated boundary conditions Eq. 2.13 and 2.14 can be written

$$\theta'''' - b\theta'' - d\theta = 0 \quad (2.17)$$

$$\text{at } \tilde{x} = 0 \quad \delta\theta = \delta\theta' = 0 \quad (2.18)$$

$$\text{at } \tilde{x} = 1 \quad \theta'' = \theta''' - b\theta' = 0$$

where we have set

$$b \equiv 48 \frac{D_{66}}{D_{11}} \frac{\ell^2}{c^2} = 48 \frac{D_{66}}{D_{11}} AR^2 \quad (2.19)$$

$$d \equiv \frac{\omega^2 \rho l^4}{D_{11}} \quad (2.20)$$

Eqs. 2.19 and 2.17 show how the effect of the warping stiffness decreases as D_{66}/D_{11} and the plate aspect ratio increase. To solve Eq. 2.17 let

$$\theta = \theta_0 e^{p\tilde{x}} \quad (2.21)$$

Then the characteristic equation becomes:

$$p^4 - b p^2 - d = 0 \quad (2.22)$$

a quadratic in p^2 . Then we find

$$p^2 = \frac{b \pm \sqrt{b^2 + 4d}}{2} \quad (2.23)$$

Since both b and d must be positive numbers, the term $b^2 + 4d$ is always positive and greater than b , and the values for p can be given as:

$$p^2 = \frac{\sqrt{b^2 + 4d} + b}{2} = f^2 \quad (2.24)$$

$$p^2 = - \left(\frac{\sqrt{b^2 + 4d} - b}{2} \right) = -g^2$$

Then the solution for $\theta(\tilde{x})$ can be written in either of the forms:

$$\theta(\tilde{x}) = A_1 e^{f\tilde{x}} + A_2 e^{-f\tilde{x}} + A_3 e^{ig\tilde{x}} + A_4 e^{-ig\tilde{x}} \quad (2.25)$$

or

$$\begin{aligned} \theta(\tilde{x}) = & B_1 \cos g\tilde{x} + B_2 \sin g\tilde{x} \\ & + B_3 \cosh f\tilde{x} + B_4 \sinh f\tilde{x} \end{aligned} \quad (2.26)$$

To evaluate the frequencies for this assumed torsional mode, one substitutes Eq. 2.26 into the cantilever boundary conditions on θ given in Eq. 2.18, and the result is a 4 by 4 set of linear homogeneous equations of the form:

$$[H] \{B\} = \{0\} \quad (2.27)$$

Or written explicitly:

$$\begin{bmatrix} 1 & 0 & 1 & 0 \\ 0 & g & 0 & f \\ -g^2 \cos g & -g^2 \sin g & f^2 \cosh f & f^2 \sinh f \\ (g^3 + bg) \sin g & -(g^3 + bg) \cos g & (f^3 - bf) \sinh f & (f^3 - bf) \cosh f \end{bmatrix} \begin{bmatrix} B_1 \\ B_2 \\ B_3 \\ B_4 \end{bmatrix} = \begin{bmatrix} 0 \\ 0 \\ 0 \\ 0 \end{bmatrix} \quad (2.28)$$

For a given plate the value for b is known from Eq. 2.19, and f and g are related by Eq. 2.24 as:

$$f^2 = g^2 + b \quad (2.29)$$

Thus given a value of b , g is the only unknown in the \tilde{H} matrix of Eq. 2.28. The eigenvalues of Eq. 2.11 will then be those values of g which force the determinant of \tilde{H} to zero. The resulting expressions are quite lengthy and would have to be solved numerically for any practical problem. Since the assumed mode is only a rough approximation of the true behavior of the plate, the accuracy of such a result would probably be less than that predicted by a finite element or finite difference model.

However it is very instructive to look at the form that solutions to Eq. 2.28 will take. If we look at the expression resulting from the imposition of the homogeneous boundary conditions at $x = 0$ and $x = l$ in this problem, we get expressions of the form

$$g = k_n \text{ and } f = \sqrt{g^2 + b} = \sqrt{k_n^2 + b} \quad (2.30)$$

where k_n is the eigenvalue. Substituting from Eq. 2.24, 2.20 and 2.19:

$$2k_n^2 = \sqrt{\left(\frac{48D_{66}AR^2}{D_{11}}\right)^2 + \frac{4\omega^2\rho l^4}{D_{11}}} - \left(\frac{48D_{66}AR^2}{D_{11}}\right) \quad (2.31)$$

which, when solved for ω gives a relation of the form

$$\omega^2 = \frac{k_n^2}{l^2} \frac{AR^2}{\rho} \left(D_{11} \frac{k_n^2}{AR^2} + 48D_{66} \right) \quad (2.32)$$

Putting the expression in a form similar to Eq. 2.16

$$\omega_n = \frac{k_n AR}{\ell^2} \sqrt{\frac{\bar{D}_T}{\rho}} \quad (2.33)$$

$$\bar{D}_T = D_{11} \frac{k_n^2}{AR^2} + 48D_{66} \quad (2.34)$$

Thus this expression indicates that the torsional frequencies of a cantilever plate depend linearly on the aspect ratio, and upon the square root of a "weighted average" of the bending (i.e. warping) stiffness and the St. Venant torsional stiffness. Further the influence of the bending stiffness on the weighted average, \bar{D}_T , increases as the square of the model eigenvalue, and decreases as the square of the plate aspect ratio. The D_{12} stiffness does not appear in the expression for \bar{D}_T due to the choice of a chordwise mode shape which excludes chordwise bending. If a more exact solution of the problem were found, one might expect the constants in Eq. 2.34 to change and perhaps the effects of D_{12} to be included, but the general form of Eq. 2.34 and 2.33 would remain unchanged.

The roughly linear dependence of ω_n on aspect ratio is well born out by more complete Ritz analysis and by experimentation for isotropic cantilever plates.⁶ We will return to the exact dependence of \bar{D}_T for orthotropic plates after the presentation of finite element analysis results in Chapter III.

2.4 Generalization of the Frequency

Nondimensionalization Scheme

Equations 2.16 and 2.33 strongly suggest that the natural frequencies of a cantilever orthotropic plate can be correlated to its bending stiffnesses D_{11} , D_{12} , etc, by use of the well known expression for frequencies of free vibration of a plate

$$\omega_n = \frac{k_n}{\ell^2} \sqrt{\frac{D_a}{\rho}} \quad (2.35)$$

where now D_a is interpreted as the "appropriate" bending stiffness for the mode in question. We have seen that for bending $D_a = D_{11}$, the plate stiffness in the bending direction. For torsion however, $D_a = \bar{D}_T$, a weighted average of the bending and torsion stiffnesses.

The extension of this scheme to the simple chordwise modes seems quite obvious. Here we might expect:

$$\omega_n = \frac{k_n}{\ell^2} \sqrt{\frac{D_{22}}{\rho}} \quad (2.36)$$

The "appropriate" stiffness D_a is now taken as the bending stiffness in the chordwise direction, and k_n is dependent on the aspect ratio of the plate.

The validity of these assumptions will be born out by their ability to predict the actual natural frequencies of a given laminated plate, or those predicted by finite element methods. We have however at least the basis for a scheme for

the rational nondimensionalization of the frequencies for these plates, and a starting point for the reduction of the data from the finite element analysis and experiments.

CHAPTER III

Finite Element Analysis3.1 Choice of Elements and Specimens to Model

In the selection of a finite element to use in modeling any physical system, one of the choices which must be made is in the relative sophistication of the element to be used. In the case of modeling a variable thickness doubly curved laminated wing or blade, it may be advantageous to use an element which includes transverse shear effects and allows for surface curvature. Elements of this type include the four node thick-shell quadrilateral isoparametric element QUAD 4 developed by MacNeal,⁷ and the six node thin-shell triangular isoparametric element developed by Minich.³ In this study the eight node quadrilateral element RS40 was used to model graphite/epoxy plates and shells. To serve as a basis for comparison the same structures were also modeled with a plate element MLP3K. These elements will be discussed in detail in the next section.

The choice of structures to model was largely determined by what could be fabricated and tested, and will be discussed in section 4.1. For reference at this point the samples modeled and tested included 3" x 3" flat plates of G/E and aluminum, 6" x 3" flat plates of G/E, G/E/Al, and 6" x 3" cylindrical section shells of G/E. All samples were

cantilevered (Fig. 1). The material properties used in the analysis are listed in Appendix A.

3.2 Description of Elements MLP3K and RS40

The element MLP3K is a 4 node 20 degrees of freedom constant thickness multilayered plate element. It is available in either a triangular or quadrilateral version, and is based on a moderately thick plate formulation. It has been used with good results to model both thin and moderately thick plates.⁸ In this study the quadrilateral version was used as a rectangular element to model thin ($t/c \sim 1/70$) plates. Element MLP3K uses linear interpolation of displacements on its boundaries, and is not a compatible element.

The element stiffness matrix is based on a hybrid stress model which used the modified complementary energy (πmc_1) variational principle. Since the element models a multilayer plate a stress field is assumed within each layer in terms of a standardized set of stress distribution parameters. Interlayer stress compatibility is satisfied, as are the stress boundary conditions on top and bottom surfaces. The element behavior is defined in terms of displacements u , v , w and rotations θ_x and θ_y at each node. With 4 nodes and 5 degrees of freedom (d.o.f.) per node, there are 20 element level d.o.f..

Transverse shear effects are treated in an average sense. Lines perpendicular to the mid surface remain straight but not necessarily perpendicular to the deformed midsurface. Thus θ_x

and θ_y correspond to but are not identical to $\frac{\partial w}{\partial y}$ and $\frac{\partial w}{\partial x}$.

Layer to layer cross section warping is not allowed, but overall warping is permitted based on the average transverse shear properties.

The inputs to the element consist of the ply orientation, thickness and density, as well as inplane and transverse elastic properties for each ply. The element is assumed to be uniform and of constant thickness and density.

The ply properties are assembled to form laminate properties, and the element stiffness matrix is given as an output. There are no restrictions on the laminate considered, so that unbalanced (D_{16} , $D_{26} \neq 0$) and unsymmetric ($B \neq 0$) laminates can be analyzed using MLP3K. A corresponding routine, MLP3M, uses bilinear interpolation to form a hybrid rational mass matrix which includes the effect of rotary inertia. Reference 8 contains a more detailed description of MLP3K.

The element RS40 is a moderately thick linear elastic shallow shell element. It is quadrilateral having 4 corner and 4 midside nodes, and uses quadratic interpolation of displacements on its boundaries. It can model arbitrary shallow complex curvatures and variations in thickness over the element. The element has been used to model thin and moderately thick shell structures.⁹

The element is based on the modified Hellinger-Reissner Principle (π_{MR}). It is designed to model a homogeneous material so a preprocessor must be used when RS40 is employed to

model composite structures. The inputs to the preprocessor are the ply thickness, density, orientation and elastic properties. Using a suitable lamination theory, the preprocessor calculates the elastic matrices \underline{A} , \underline{B} and \underline{D} of the laminate, the transverse shear matrices, and the translational and rotary inertia at each node. RS40 has been modified for use with laminated materials such that it accepts these values rather than just the material \underline{E} matrix. It uses the \underline{A} matrix when calculating the strain energy associated with extension, \underline{D} with bending, \underline{B} with bending stretching coupling, etc. In this way RS40 can correctly calculate the stiffness matrix of a shell composed of unbalanced (D_{16} , $D_{26} \neq 0$) or unsymmetric ($\underline{B} \neq 0$) laminate. No reduced stiffness approximation must be applied to account for the bending-stretching coupling.

As in MLP3K, transverse shear effects are handled in an average sense, with perpendiculars which remain straight but are free to twist. The nodal degrees of freedom are then u , v , w in the global x , y , z coordinates, and θ_x and θ_y about local x and y axes which are mutually orthogonal and are tangent to the shell midsurface. With 8 nodes, there are 40 element degrees of freedom.

The input to the element is now for each node: the coordinate of the node, a set of 3 direction vectors tangent and normal to the shell midsurface, the laminate elastic and inertia properties from the preprocessor, and the shell thickness.

The properties and thicknesses are interpolated biquadratically over the element. The outputs consist of the element stiffness matrix and hybrid rational mass matrix which includes the effects of rotary inertia. Note however that in its present formulation RS40 cannot model the case of a mass distribution unsymmetric about the midplane. For a more complete discussion of RS40, see Reference 9.

3.3 Finite Element Software

The software used for the analysis of cantilever plates and cylindrical shell sections using the MLP3K and RS40 elements was based on the Finite Element Analysis Basic Library, version 5 (FEABL5) developed by the Aeroelastic and Structures Research Lab at M.I.T.⁸ FEABL is a series of modular sub-routines which are linked together by the user's main program.

The flow diagram used in conjunction with RS40 is shown in Fig. 2. After initialization of variables and arrays, subroutine INPUT reads the parameters which specify the article to be modeled: ply orientation, thickness, stacking, dimensions etc; and of the solution required: grid, convergence criteria, etc. Routines SETUP and ORK are FEABL supplied housekeeping routines. LAMIN and CLT prepare the laminate properties for use by RS40 according to classical laminate theory as described in Section 3.2. RS40 then calculates element level k and m matrices, and with clamped boundary conditions applied along $y = 0$, ASEMBL creates the global K and M properties.

The resulting eigenvalue problem is solved by subroutine SSPACE using the subspace iteration method (SIM).¹⁰ The SIM technique reduces the full space problem to a representative subspace, solves the eigenvalue problem in the subspace, then recreates the full space eigenvectors.

For a problem with N unconstrained degrees of freedom, the procedure works as follows. The user specifies P , the number of eigenvectors to be included in the subspace. The value of P is chosen in the range

$$p + 3 \leq P \leq 2p \quad (3.1)$$

where p is the number of eigenvectors for which convergence is desired. The program then uses an initial guess for the set of P eigenvectors to reduce the full space \tilde{K} and \tilde{M} matrices to their subspace equivalents:

$$\tilde{k} = \tilde{U}^{(i)T} \tilde{K} \tilde{U}^{(i)} \quad \tilde{m} = \tilde{U}^{(i)T} \tilde{N} \tilde{U}^{(i)} \quad (3.2)$$

where $\tilde{U}^{(i)}$ is the $N \times P$ matrix of eigenvectors. The resulting auxiliary $P \times P$ eigenvalue problem

$$\tilde{k} \tilde{u} = \tilde{m} \tilde{u} \tilde{\zeta} \quad (3.3)$$

is solved in routine SSPACE using an iterative Jacobi diagonalization scheme. At the end of the step, the full space

eigenvectors are recomputed according to

$$\tilde{u}^{(i+1)} = \tilde{K}^{-1} \tilde{M} \tilde{u}^{(i)} \quad (3.4)$$

and the procedure is begun again with Eq.'s 3.2 using the newly computed vectors. Convergence of a mode occurs when for a given mode

$$|\lambda_j^{(i)} - \lambda_j^{(i+1)}| / |\lambda_j^{(i)}| < \epsilon \quad (3.5)$$

where the allowable tolerance parameter ϵ is specified by the user. Here the subspace eigenvalue λ_j is identical to the full space value.

Once the solution has converged, SSPACE prints the requested eigen values and vectors and returns command to main. An M.I.T. maintained subroutine CONTUR was used to contour plot the mode shapes using a line printer. The program used in conjunction with MLP3K was nearly identical to the described except that it could analyze only flat plates. Subroutine CLT was not used since MLP3K does lamination theory calculations internally.

3.4 Convergence and Accuracy

Since a study of convergence and accuracy implies that we know an exact solution to which a result should converge, all convergence studies were done modeling a flat rectangular

aluminum plate. For this problem the assumed mode shape Ritz solution's listed in Tables 4.49 and 4.52 of Reference 6 were considered the reference solutions.

In studying the grid convergence of a cantilever plate model there are two parameters, of interest, the number of elements in the spanwise (x) direction and chordwise (y) directions. Convergence of each frequency is most easily seen if one fixes the chordwise number of elements and varies the spanwise number. Families of convergence curves are then produced. Figure 3 shows two typical sets of curves, for the 2nd bending and 2nd torsion modes of a plate of aspect ratio two. For each mode the convergence for MLP3K (with 5 elements in the y direction) and RS40 (with 3 elements in the y direction) are plotted versus the total number of unconstrained degrees of freedom. Since RS40 has 8 nodes per element, and MLP3K has only 4, the total number of degrees of freedom in the y direction are roughly equivalent in these two cases.

Figure 3 demonstrates that RS40 quickly converges to a value between 1 and 2 percent below the Ritz solution. On the other hand MLP3K converges much more slowly, probably due to the linear, rather than quadratic interpolation of displacements used. In the second torsion mode MLP3K converges to a frequency about 4% less than the Ritz value, and thus represents the structure as being too soft. The plots in Fig. 3 are very representative of the other modes, and for plates of

AR = 1. In almost all cases RS40 converged more quickly to a more accurate value than did MLP3K.

The final choices for the grids used represent a tradeoff between computing accuracy and cost, and are summarized below:

ELEMENT \ PLATE	3" x 3"	6" x 3"
MLP3K	7 x 5	10 x 5
RS40	3 x 3	6 x 3

Based on their agreement with the Ritz analysis for an isotropic plate as shown in Table 1, the predicted values of frequency from MLP3K should be within $\pm 3\%$ and from RS40 within $\pm 1\%$. These grid choices were then extended to all laminate samples modeled. Isotropic cylindrical shell sections were also modeled with RS40. The results were found to be in good agreement with simple beam theory for first bending modes, and with torsion theory for torsional modes.

The only other choice left to the user is the number of modes for which convergence is desired, and the number of modes to be included in the subspace. Since convergence was desired for 5 modes, runs were made with 8, 9, and 10 in the subspace with no difference in results. In all remaining calculations 8 modes were kept in the subspace.

For many choices of grid size it became obvious that the subspace iteration produced incorrect values, high and low, for

the first bending frequency. This problem occurred more often when the ratio of the number of chordwise elements to that of elements was larger than $1/2$.

The problem was also sensitive to element aspect ratio. It is suspected that this error is due to a bad choice for the initial guess at the eigenvectors made in subroutine SSPACE. Frequency values which are thought to be incorrect are entered in the Tables in parenthesis.

From this point on, all results discussed will be those from RS40. These are largely substantiated by the MLP3K results, but the RS40 results should be more accurate.

3.5 Nondimensionalized Frequency Results

The computed frequencies from RS40 are shown in Tables 2-8, and the computed mode shapes as shown in Figures 5 to 74. The mode shapes are shown as contour plots with node lines shown by dark lines and contours of constant deflection shown by alternating bands of white and grey (characters). The clamped edge is shown at the bottom. The actual numerical frequencies will be discussed in more detail when they are compared with measured values in Chapter 5.

The scheme of "rational nondimensionalization", that is nondimensionalization of the frequency by the appropriate stiffness terms was proposed in Section 2.4. This scheme was applied to the frequencies calculated by RS40. In Tables 2 and

3 the frequencies and rationally nondimensionalized frequencies are listed for a series of laminated plates of $AR = 1$ and 2 .

After some trial and error, the scheme which gave the best results for k_n was as follows. Let ω_n be the predicted frequency, then k_n the nondimensionalized frequency is given by:

$$\omega_n = \frac{k_n}{\ell^2} \sqrt{\frac{D_a}{\rho}} \quad \text{or} \quad k_n = \omega_n \ell^2 \sqrt{\frac{\rho}{D_a}} \quad (3.6)$$

where

ℓ = length of the plate

ρ = mass per unit area

D_a = "appropriate" stiffness for the mode analyzed.

The appropriate stiffnesses were found as

$$\text{for spanwise bending: } D_a = D_{11} \quad (3.7)$$

$$\text{for chordwise bending: } D_a = D_{22} \quad (3.8)$$

for torsion:

$$D_a = \bar{D}_T = \frac{(D_{11} \frac{n^2}{AR^2} + 2D_{12} + 4D_{66})}{(\frac{n^2}{AR^2} + 2)} \quad (3.9)$$

The form of Eq. 3.7 and 3.8 are just those found in Eq. 2.16 and suggested in Eq. 2.36. The form of Eq. 3.9 is quite similar to Eq. 2.34 found from the Ritz analysis and

repeated here:

$$\bar{D}_T = D_{11} \frac{k_n^2}{AR^2} + 48D_{66} \quad (3.10)$$

Both are weighted averages of the torsion and warping stiffnesses. The term $48D_{66}$ has been replaced by the form of the coefficients from the plate bending equation, and the factor of k_n^2 has simply been replaced by the torsional mode number n ($n = 1$ for 1st torsion, 2 for second torsion, etc). The term in the denominator of Eq. 3.9 is chosen so that D_a goes to D for an isotropic plate.

The frequencies reduced by this scheme and shown in Tables 2 and 3 of very different laminates show remarkable consistency and agreement with the isotropic value. In every case listed in Tables 2 and 3 if one estimated the frequencies using Eq. 3.6 and the known isotropic value for k_n , the result would correctly predict the ranking of the frequencies (1st bending, 1st torsion, etc).

The implication of this is that using the simple relations of Eq. 3.6 through 3.9 and classical lamination theory, one can estimate the relative frequencies and approximate mode shape of almost any thin laminated cantilever plate to within about 10%. Since the lower frequencies are usually well spread out, this will usually predict the exact ranking of the natural frequencies.

CHAPTER IV

Experimental Equipment and Procedures4.1 Choice of Specimens to be Tested

In choosing what types of specimens to construct and test for comparison with finite element predictions, there were four main parameters considered: the effect of aspect ratio, of curvature, of the anisotropy of the laminate, and the effect of a sandwich or hybrid laminate.

To study the effect of aspect ratio on the accuracy of computed frequency and mode shapes, it was decided to build Graphite/Epoxy (G/E) plates of aspect ratio 1 and 2. The widest specimen that could be tested was 3 inches, so the sides were set at 3" x 3" and 6" x 3". To verify the ability of RS40 to model curved shells a set of cylindrical shell section, 6" x 3" with a radius of curvature of 5" were tested. In many practical problems, Graphite/Epoxy is not used alone, but is bonded to a substructure. To simulate this case a set of 6" x 3" Graphite/Epoxy/Aluminum symmetric sandwich plates were built and tested.

In each of the above cases, the effects of the choice of laminate is of interest. In the limit one can have a laminate very stiff in bending, stiff in torsion or quasi-isotropic. After preliminary design and testing the following 8 ply laminates were chosen to represent the three cases of interest: bending stiff $[0_2/\pm 30]_S$, torsion stiff $[\pm 45/\mp 45]_S$, and quasi-isotropic $[0/\pm 45/90]_S$. The samples tested can be represented

by the matrix below, where the number indicates the sample aspect ratio:

	$[0_2/\pm 30]_S$	$[\pm/\mp 45]_S$	$[0/\pm 45/90]_S$
G/E plate	1,2	1,2	1,2
G/E shell	2	2	2
G/E/Al plate	2	2	2

In the case of the aluminum sandwich, the 8 plys were placed symmetrically about the aluminum, 4 on a side, and 0_4 replaced the $0_2/\pm 30$.

To serve as a calibration for the test procedure a set of aluminum plates of aspect ratio 1 and 2 and roughly the same thickness were built and tested.

4.2 Fabrication of the Specimens

The materials used in fabricating the specimens were primarily Graphite/Epoxy prepreg and rolled aluminum sheet.

The graphite was Hercules type AS/3501-6 taken from lot 676.

The aluminum was 2024-T3 rolled sheet nominally .040" thick.

The lay up and cure process depended on the type of sample being made. For the flat G/E plates, the prepreg was layed up as laminates roughly 12" x 14" in size. The laminate was cured in a press using the cycle listed in Appendix B, and surrounded by a symmetric arrangement of peel ply and bleeders. In the press cycle, the manufactureres temperature and pressure

cycle are approximated, but no vacuum was drawn over the laminate. After curing, specimens were cut from the laminate using a diamond coated cutting wheel.

For the Graphite/Epoxy/Aluminum sandwich specimens, the prepreg was cut to the exact size of the aluminum plate, the plate being used as a template. Six of these 6" x 3" samples were then cured at a time in the press with the graphite cocured onto the aluminum. The samples were separated during curing by resin dams which insured the resin would flow vertically and not sideways, and that the fibers would not flow around the edges of the plate. The same cure cycle was used as with the flat G/E laminates.

The cylindrical shell section specimens were layed up individually on a cylindrical tool. The lay up was directly on the surface of the tool. The laminate was surrounded by a resin dam, and peel ply and bleeders were stacked on top of the laminate only. The curved specimens were cured in an oven under vacuum using the second cycle in Appendix B. This cycle approximates the temperature and vacuum aspects of the manufacturers, but the pressure on the laminate is only about 14 psi, instead of the 100 psi that is called for.

The next step in the preparation of all the samples was to finish the edges by sanding. The edges were sanded until they were parallel, square and of the correct dimensions. The final step before the sample could be tested was to bond onto the base

a 1" x 3" loading tab. This tab was to insure that the specimen could be clamped firmly and squarely in the test jig without any damage being done to the surface fibers. The aluminum tabs were machined to size (and to the proper curvature for the curved shell specimens) and bonded to the laminates in a secondary bond using Cyanamid FM123 film adhesive at 225°F and 50 psi.

Because this bonding operation introduced a possible source of error into the test, half of the aluminum samples made had tabs bonded on in a manner identical to those on the laminated specimens. The other half were machined from a solid plate of 3/8" aluminum to the same dimensions as the bonded samples. Since no difference was found in the frequencies and mode shapes of the bonded and integral specimens, the bonded tab is assumed to introduce no noticeable error in the testing. As another check some of the samples were made symmetric about the clamp, while others extended only in one direction from the clamp. Again no significant difference was found, so the asymmetry of the specimens about the clamp is assumed to have no adverse effect on the results.

4.3 Test Apparatus and Procedures

The test apparatus is shown in Fig. 4. The specimen was clamped into a rectangular block of aluminum 1" x 6" x 6" by three 3/8" bolts tightened to a torque of 75 in#. The block was suspended by 4 spring steel flexures. The flexures allowed

the block to move perpendicular to the clamp but were very stiff in other directions. The block was rigidly attached to a Ling model 420 shaker mounted horizontally. The shaker has a peak force output of 100 lb. force. With this setup the samples could be clamped very rigidly at their base and excited along their z axis in a range from about 5 to 3000 Hz.

The moving base was instrumented with 2 Endevco model 7701-50 "Isoshear" accelerometers. One Endevco 2222B micro-ministure accelerometer was mounted on the specimen within $3/4$ " of the base and centerline. The presence of this sample mounted accelerometer was found to have less than a .2% effect on the frequency, and often no effect at all.

By monitoring the base and sample mounted accelerometers on a scope, one gets a direct indication of the amplitude and phase response of the sample. Resonances were taken as the point of 90° phase shift between the input and response accelerometers. In the case of some less strongly excited modes where a full 90° phase shift did not occur, the combination of maximum phase shift and amplitude was used to determine the resonance. The frequency data was read from a digital counter and found to be reproducible to about .2 Hz for bending modes, .5 Hz for chordwise modes and 1 Hz for torsion modes, which were only lightly excited.

The nodal pattern of a given mode was found by slowly scanning the surface with a pointed pencil eraser, while

watching the phase and amplitude response on the scope. Nodal points could be easily identified as those points which when touched had no effect on the phase or amplitude response. These points were recorded on tracing paper, and the resulting modal patterns are easily identifiable. In this way the frequency and mode shapes for the first 5 modes of all the specimens were observed and recorded.

CHAPTER V

Comparison of Experimental and Finite Element Results5.1 Frequency Results for Aluminum Plates

A total of eight aluminum plates were tested, four 3" x 3" and four 6" x 3". Since the plates varied in thickness from .04" to .05", the measured frequencies had to be corrected for this effect. From the expression for the frequency of an isotropic plate

$$\omega_n = \frac{k_n}{\ell^2} \sqrt{\frac{D}{\rho}} = \frac{k_n}{\ell^2} \sqrt{\frac{E t^3}{12(1+\nu)\bar{\rho}t}} = t \left\{ \frac{k_n}{\ell^2} \sqrt{\frac{E}{12(1+\nu)\bar{\rho}}} \right\} \quad (5.1)$$

we see the frequency depends linearly on the thickness. Using this relation the measured frequencies were normalized to a reference thickness of .0416", and averaged for each mode. The resulting values are shown in Table 4. The coefficient of variation of nominally identical specimens averaged about 1% and did not exceed 2.5% for any mode, showing that the results were fairly consistent.

The frequency results predicted by RS40 finite element analysis for an aluminum plate .0416" thick are also listed in Table 4. In comparing the measured and calculated frequencies we see that at most the two differ by 2.0% of the measured

frequency. Furthermore six of the ten modes measured for the two sizes of plates are within 0.9%. This represents quite excellent agreement between calculated and measured values.

With this good agreement for isotropic plates, we have some confidence that the frequencies measured for the laminated specimens will truly represent the cantilever frequencies, and will not be affected by any imperfection of the clamp, or by the presence of the bonded loading tab.

5.2 Frequency Results for the Laminated Plates and Shells

Thirty-seven laminated plates and shells were tested, an average of three for each configuration described in Section 4.1. In no case were more than 5 nor less than 2 of a given type tested. The 8 ply Graphite/Epoxy laminates ranged from .041" to .043" in thickness. If the manufacturer stated nominal ply thickness of .0052" is assumed, the 8 ply thickness should be .0416". Since this was the value used in the finite element analysis, the experimental results should also be normalized to this thickness. However a correction of the data to account for fiber volume effects implies a knowledge of all the ply elastic properties, and an understanding of how the ply stiffness contribute the effective stiffness of a given mode. Since neither of these are well known, the frequency data was corrected for thickness using the simple linear relationship for isotropic plates given by Eq. 5.1.

The corrected frequencies were averaged and are listed in Tables 5 to 8 for the various laminates and configurations. The results were remarkably consistent, with a coefficient of variation which averaged 1.0% and was less than or equal to 0.6% for 27 of the 60 modes measured. This consistency of results give some confidence in the workmanship and quality of specimens tested.

If the ranking of the frequencies given in Tables 5 to 8 is studied, some interesting trends can be observed. Looking at the 3" x 3" G/E plates in Table 5, we note that the "torsion stiff" laminate $[\pm 45/\bar{\pm} 45]_S$ most closely simulates the isotropic case in spacing and ranking of frequencies, while the laminate $[0/\pm 45/90]$ which is "quasi isotropic" with respect to in plane properties now has a different ranking than the aluminum, with first chordwise lower than second bending. The case is different in the 6" x 3" plates of Table 6. Here the $[0/\pm 45/90]_S$ resembles the isotropic case, while $[\pm 45/\bar{\pm} 45]_S$ has become flexible enough in bending that second bending is now lower than first torsion.

As shown in Table 7, the effect of the aluminum core in the sandwich specimens is to moderate the selective stiffening effect of the Graphite/Epoxy, and to decrease the anisotropy of the plate. Dramatic shifts in frequency and mode shape are now harder to achieve. The $[0/\pm 45/90/Al]_S$ laminate now has indeed become almost isotropic in behavior. The introduction of only

4.6% curvature (rise height/chord) has a dramatic effect on the frequencies (Table 8). The slight amount of curvature stiffens the bending modes greatly, but has only a small effect on the torsion and chordwise frequencies. First torsion has now replaced first bending as the lowest mode for the curved samples of laminates $[0/\pm 45/90]_S$ and $[0_2/\pm 30]_S$, and second bending has disappeared from the lowest five modes. The ability for composites to tailor the modal ranking and nodal structure of a cantilever with some curvature seems even greater than the effect on flat plates.

The calculated frequencies shown in Tables 5 to 8 show fair agreement with the measured values. Some values are within a few percent while others are off as much as 12%, the average error being about 6%. In every case the ranking of the modes was correct, and except for 1 value in 60, the calculated values are too high. These two facts suggest the basic material elastic constants used for in plane and/or transverse properties may be too high. The material properties used and listed in Appendix A are the design values used by the Grumman Corporation for this fiber/resin system. During the course of this study other investigators at M.I.T. using the same system and cure cycles measured material constants significantly different than those listed by Grumman. This is possible due to the inability to reproduce the manufacturer's recommended cure cycle.

The resulting uncertainty in the actual material properties of the specimens used is as great as the errors in frequency shown in Tables 5 to 8. A more realistic set of material properties was used to recalculate the frequencies in a few cases, as shown in Table 9. Here the second set of properties in Appendix A was used, which correspond more closely to those measured at M.I.T. The resulting frequencies agree more closely with the observed values. Thus the accuracy of the RS40 finite element calculations is difficult to evaluate due to the large uncertainty in material properties.

During an attempt to achieve a better prediction of the observed frequencies, the transverse shear stiffnesses were among those varied. It was observed that a 10% reduction in the transverse shear stiffness had the effect of reducing the frequencies much less than 1%. It seems that with the present treatment the softening effect of transverse shear for a thin cantilevered plate is small.

5.3 Mode Shape Results

The mode shapes as experimentally determined are shown in Figs. 5 to 74. The clamped edge is shown at the bottom, and the solid lines indicate the node lines, (i.e. the points of zero displacement). The patterns are exactly as was observed, and have not been corrected in any way. The patterns are also labeled with the number in ascending order of frequency (1st is

lowest, 5th the highest measured) and their common name (1st bending, etc).

As can be observed the agreement in the calculated and actual nodal pattern is excellent in almost all samples and modes observed.

CHAPTER VI

Conclusions6.1 Finite Element Analysis

The finite element RS40 is an effective and versatile anisotropic shell element for use in dynamic modeling. When used with a preprocessor which does laminate calculation, RS40 can be used to model laminated plates and shells of variable thickness, mass and stiffness, and with arbitrary shallow complex curvature. The element has good convergence properties, and in the isotropic case agrees with analytic and experimental results for cantilever plates.

The natural frequencies of cantilever composite plates and shells predicted by element RS40 were in reasonable agreement with the experimentally observed values. In all cases the ranking of the frequencies was correct. In view of the uncertainty in the laminate stiffness properties, it is difficult to assess the accuracy of RS40. The predicted mode shapes are in excellent agreement with the observed patterns.

6.2 Nondimensional Analysis

The approximate values and rankings of natural frequencies of laminated cantilevered plates can be determined from the known values of k_n for an isotropic plate, and the simple relation $\omega_n = (k_n / \ell^2) \sqrt{D_a / \rho}$, where D_a is the appropriate orthotropic plate stiffness for the mode in question. Using this

relation and classical lamination theory, one can make preliminary design judgements and evaluate the effect of ply orientation and stacking sequence on natural frequencies without sophisticated numerical models.

6.3 Use of Composites for Elastic Tailoring

Graphite/Epoxy composites can be used effectively to alter the natural frequencies of a plate or shell of fixed dimension, and to tailor the mode shaper to produce desirable elastic or aeroelastic properties.

6.4 Effect of Transverse Shear

Using RS40, the softening effect of transverse shear on the frequencies of a thin laminated plate were found to be small.

APPENDIX A

Material Properties

Hercules reported data for AS/3502-6

0° Tensile Modulus 20.0×10^6 psi

Design properties used in finite element calculations:

(Based on Grumman design values.)

E_L	18.5×10^6 psi
E_T	1.60×10^6
ν_{LT}	.250
G_{LT}	$.650 \times 10^6$
G_{13}	$.650 \times 10^6$
G_{23}	$.222 \times 10^6$

Modified properties used in calculating frequencies in

Table 9, and based on M.I.T. measurements:

E_L	16.0×10^6 psi
E_T	1.36×10^6
ν_{LT}	.275
G_{LT}	$.900 \times 10^6$
G_{13}	$.650 \times 10^6$
G_{23}	$.222 \times 10^6$

APPENDIX B

Cure Cycles

Cure cycle used with AS/3501-6 cured in hot press:

1. Preheat press to 275°F.
2. Place cold workpiece on press.
Apply 15 psi pressure.
3. Leave at 275°F, 15 psi 16 min.
(plates heat up to 275°F).
4. Raise temperature to 300°F. 5 min.
5. When temperature increases to 300°F
increase pressure to 100 psi.
6. Leave at 300°F, 100 psi. 30 min.
7. Raise temperature to 350°F. 10 min.
8. Leave at 350°F, 100 psi. 30 min.

Cure cycle used with AS/3501-6 cured in oven:

1. Place cold workpiece in oven.
2. Pull vacuum to 14 psi.
3. Raise temperature to 275°F. 25 min.
4. Leave at 275°F. 30 min.
5. Raise temperature to 350°F. 15 min.
6. Leave at 350°F. 60 min.
7. Turn off power, cool down in oven. 30 min.
8. Turn off vacuum, remove from oven.

References

1. Proceedings, "Third Conference on Fibrous Composites in Flight Vehicle Design," NASA TM X-3377, 1976.
2. Griffin, K. E., "An Aeroelastic Tailoring Study of a High Aspect Ratio Wing," included in proceedings, "Third Conference on Fibrous Composites in Flight Vehicle Design," NASA TM X-3377.
3. Minich, M. D., and Chamis, C. C., "Analytical Displacements and Vibrations of Cantilevered Unsymmetric Fiber Composite Laminates," NASA TM X-71699, 1975.
4. Reissner, E., and Stein, M., "Torsion and Transverse Bending of Cantilever Plates," NACA TN 2369, 1951.
5. Ashton, J. E., and Whitney, J. M., Theory of Laminated Plates, Technomic Publishing Co., Stamford, Conn., 1970.
6. Leissa, A. W., "Vibration of Plates," NASA SP-160, 1969.
7. MacNeal, R. H., "A Simple Quadrilateral Shell Element," Computers and Structures, Vol. 8, pp. 175-183, 1978.
8. Spilker, R. L., et al., "Static and Dynamic Analysis of Multilayer Composite Plates and Shells by the Hybrid-Stress Finite Element Model," Aeroelastic and Structures Research Lab Report ASRL TR181-2, M.I.T., June, 1976.
9. Lee, S. W., "Finite Element Methods for Reduction of Constraints and Creep Analysis," Ph.D. Thesis, Department of Aeronautics and Astronautics, M.I.T., February, 1978.
10. Bathe, K. J., "Convergence of Subspace Iteration," Paper presented at U.S. - Germany Symposium: "Formulations and Computational Procedures in Finite Element Analysis," M.I.T., August, 1976.

TABLE 1. COMPARISON OF THE FREQUENCIES CALCULATED
USING MLP3K AND RS40 WITH RITZ SOLUTIONS

MODE TYPE*	RITZ SOLUTION	MLP3K SOLUTION		RS40 SOLUTION	
	FREQ. (HZ)	FREQ. (HZ)	%DIFF.	FREQ. (HZ)	%DIFF.
3" x 3" x .0416" ALUMINUM					
1 1B	152.9	151.0	-1.3	152.6	-0.2
2 1T	374.0	360.4	-3.6	370.1	-1.0
3 2B	938.2	943.8	0.6	937.9	0.0
4 1C	1201.	1209.6	0.7	1193.	-0.7
5 2T	1364.	1326.7	2.7	1356.	-0.6
6" x 3" x .0416" ALUMINUM					
1 1B	38.0	37.4	-1.6	37.7	-0.8
2 1T	163.3	156.1	-4.4	161.5	-1.1
3 2B	236.4	237.0	0.3	234.3	-0.9
4 2T	532.9	512.5	-3.8	523.6	-1.7
5 3B	657.7	682.7	3.7	660.2	0.4

* HERE B-BENDING, T-TORSION, C-CHORDWISE

TABLE 2. FREQUENCIES CALCULATED USING RS40
FOR A 3" x 3" x .0416" PLATE

LAMINATE: ALUMINUM		[0 ₄] _S	[0 ₂ / ₊ 30] _S	[₋ 45/ ₊ 45] _S	[0/ ₊ 45/90] _S	[0 ₂ / ₊ 60/90] _S
MODE TYPE & FREQUENCY (HZ)	1B 152.6	1B 270.2	1B 263.3	1B 140.8	1B 225.4	1B 215.6
	1T 370.1	1T 338.6	1T 364.4	1T 500.0	1T 422.2	1T 389.4
	2B 937.9	1C 700.1	1C 762.2	2B 805.3	1C 1013.	1C 1130.
	1C 1193.	2C 1652.	2B 1655.	1C 1326.	2B 1426.	2B 1364.
	2T 1356.	2B 1704.	2C 1709.	2T 1645.	2T 1722.	2T 1640.
MODE TYPE & RATIONALLY NONDIMEN- SIONALIZED FREQUENCY $2\pi f l^2 \sqrt{\rho/D_a}$	1B 3.49	1B 3.52	1B 3.52	1B 3.26	1B 3.49	1B 3.52
	1T 8.46	1T 7.02	1T 7.32	1T 8.28	1T 7.93	1T 7.91
	2B 21.4	1C 31.0	1C 32.4	2B 18.6	1C 29.9	2B 26.4
	1C 27.3	2C 73.1	2B 22.1	1C 30.6	2B 22.1	2B 22.2
	2T 31.0	2B 22.2	2C 72.6	2T 31.3	2T 29.1	2T 29.5

TABLE 3. FREQUENCIES CALCULATED USING RS40
FOR A 6" x 3" x .0816" HYBRID PLATE

LAMINATE: ALUMINUM		[0 ₄ /Al] [*] _S		[+45/-45/Al] [*] _S		[0/+45/90/Al] [*] _S	
MODE TYPE & FREQUENCY (HZ)							
1B 73.9		1B 113.8		1B 67.3		1B 86.4	
1T 316.8		1T 229.3		2B 355.9		1T 314.6	
2B 459.5		2B 680.9		1T 380.2		2B 506.1	
2T 1027.		2T 885.8		3B 1029.		2T 1035.	
3B 1295.		1C 1168.2		2T 1187.		3B 1418.	
MODE TYPE & RATIONALLY NONDIMEN- SIONALIZED FREQUENCY							
$2\pi f l^2 \sqrt{\rho/D_a}$							
1B 3.44		1B 3.67		1B 3.58		1B 3.66	
1T 14.8		1T 14.7		2B 18.9		1T 14.7	
2B 21.4		2B 22.0		1T 14.3		2B 21.4	
2T 47.9		2T 43.1		3B 54.7		2T 47.1	
3B 60.4		1C 96.1		2T 47.6		3B 60.0	

* THICKNESS OF ALUMINUM PLY IS .040"

TABLE 4. CALCULATED AND OBSERVED FREQUENCIES
OF ALUMINUM PLATES

PLATE SIZE (LENGTH x WIDTH)	MODE	CALCULATED* FREQUENCY f_c (Hz)	OBSERVED* FREQUENCY f_0 (Hz)	%DIFF. $(f_c - f_0)/f_0$
3" x 3"	1B	152.6	153.0	-0.3
	1T	370.1	367.1	0.8
	2B	937.9	922.5	1.7
	1C	1193.	1213.	-1.7
	2T	1356.	1336.	1.5
6" x 3"	1B	37.66	37.6	0.2
	1T	161.5	158.	2.2
	2B	234.3	234.9	-0.3
	2T	523.6	518.8	0.9
	3B	660.2	658.1	0.3

* FREQUENCIES CORRECTED TO .0416" THICKNESS

TABLE 5. CALCULATED AND OBSERVED FREQUENCIES
OF 3" x 3" 8-PLY GRAPHITE/EPOXY PLATES

LAMINATE	MODE	CALCULATED FREQ. (Hz)	OBSERVED FREQ. (Hz)	%DIFF.
$[0_2/\pm 30]_S$	1B	263.3	234.2	12.4
	1T	364.4	362.	0.7
	1C	762.2	728.3	4.7
	2B	1655.	1449.	14.2
	2C	1709.	1503.	13.7
$[0/\pm 45/90]_S$	1B	225.4	196.4	14.8
	1T	422.2	418.	1.0
	1C	1013.	960.	5.5
	2B	1426.	1215.	17.4
	2T	1722.	1550.	11.1
$[\pm 45/\mp 45]_S$	1B	140.8	131.2	7.3
	1T	500.0	472.	5.9
	2B	805.3	790.5	1.9
	1C	1326.	1168.	13.5
	2T	1645.	1486.	10.7

TABLE 6. CALCULATED AND OBSERVED FREQUENCIES
OF 6" x 3" 8-PLY GRAPHITE/EPOXY PLATES

LAMINATE	MODE	CALCULATED FREQ. (Hz)	OBSERVED FREQ. (Hz)	%DIFF.
[0 ₂ /±30] _S	1B	(68.98)	58.3	(18.3)
	1T	139.1	148.	-6.0
	2B	408.7	362.7	12.7
	2T	526.0	508.	3.5
	1C	588.8	546.	7.8
[0/±45/90] _S	1B	(59.63)	48.6	(22.7)
	1T	176.3	169.	4.3
	2B	345.9	303.0	14.2
	2T	592.2	554.	6.9
	1C	820.4	739.	11.0
[±45/±45] _S	1B	(39.05)	31.3	(24.8)
	2B	192.8	185.8	3.7
	1T	229.3	214.	7.1
	3B	565.8	533.	6.2
	2T	707.6	653.	8.4

NOTE: VALUES IN PARENTHESIS ARE THOUGHT TO BE
DUE TO COMPUTATIONAL ERROR.

TABLE 7. CALCULATED AND OBSERVED FREQUENCIES
OF 6" x 3" GRAPHITE/EPOXY/ALUMINUM PLATES

LAMINATE	MODE	CALCULATED FREQ. (Hz)	OBSERVED FREQ. (Hz)	%DIFF.
$[0_4/A1]_S^*$	1B	113.8	101.7	11.9
	1T	229.3	229.	0.1
	2B	680.9	631.9	7.8
	2T	885.8	865.	2.4
	1C	1168.	1129.	3.5
$[0/\pm 45/90/A1]_S^*$	1B	86.41	75.9	13.8
	1T	314.6	302.	4.2
	2B	506.1	469.6	7.8
	2T	1035.	983.	5.3
	3B	1418.	1306.	8.6
$[\pm 45/\mp 45/A1]_S^*$	1B	67.32	58.3	15.5
	2B	355.9	351.6	1.2
	1T	380.2	358.	6.2
	3B	1029.	1006.	2.3
	2T	1187.	1113.	6.6

* THE LAMINATE CONSIST OF 4-PLIES/.040" ALUMINUM/4-PLIES

TABLE 8. CALCULATED AND OBSERVED FREQUENCIES OF
6" x 3" GRAPHITE/EPOXY CYLINDRICAL
SHELL SECTIONS

LAMINATE	MODE	CALCULATED FREQ. (Hz)	OBSERVED FREQ. (Hz)	%DIFF.
$[0_2/\pm 30]_S$	1T	169.9	161.	5.5
	1B	291.6	254.1	14.8
	1C	597.2	555.6	7.5
	2T	719.5	670.0	7.4
	2C?	834.0	794.	5.0
$[0/\pm 45/90]_S$	1T	182.2	177.	2.9
	1B	231.2	201.8	14.6
	2T	703.6	645.	9.1
	1C	809.5	754.	7.4
	?	980.1	884.8	10.8
$[\pm 45/\mp 45]_S$	1B	144.7	145.3	-0.4
	1T	248.3	222.	11.8
	2T	770.8	712.	8.3
	2B	814.1	774.2	5.2
	1C	1042.5	997.	4.6

TABLE 9. OBSERVED FREQUENCIES COMPARED TO FREQUENCIES CALCULATED
USING ORIGINAL AND MODIFIED MATERIAL PROPERTIES

(3" x 3" 8-PLY GRAPHITE/EPOXY PLATE)

LAMINATE	MODE	OBSERVED FREQ. (Hz)	ORIGINAL MAT'L PROP.		MODIFIED MAT'L PROP.	
			CALCULATED FREQ.	%DIFF. FROM OBSERVED	CALCULATED FREQ.	%DIFF. FROM OBSERVED
[0 ₂ /+30] S	1B	234.2	263.3	12.4	245.7	4.9
	1T	362.	364.4	0.7	363.6	0.4
	1C	728.3	762.2	4.7	751.8	3.2
	2B	1449.	1655.	14.2	1543.	6.5
	2C	1503.	1709.	13.7	1634.	8.7
60						
[+45/-45] S	1B	131.2	140.8	7.3	138.8	5.8
	1T	472.	500.	5.9	468.3	-0.8
	2B	790.5	805.3	1.9	813.3	2.9
	1C	1168.	1326.	13.5	1265.	8.3
	2T	1486.	1645.	10.7	1565.	5.3

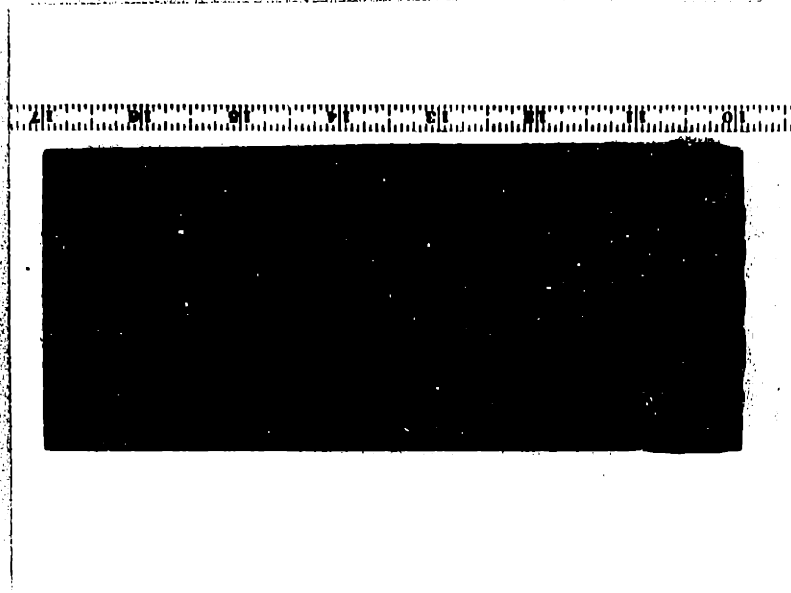
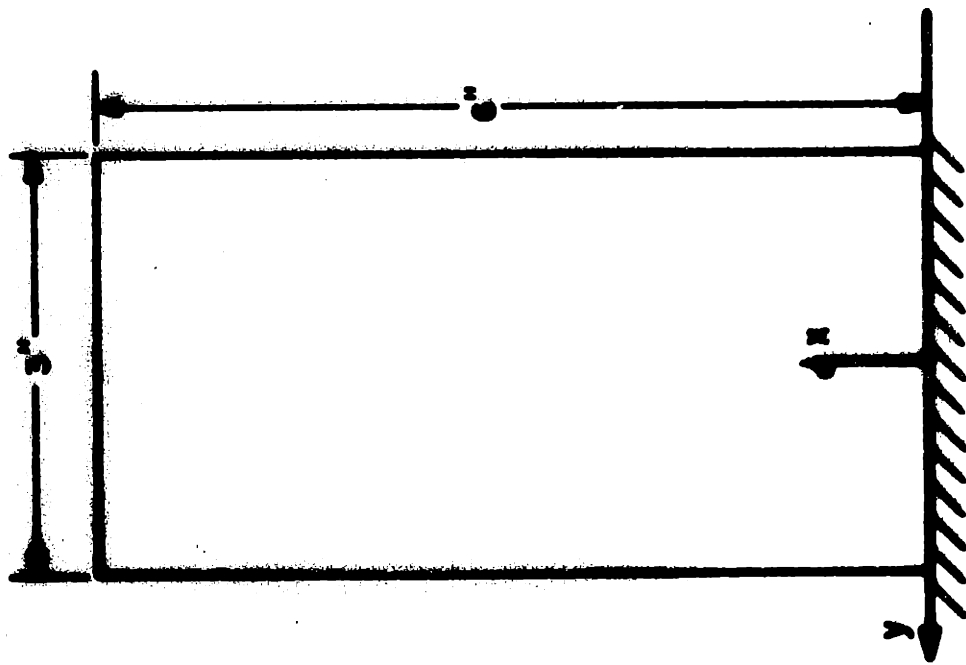


FIG. 1 TYPICAL SPECIMEN ANALYZED

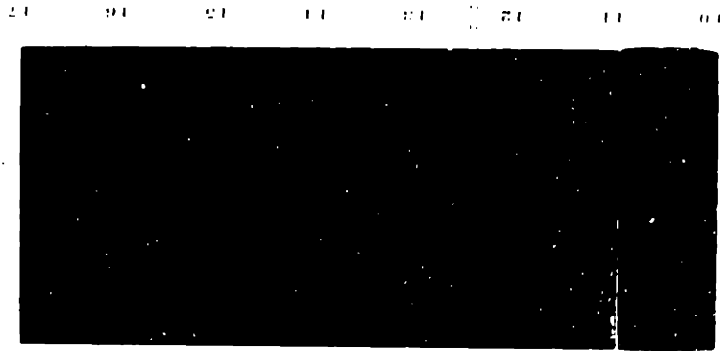
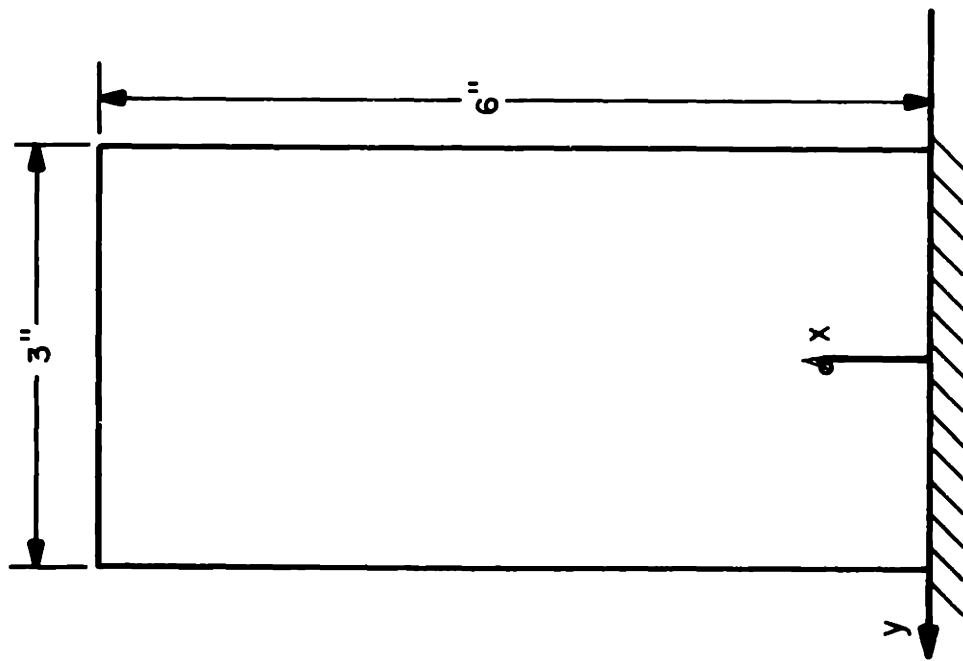
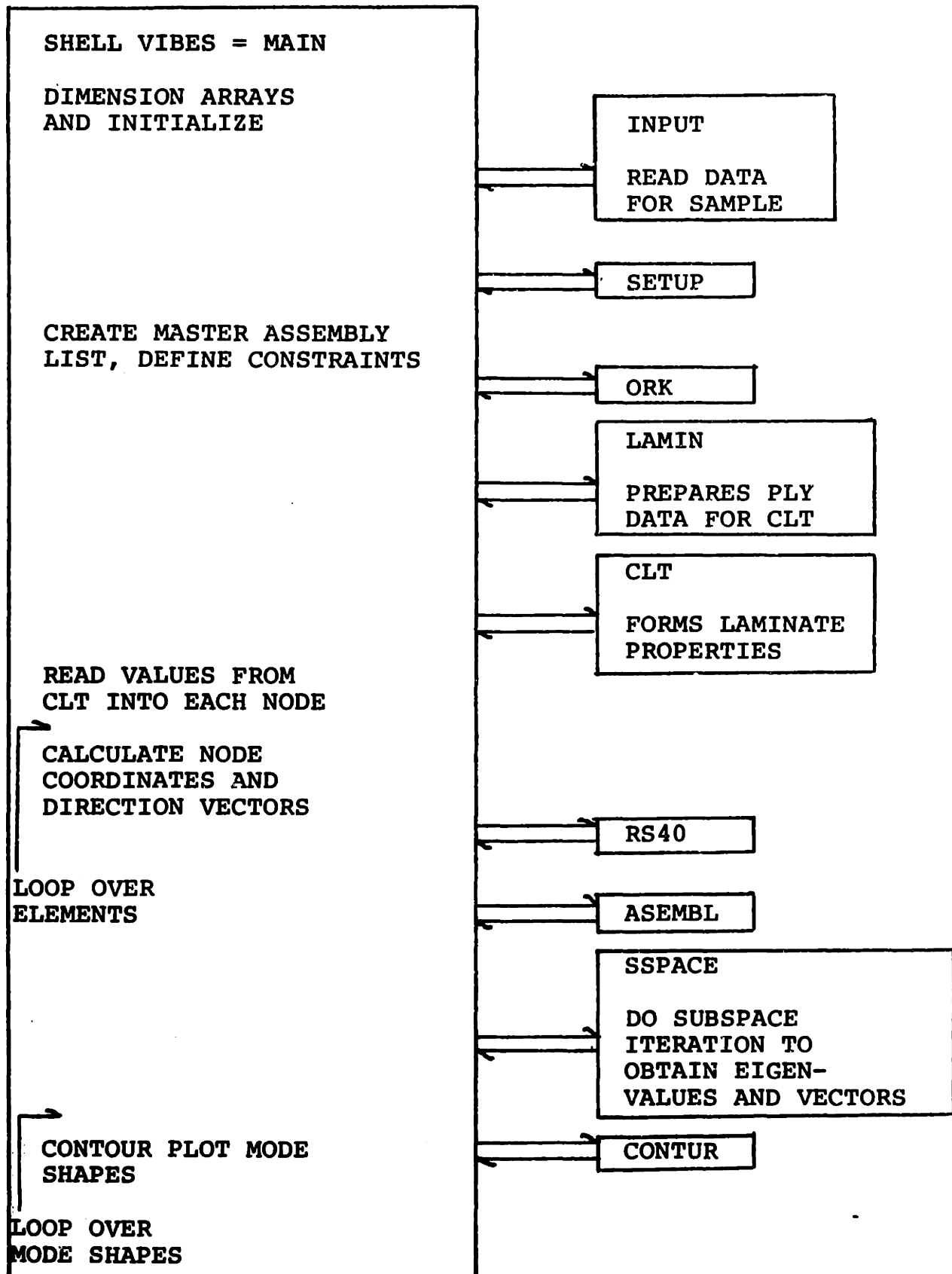
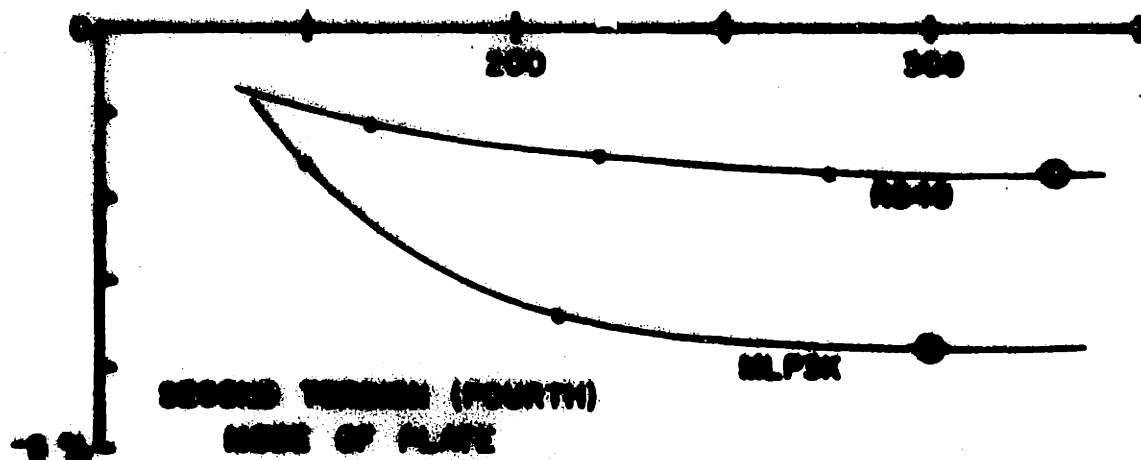
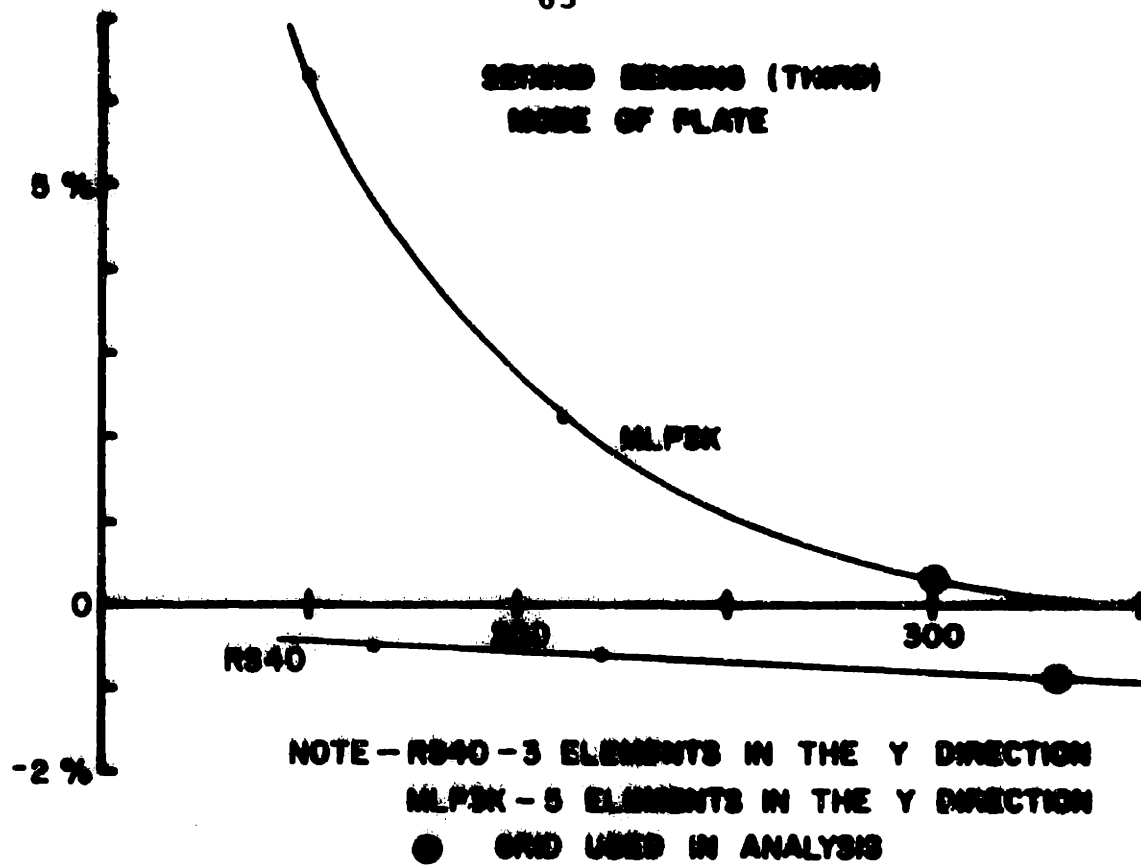


FIG. 1 TYPICAL SPECIMEN ANALYZED

FIG. 2 FLOW DIAGRAM FOR PROGRAM SHELL VIBES





**FIG. 3 PERCENT DIFFERENCE FROM
RITZ SOLUTION VS. TOTAL
NUMBER OF UNCONSTRAINED D.O.F.
FOR 6" x 3" PLATE**

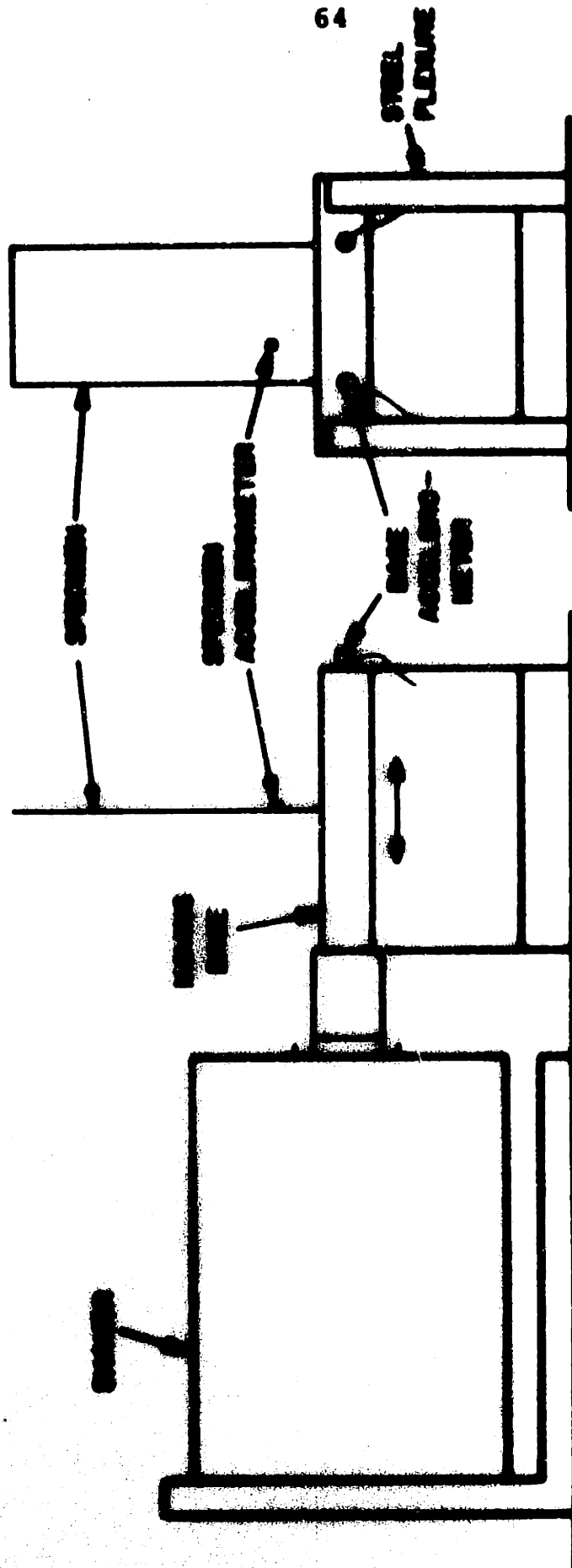
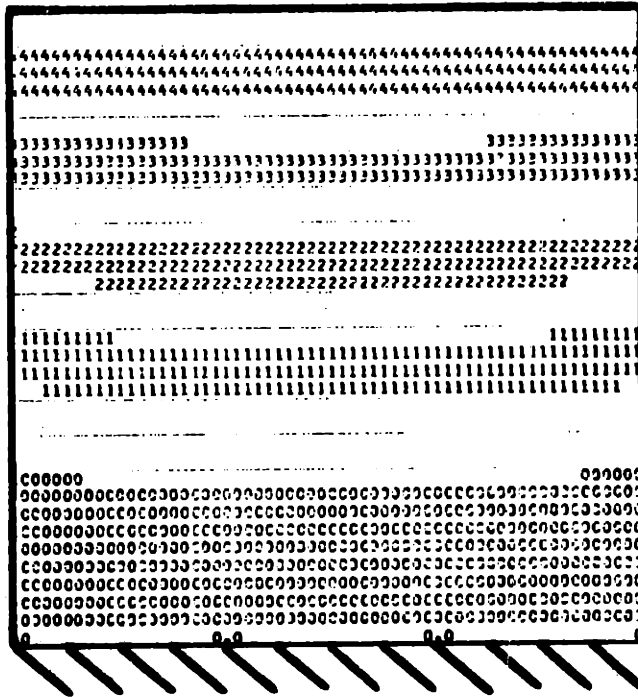
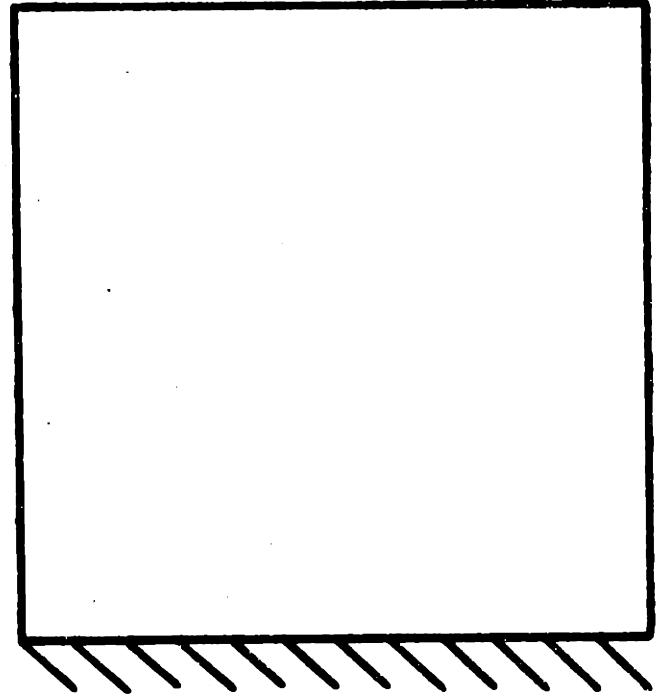


FIG. 4 EXPERIMENTAL SET-UP



CALCULATED MODE SHAPE

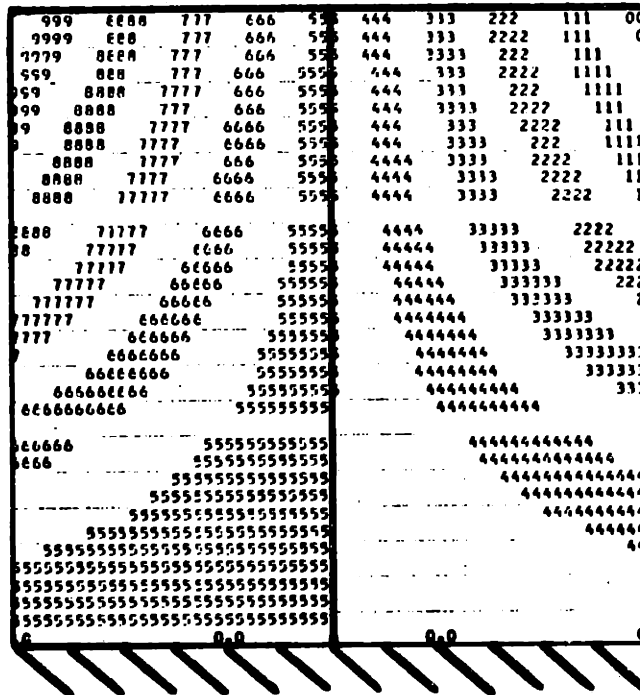
152.6 Hz



OBSERVED MODE SHAPE

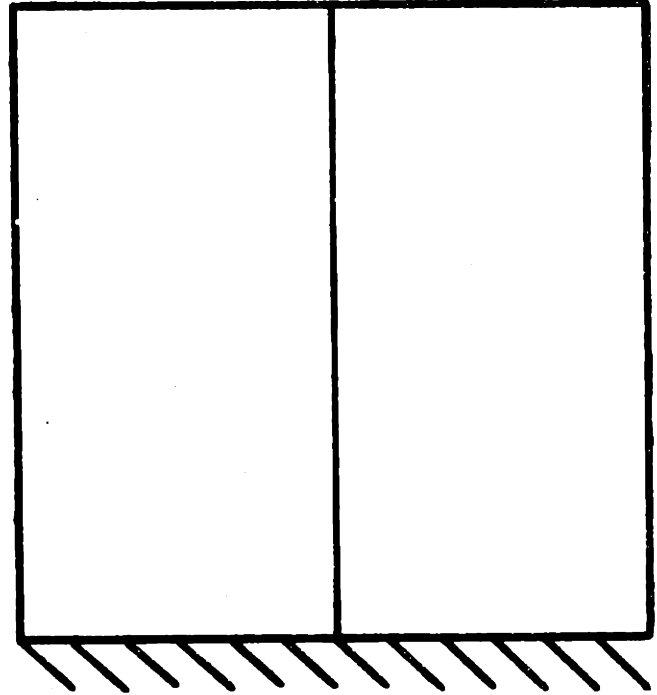
153.0 Hz

FIG. 5 1st BENDING (1st) MODE OF AN
ALUMINUM PLATE



CALCULATED MODE SHAPE

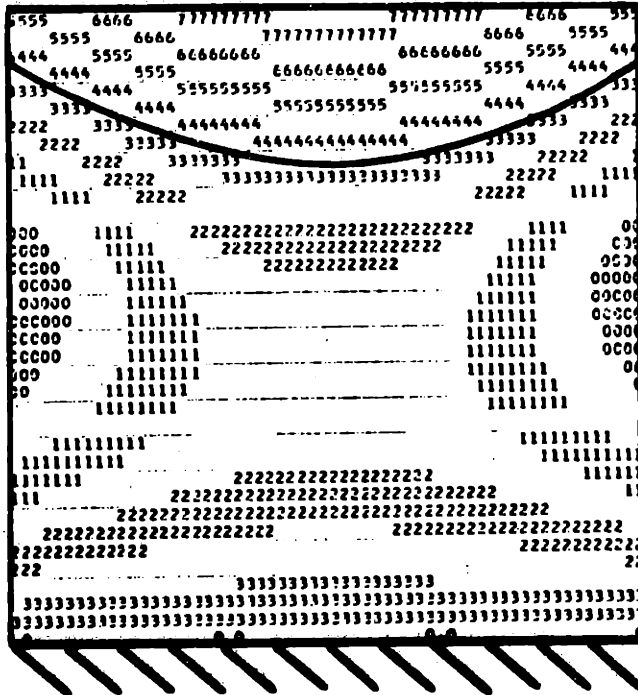
370.1 Hz



OBSERVED MODE SHAPE

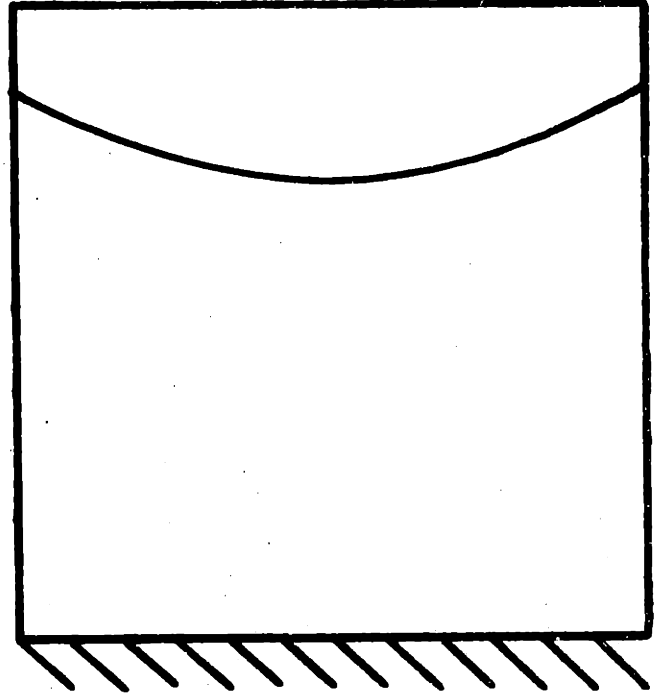
367.1 Hz

FIG. 6 1st TORSION (2nd) MODE OF AN
ALUMINUM PLATE



CALCULATED MODE SHAPE

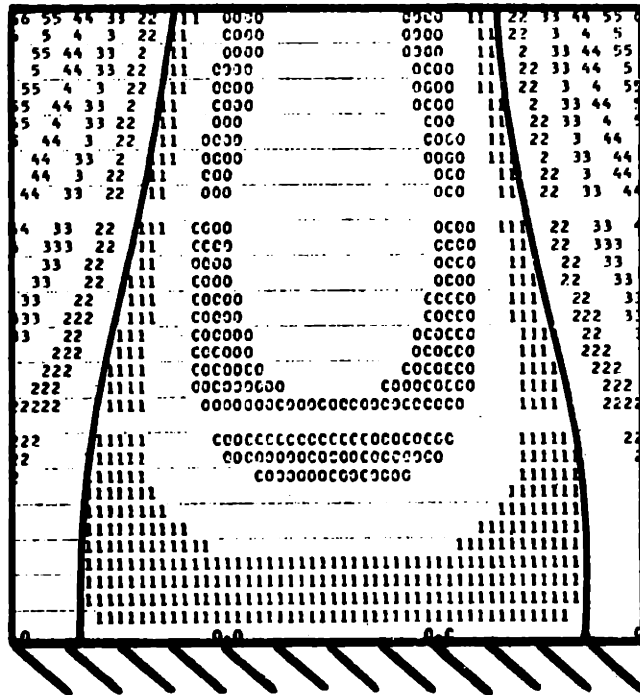
937.9 Hz



OBSERVED MODE SHAPE

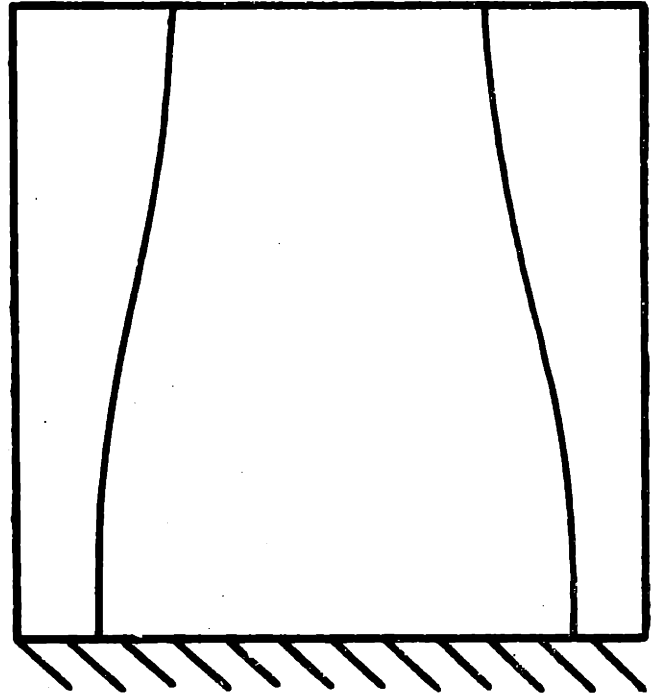
922.5 Hz

FIG. 7 2nd BENDING (3rd) MODE OF AN
ALUMINUM PLATE



CALCULATED MODE SHAPE

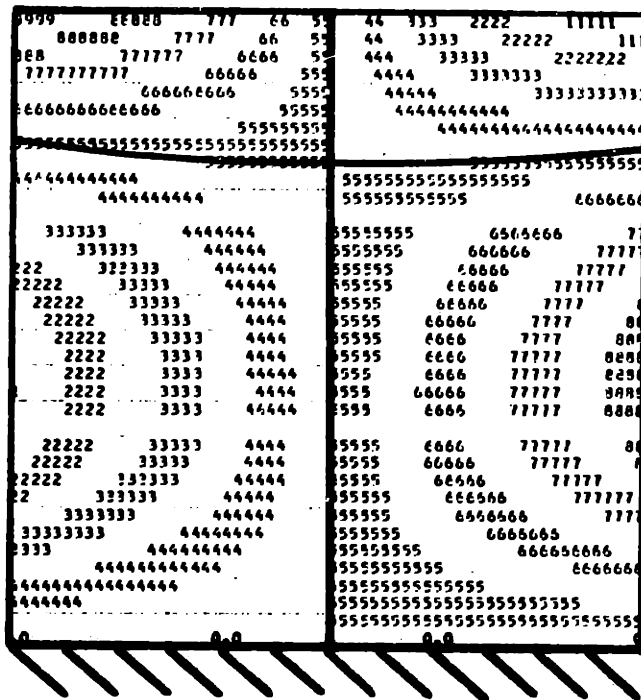
1193. Hz



OBSERVED MODE SHAPE

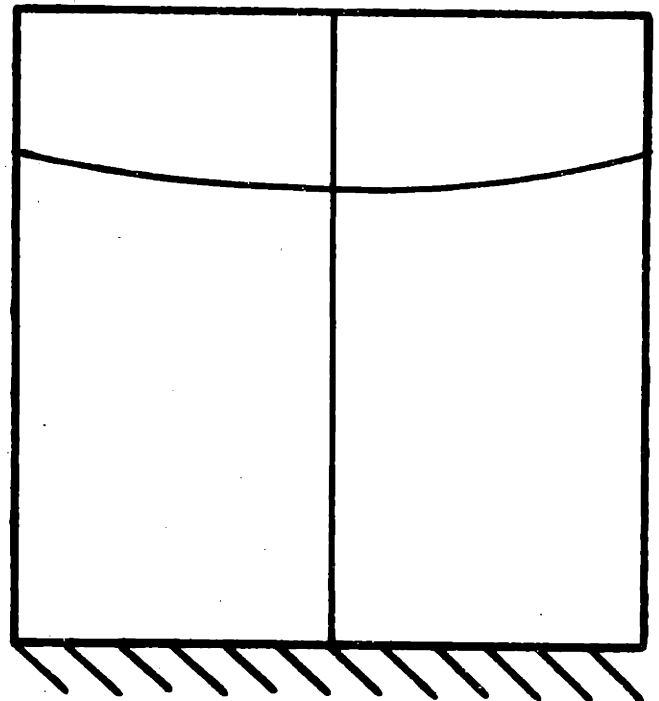
1213. Hz

FIG. 8 1st CHORDWISE (4th) MODE OF AN
ALUMINUM PLATE



CALCULATED MODE SHAPE

1356. Hz

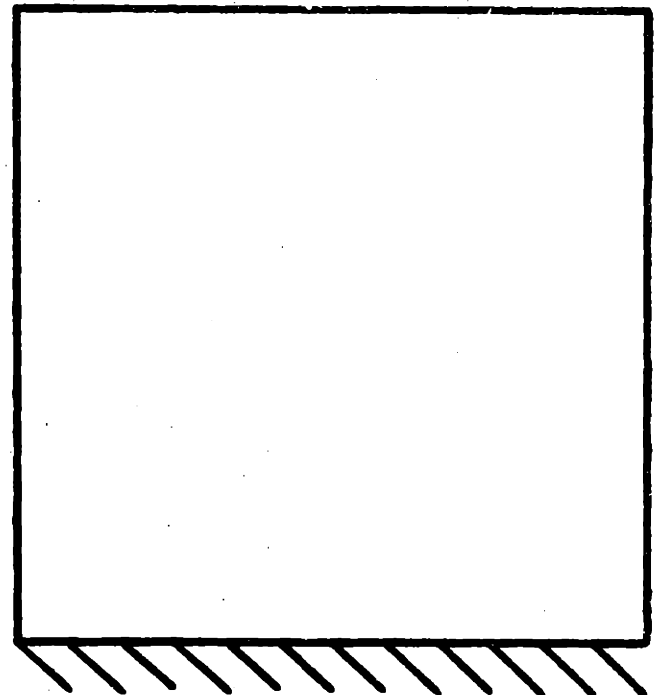


OBSERVED MODE SHAPE

1336 Hz

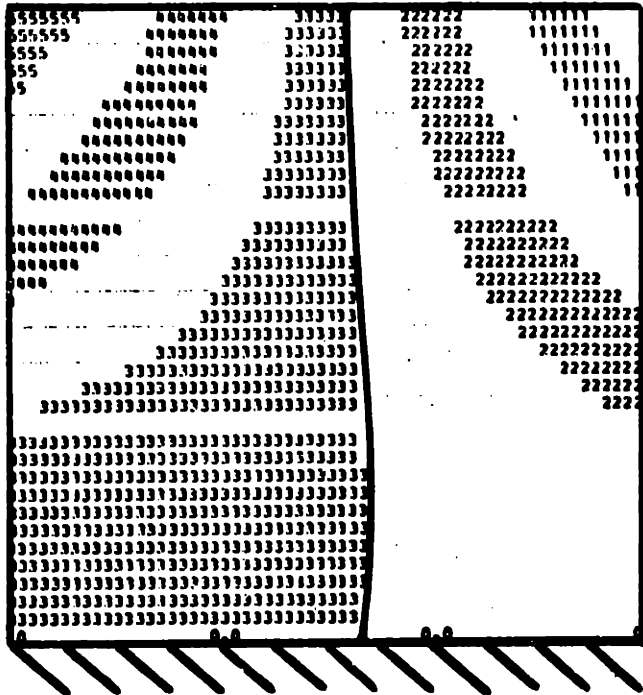
FIG. 9 2nd TORSION (5th) MODE OF AN
ALUMINUM PLATE

263.3 Hz



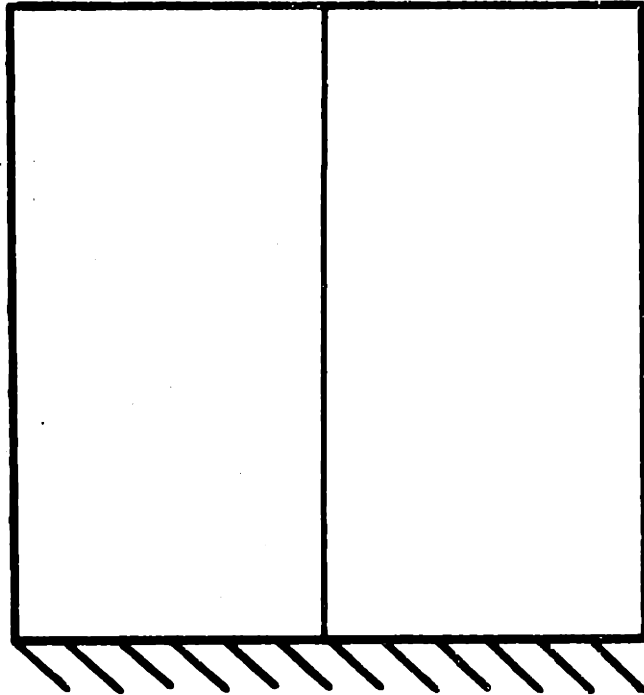
234.2 Hz

FIG. 10 1st BENDING (1st) MODE OF AN
[0₂/+30]_s PLATE



CALCULATED MODE SHAPE

364.4 Hz

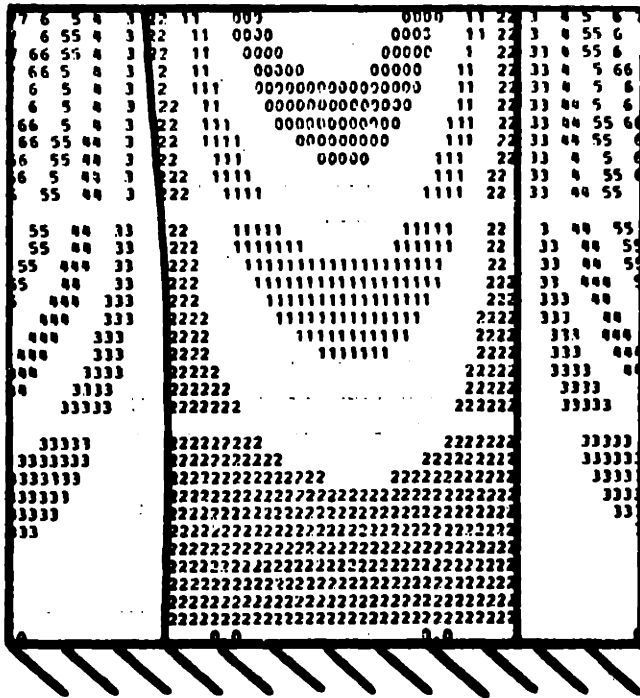


OBSERVED MODE SHAPE

362. Hz

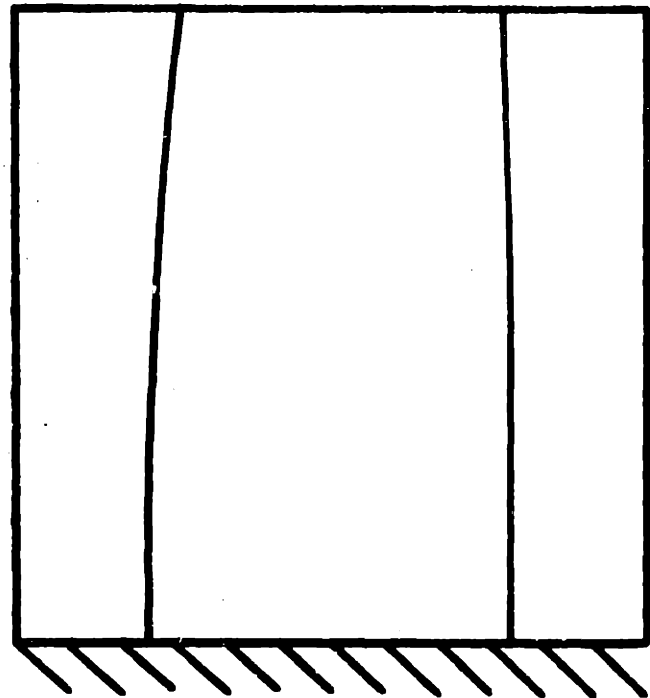
FIG. 11 1st TORSION (2nd) MODE OF AN

[0₂/±30]_s PLATE



CALCULATED MODE SHAPE

762.2 Hz

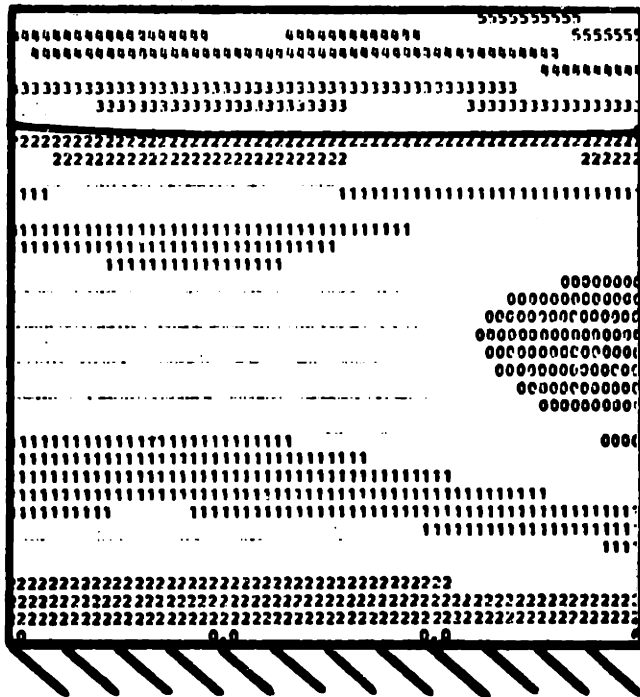


OBSERVED MODE SHAPE

728.3 Hz

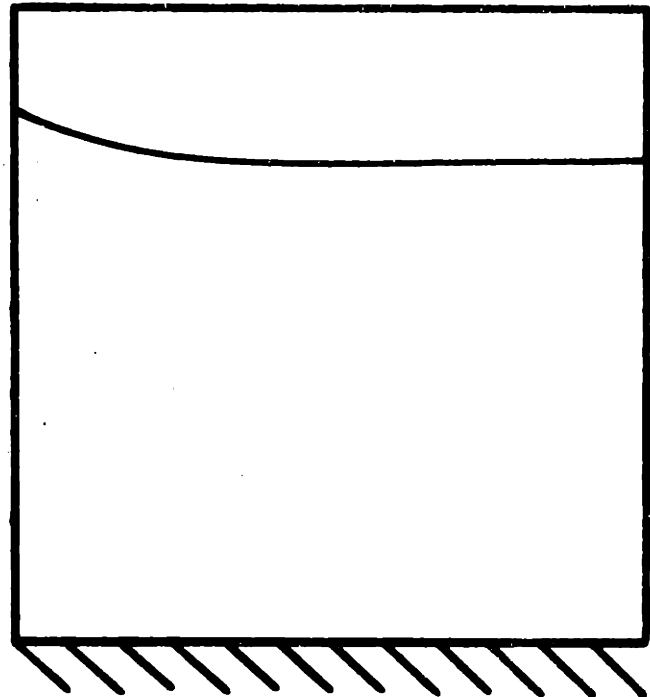
FIG. 12 1st CHORDWISE (3rd) MODE OF A

 $[0_2/\pm 30]_s$ PLATE



CALCULATED MODE SHAPE

1655. Hz

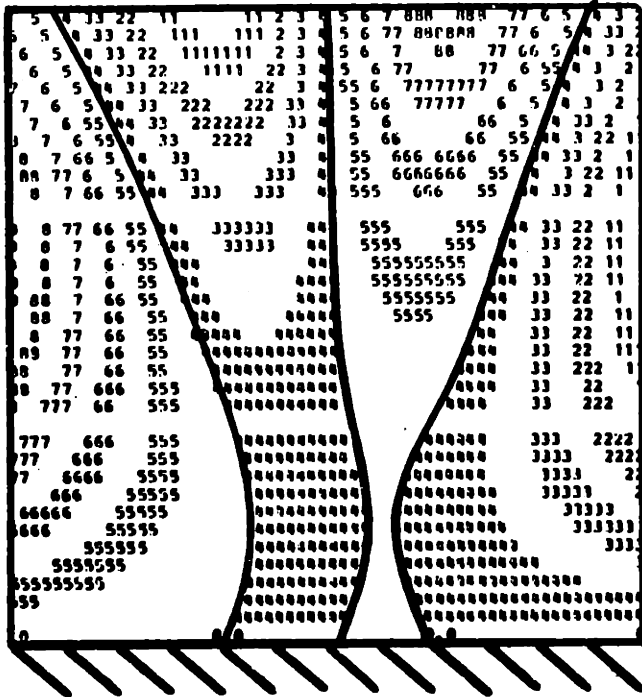


OBSERVED MODE SHAPE

1449 Hz

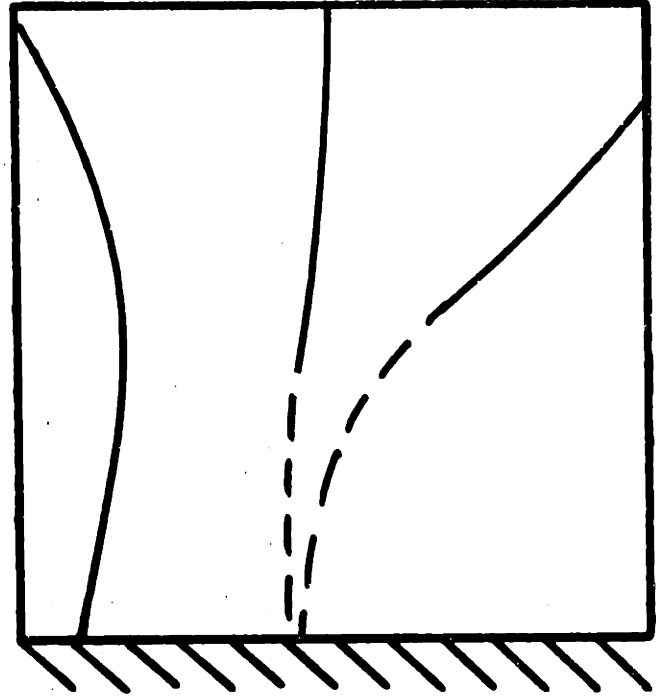
FIG. 13 2nd BENDING (4th) MODE OF A

[0₂/±30]_s PLATE



CALCULATED MODE SHAPE

1709 Hz

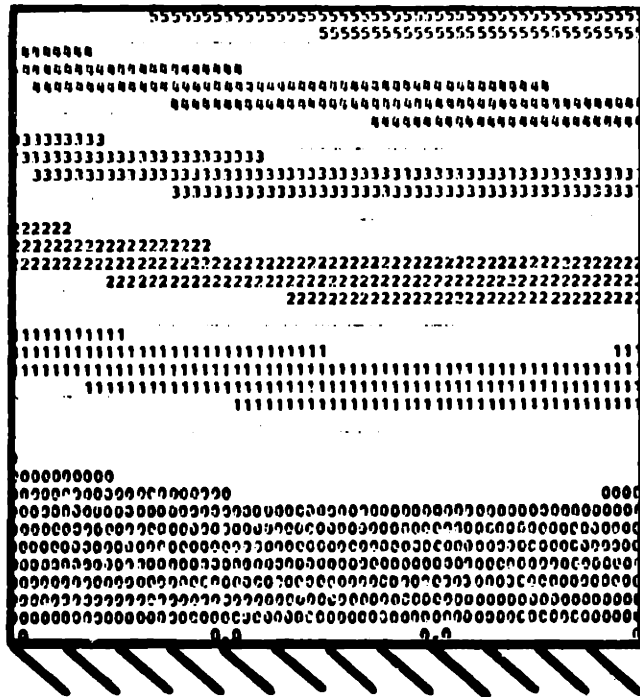


OBSERVED MODE SHAPE

1503 Hz

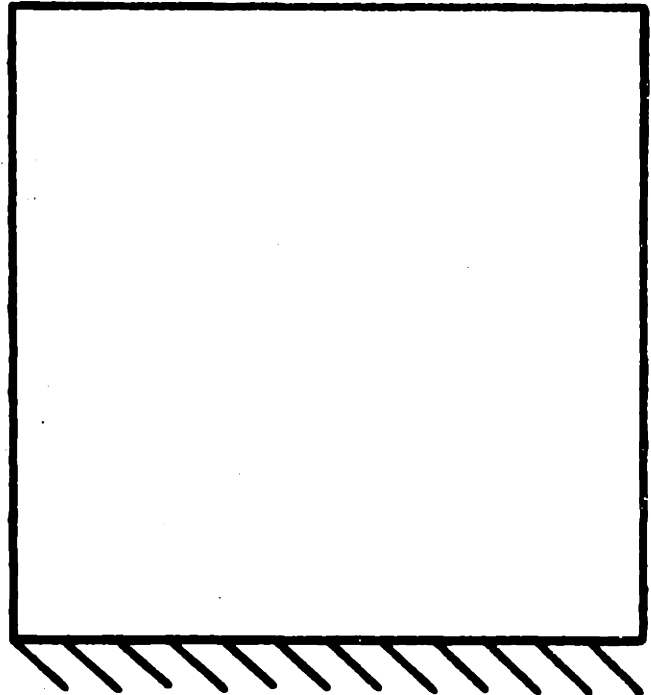
FIG. 14 2nd CHORDWISE (5th) MODE OF A

[0₂/±30]_s PLATE



CALCULATED MODE SHAPE

225.4 Hz

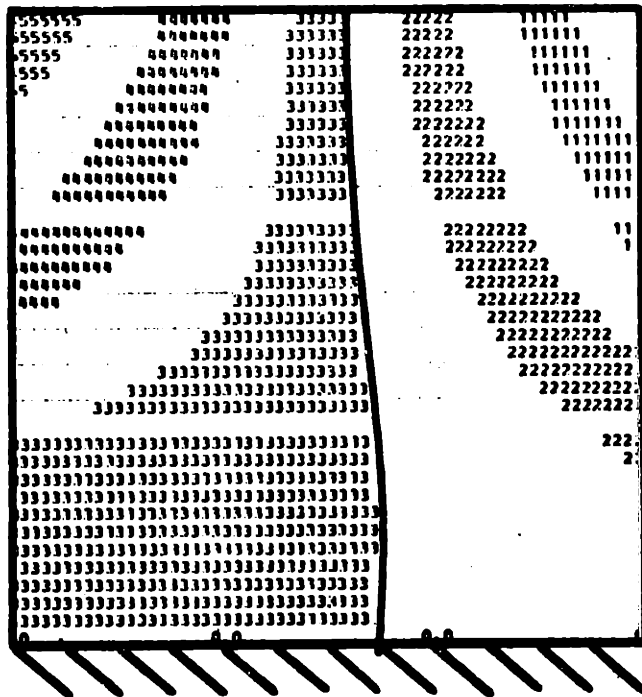


OBSERVED MODE SHAPE

196.4 Hz

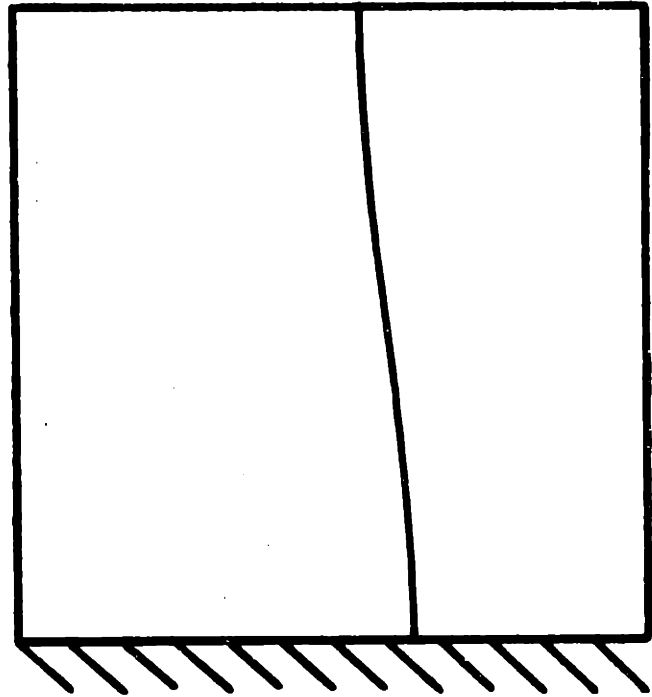
FIG. 15 1st BENDING (1st) MODE OF A

[0/±45/90]_g PLATE



CALCULATED MODE SHAPE

422.2 Hz

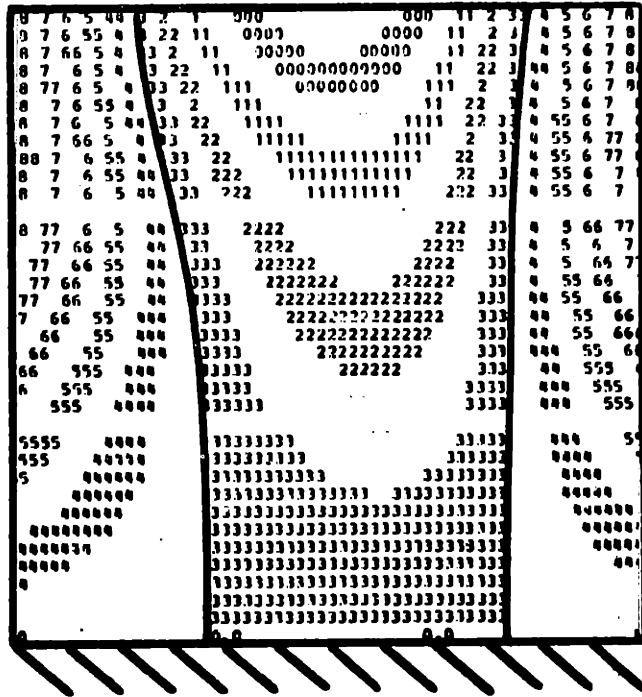


OBSERVED MODE SHAPE

418 Hz

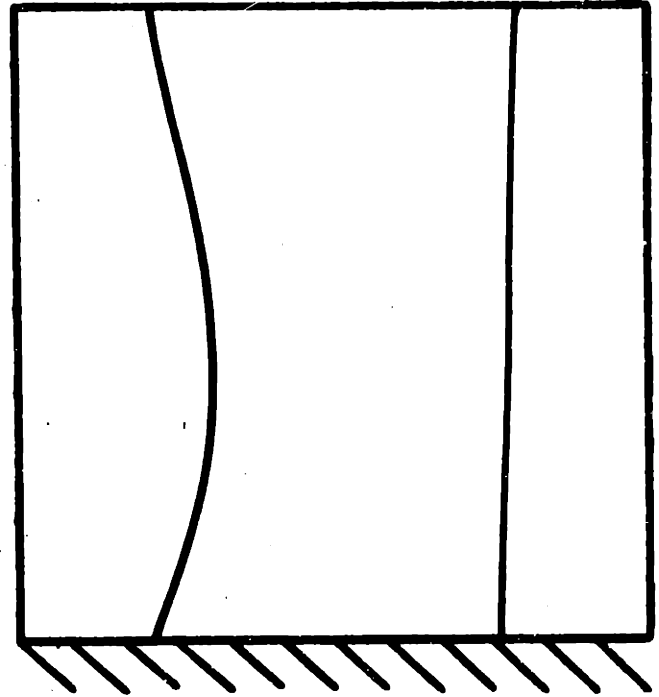
FIG. 16 1st TORSION (2nd) MODE OF A

[0/±45/90]_s PLATE



CALCULATED MODE SHAPE

1013 Hz

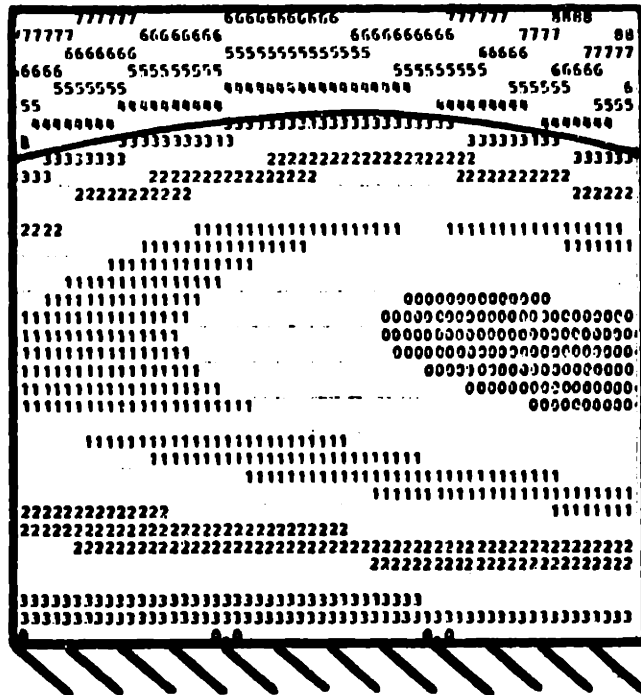


OBSERVED MODE SHAPE

960 Hz

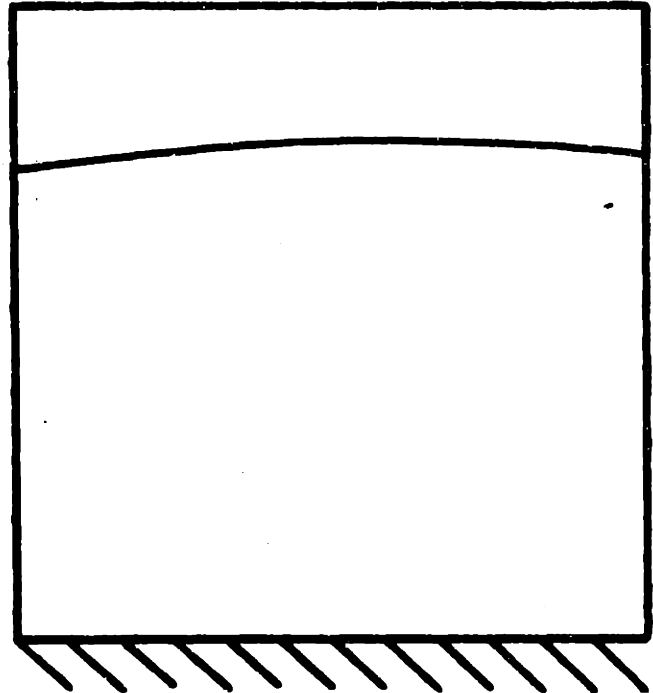
FIG. 17 1st CHORDWISE (3rd) MODE OF A

 $[0/\pm 45/90]_s$ PLATE



CALCULATED MODE SHAPE

1426 Hz

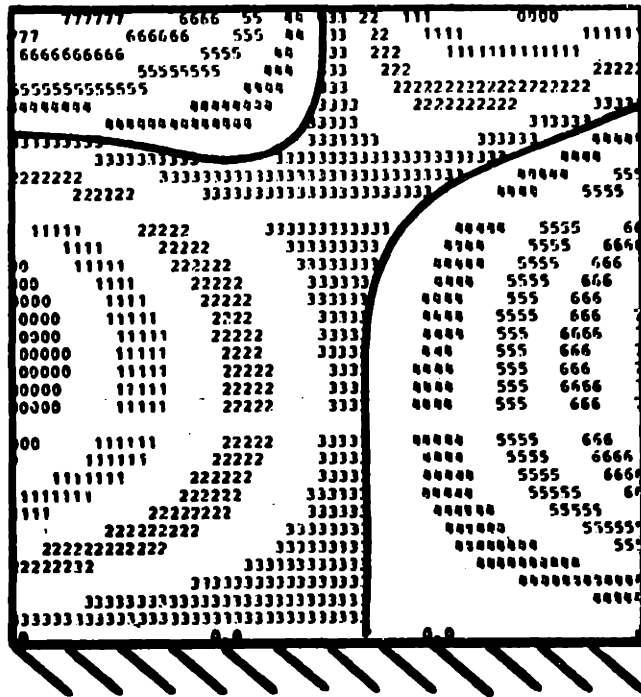


OBSERVED MODE SHAPE

1215 Hz

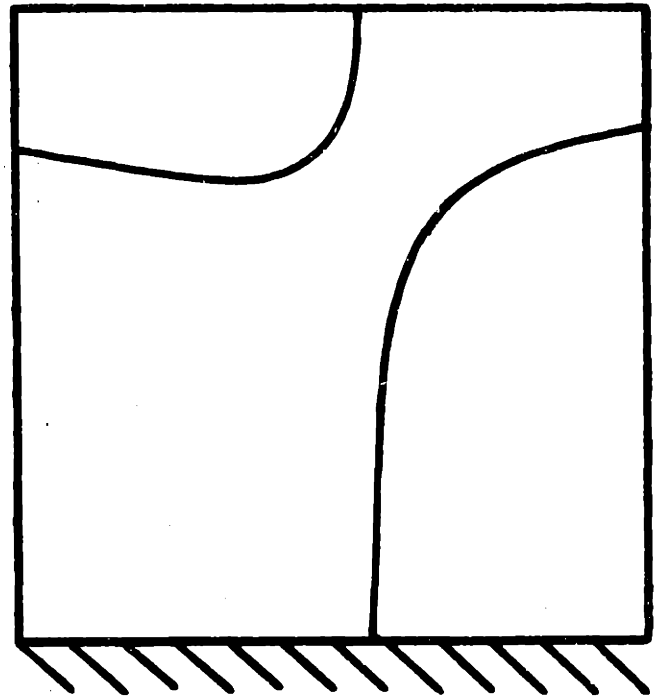
FIG. 18 2nd BENDING (4th) MODE OF A

[0/+45/90]_s PLATE



CALCULATED MODE SHAPE

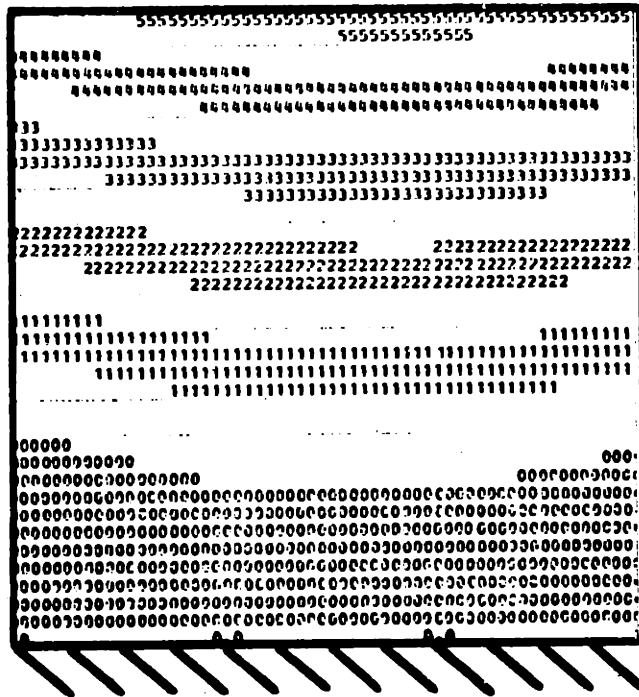
1722 Hz



OBSERVED MODE SHAPE

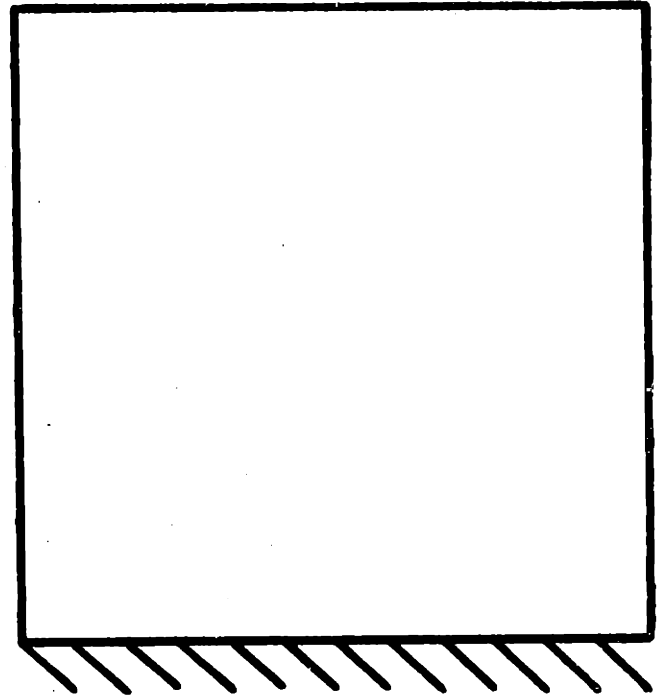
1550 Hz

FIG. 19 2nd TORSION (5th) MODE OF A
 $[0/\pm 45/90]_s$ PLATE



CALCULATED MODE SHAPE

140.8 Hz

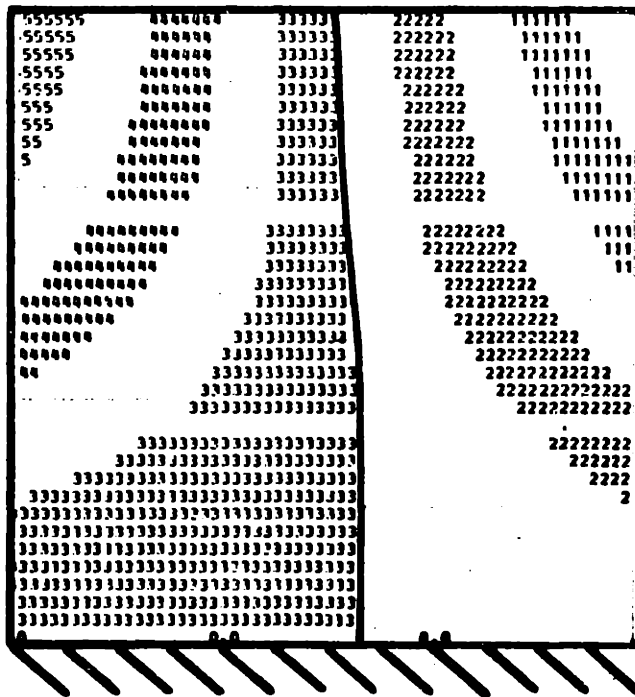


OBSERVED MODE SHAPE

131.2 Hz

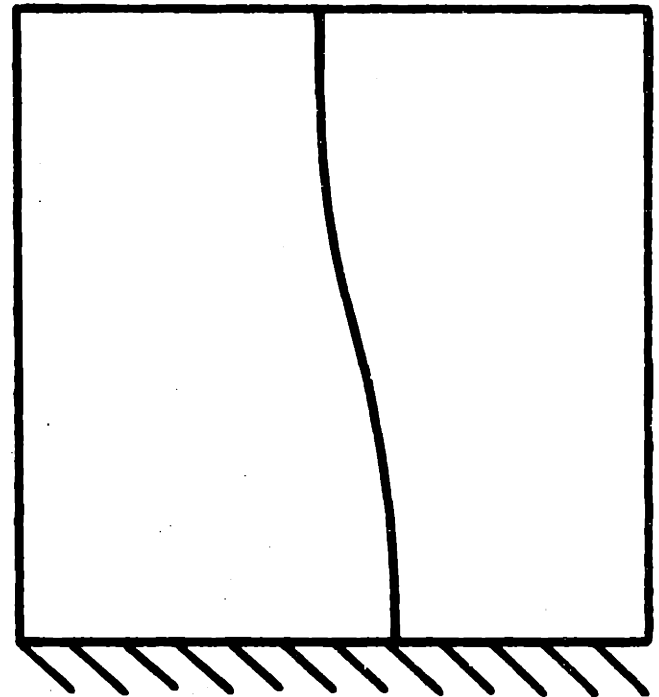
FIG. 20 1st BENDING (1st) MODE OF A

[+45/-45]_s PLATE



CALCULATED MODE SHAPE

500.0 Hz

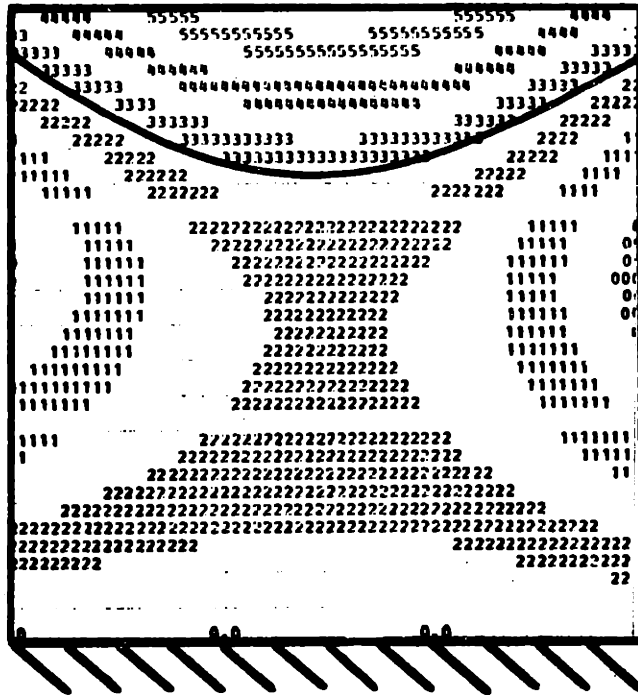


OBSERVED MODE SHAPE

472. Hz

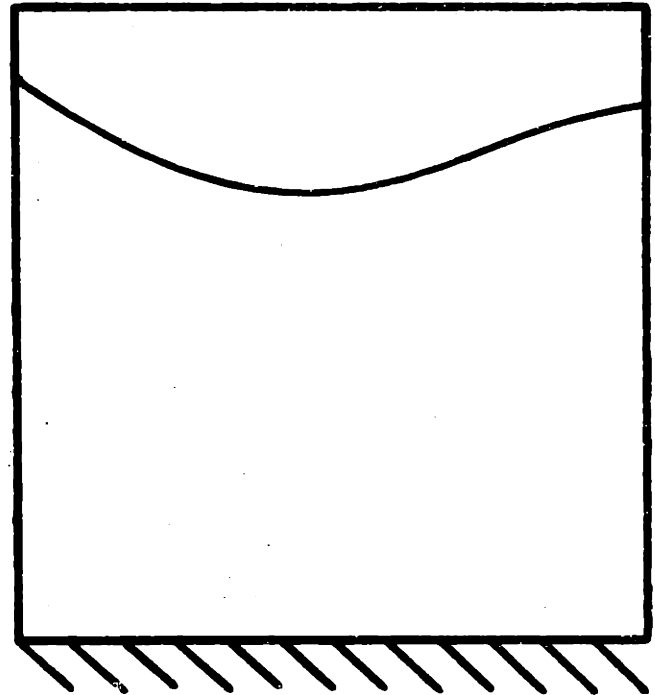
FIG. 21 1st TORSION (2nd) MODE OF A

[$\pm 45/\mp 45$]_s PLATE



CALCULATED MODE SHAPE

805.3 Hz

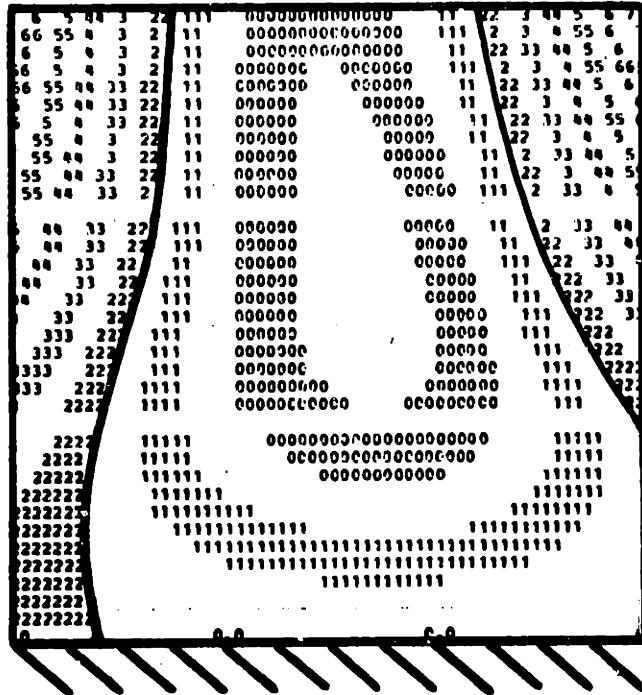


OBSERVED MODE SHAPE

790.5 Hz

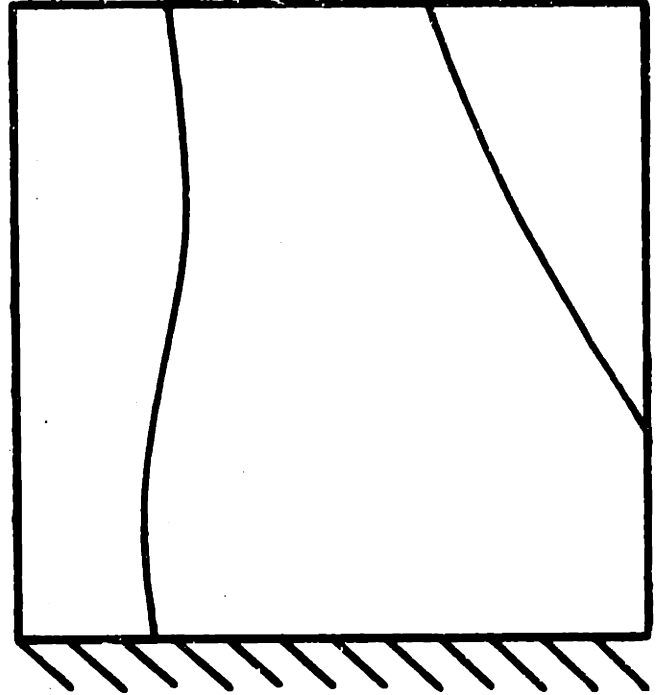
FIG. 22 2nd BENDING (3rd) MODE OF A

[+45/-45]_s PLATE



CALCULATED MODE SHAPE

1326 Hz

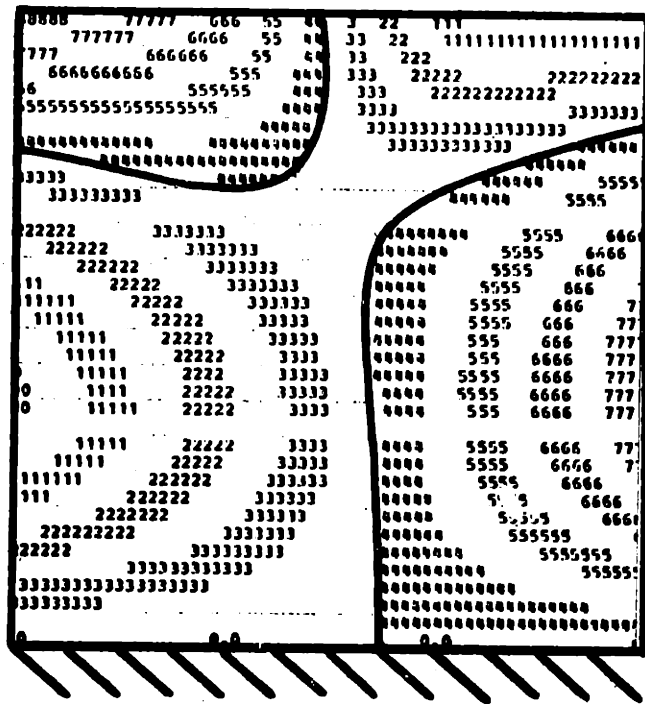


OBSERVED MODE SHAPE

11.68 Hz

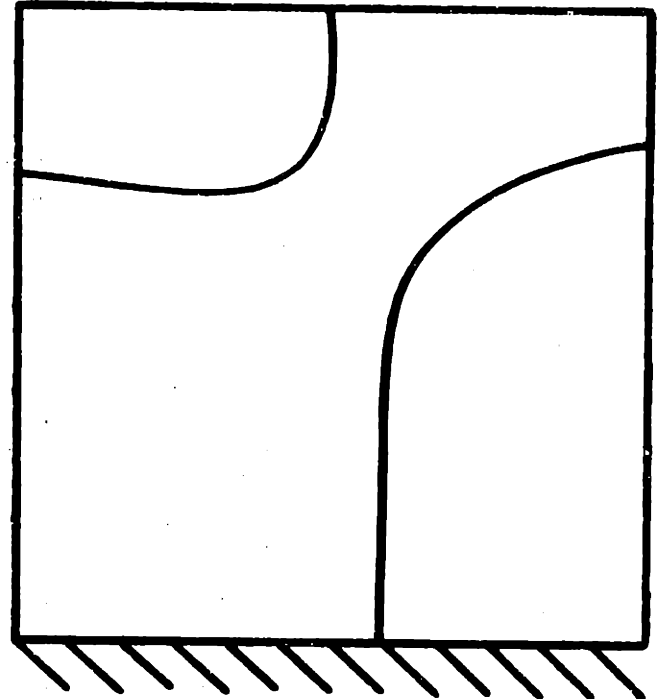
FIG. 23 1st CHORDWISE (4th) MODE OF A

[+45/-45]_s PLATE



CALCULATED MODE SHAPE

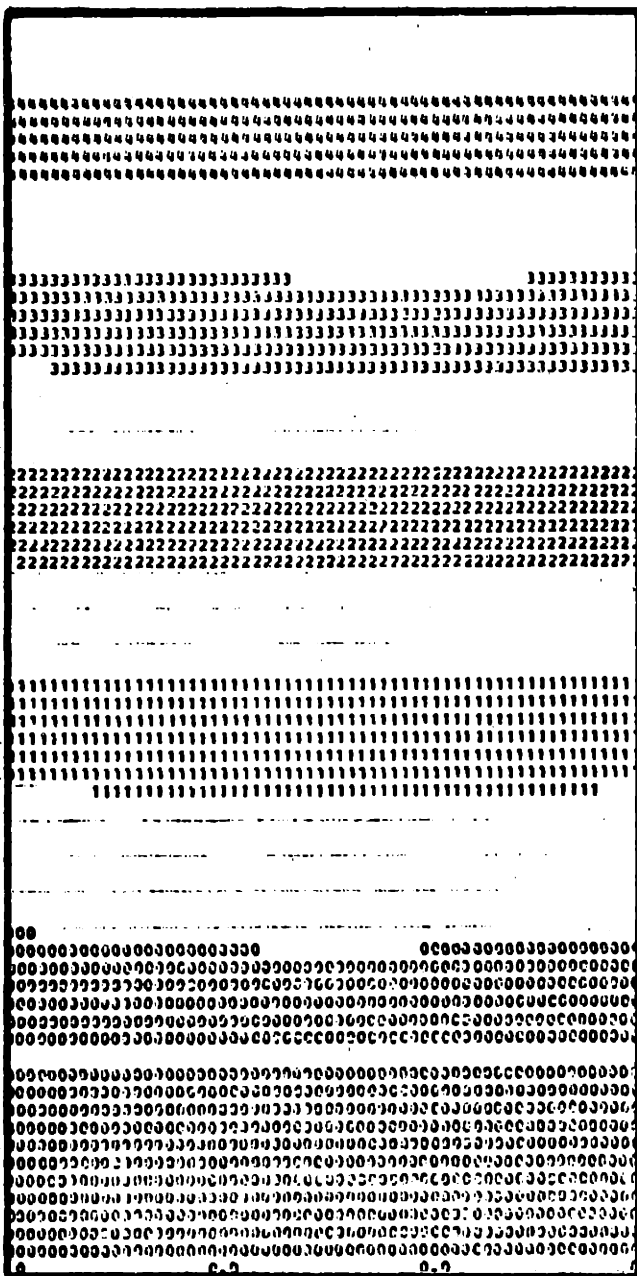
1645 Hz



OBSERVED MODE SHAPE

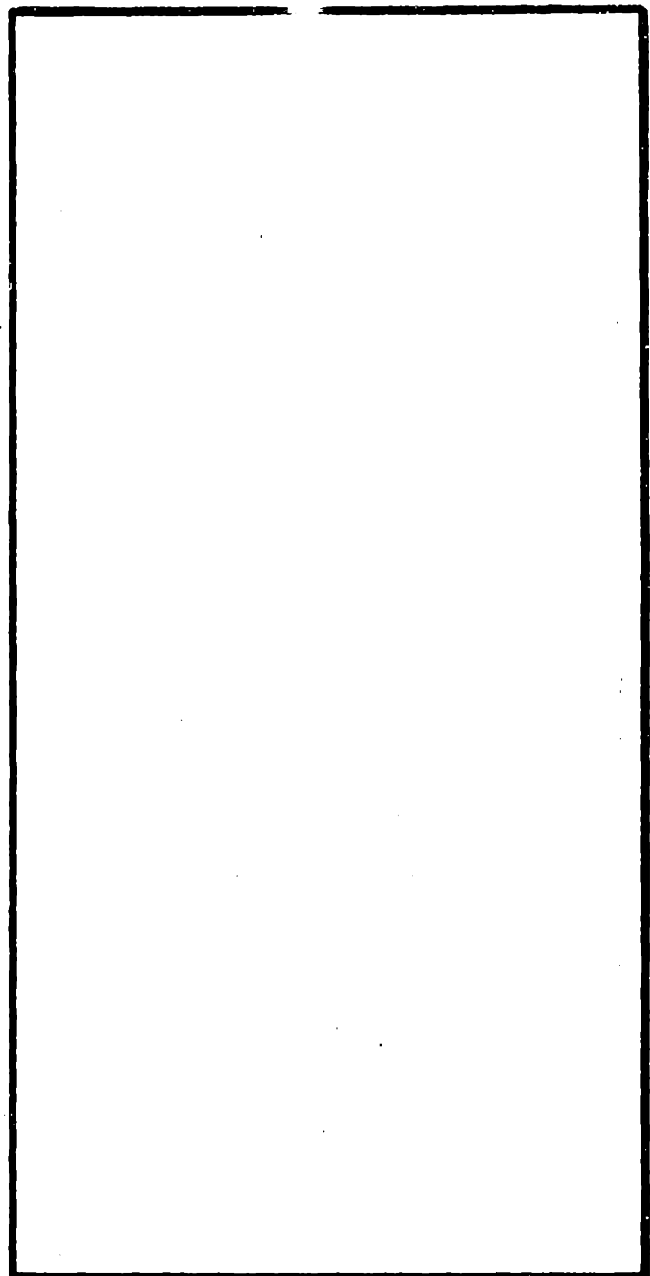
1486 Hz

FIG. 24 2nd TORSION (5th) MODE OF A
 $[+45/\bar{+45}]_s$ PLATE



CALCULATED MODE SHAPE

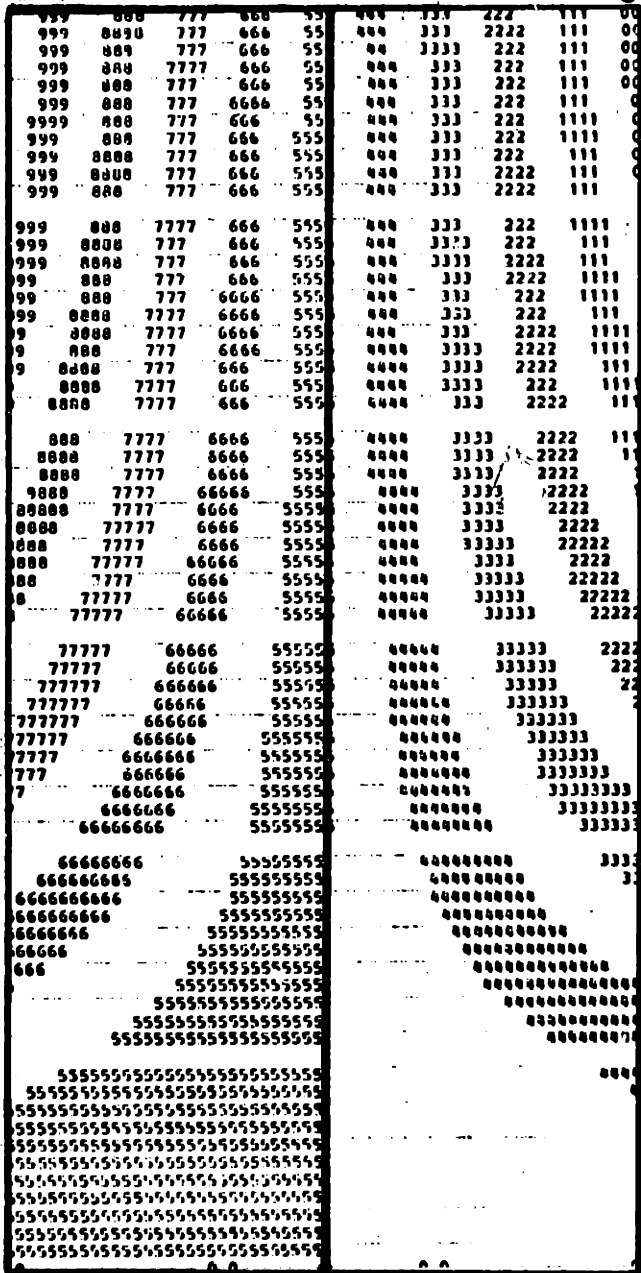
37.66 Hz



OBSERVED MODE SHAPE

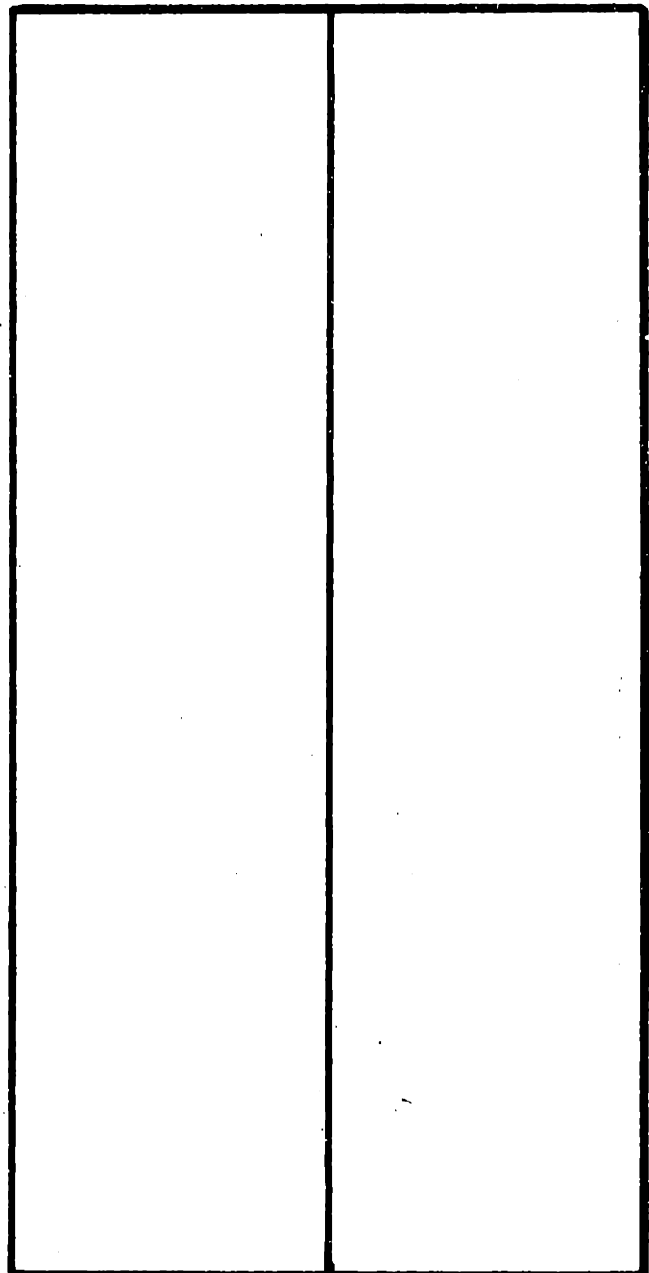
37.6 Hz

FIG. 25 1st BENDING (1st) MODE OF A
ALUMINUM PLATE



CALCULATED MODE SHAPE

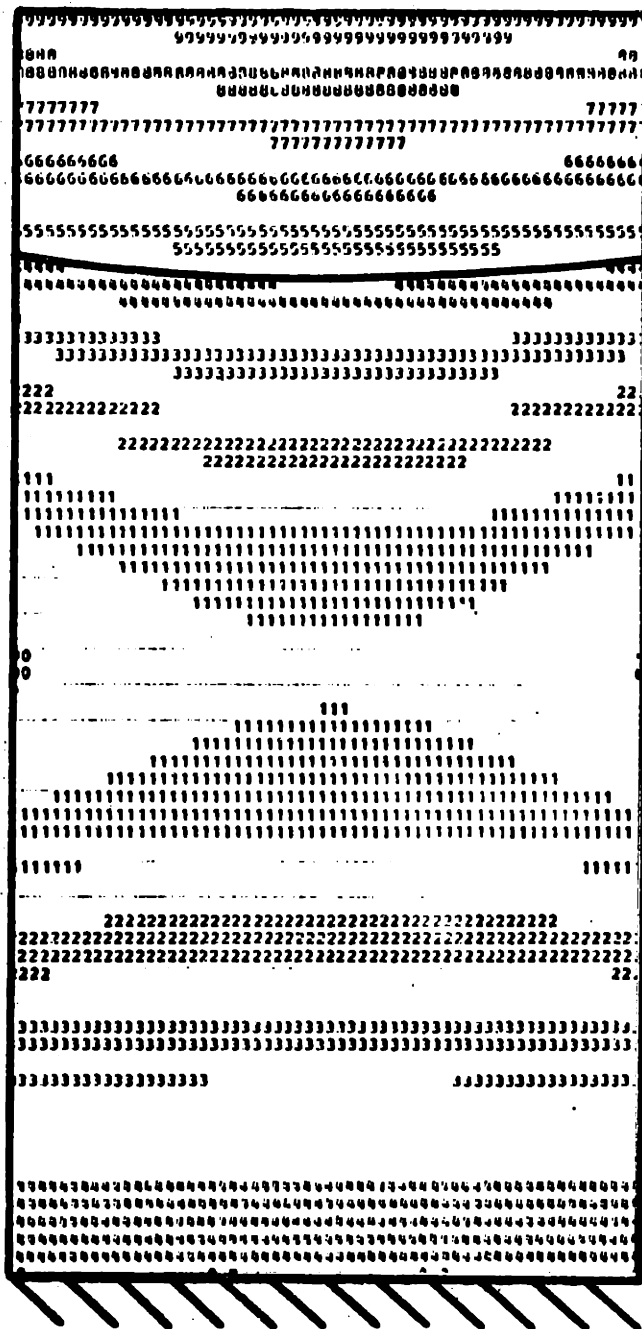
161.5 Hz



OBSERVED MODE SHAPE

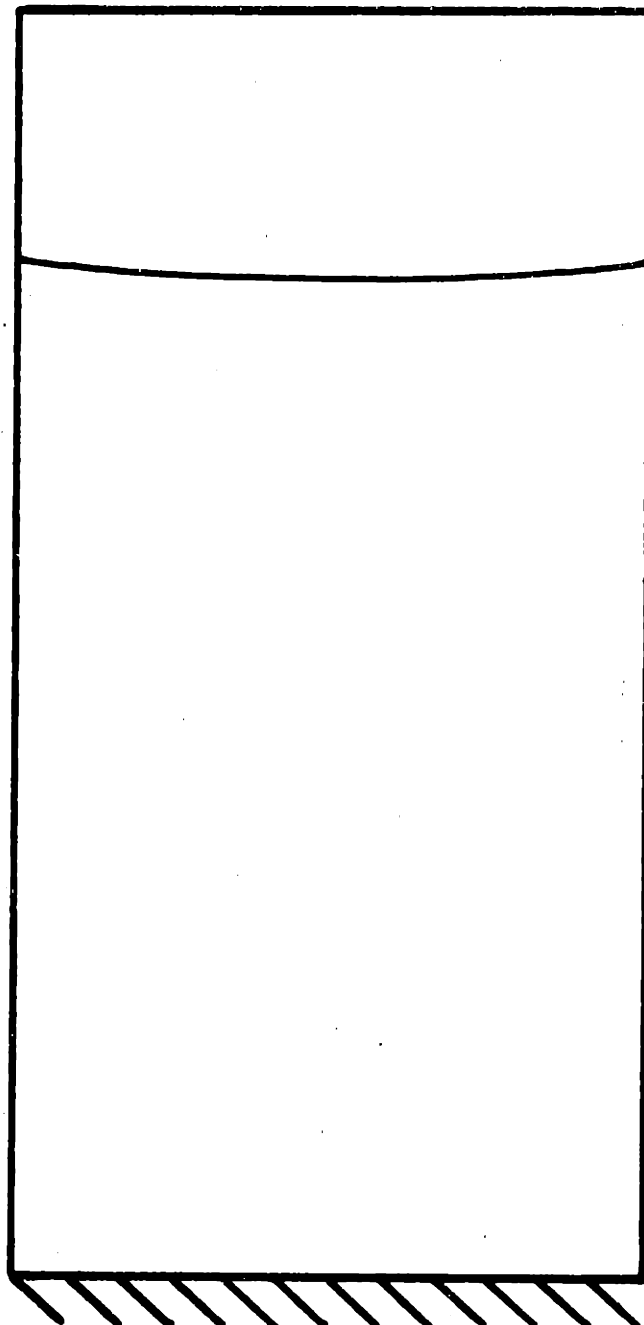
158 Hz

FIG. 26 1st TORSION (2nd) MODE OF AN
ALUMINUM PLATE



CALCULATED MODE SHAPE

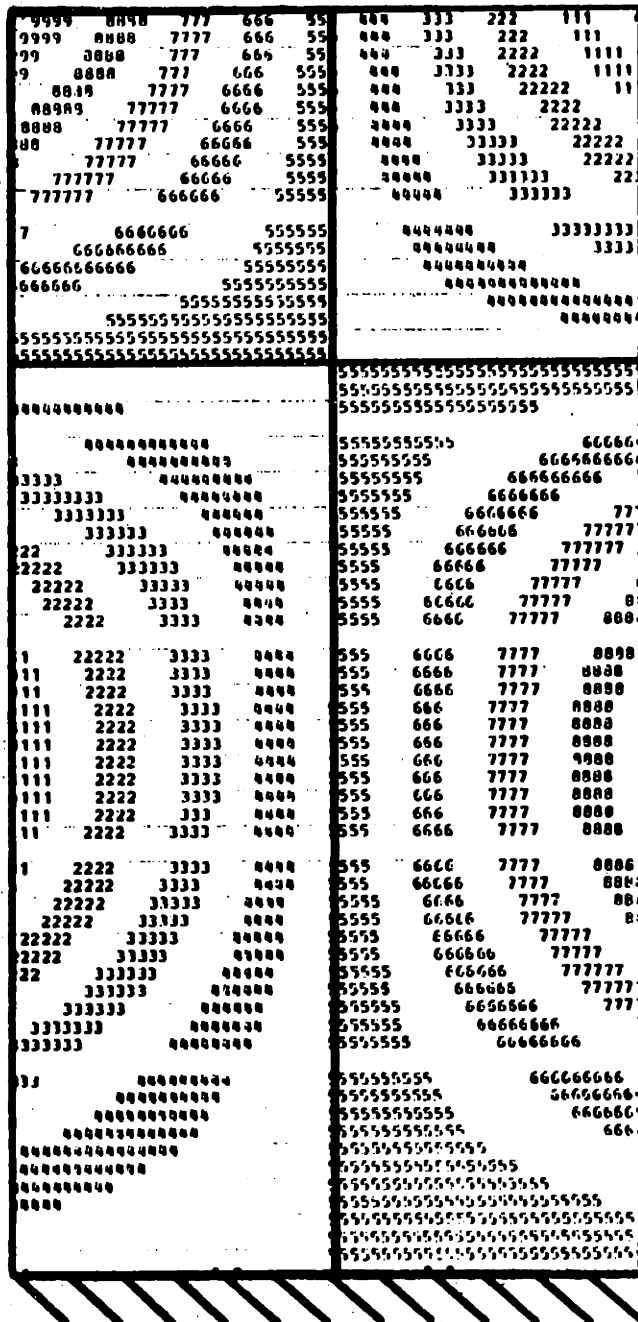
234.3 Hz



OBSERVED MODE SHAPE

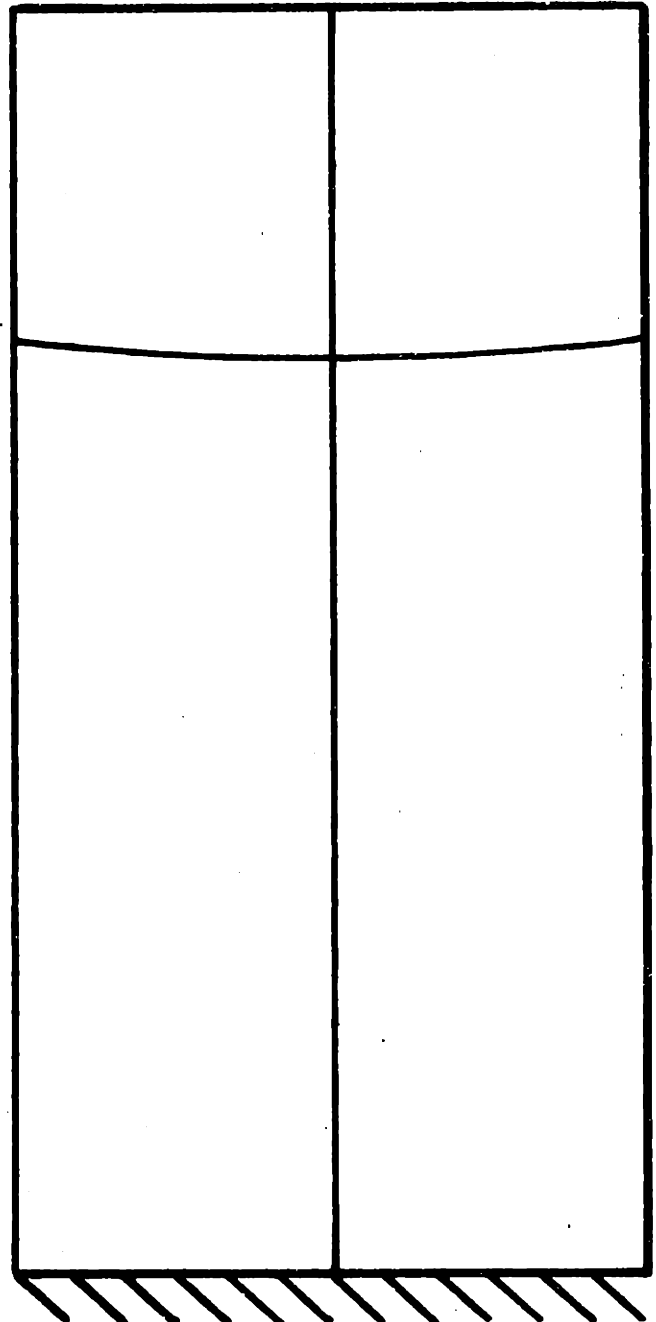
234.9 Hz

FIG. 27 2nd BENDING (3rd) MODE OF AN
ALUMINUM PLATE



CALCULATED MODE SHAPE

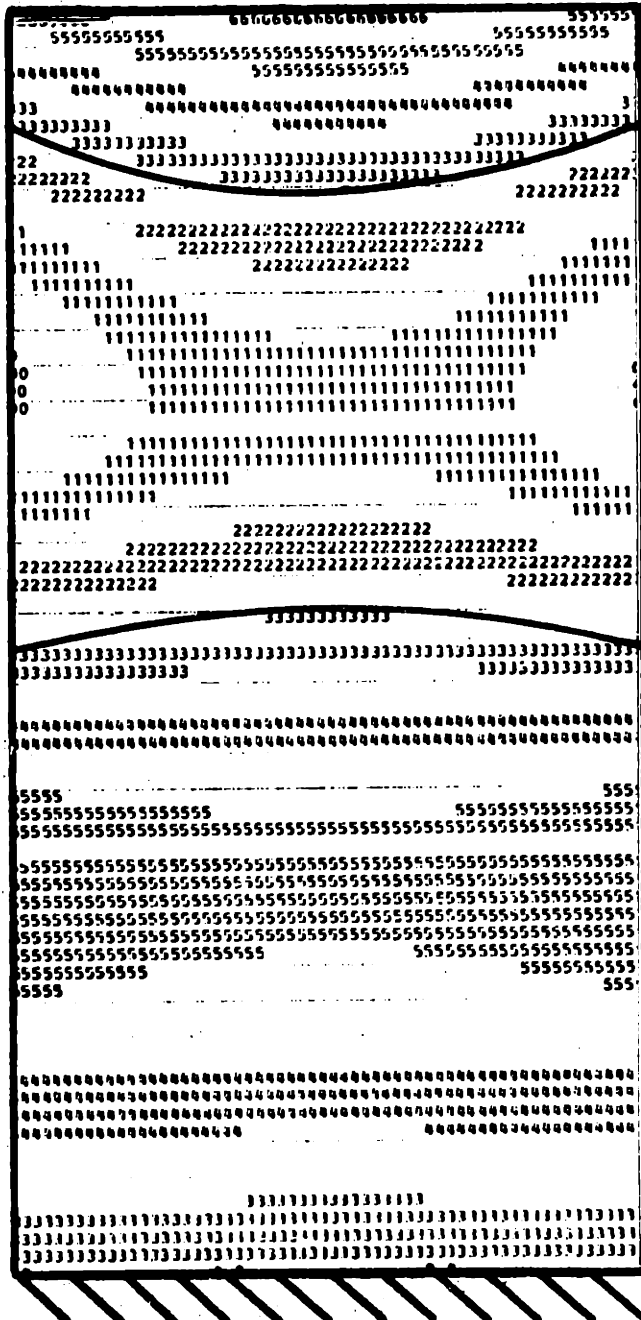
523.6 Hz



OBSERVED MODE SHAPE

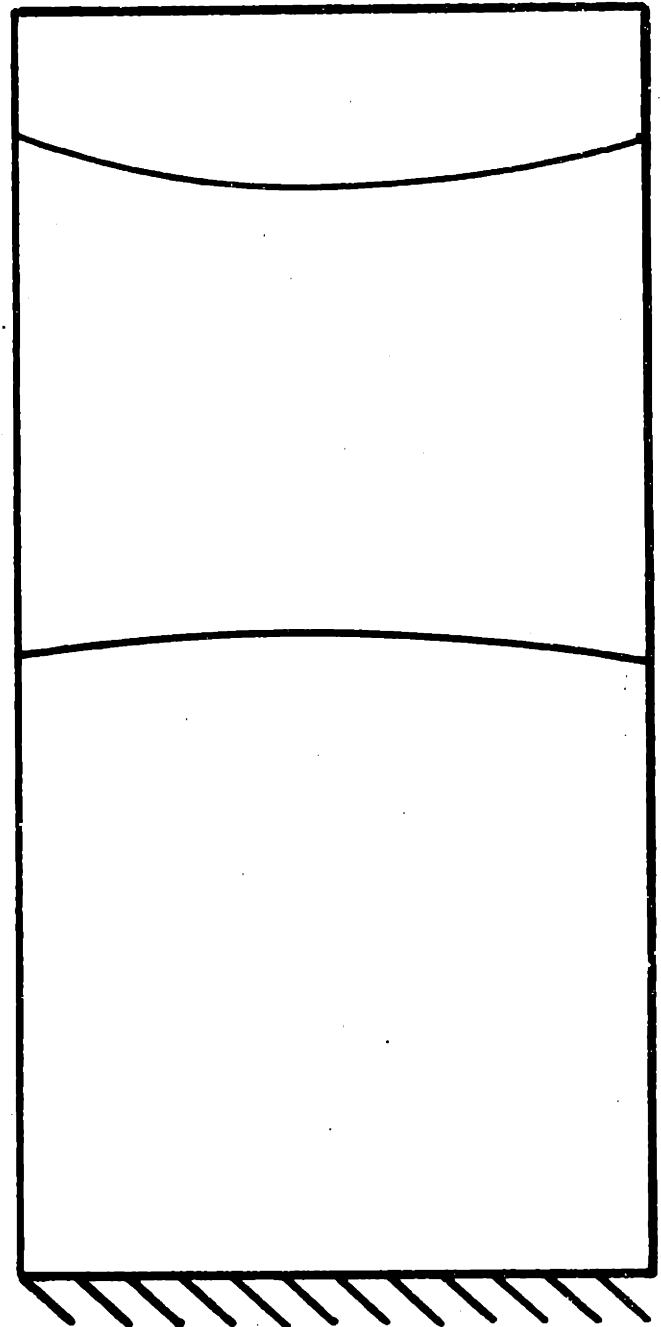
518.8 Hz

FIG. 28 2nd TORSION (4th) MODE OF AN
ALUMINUM PLATE



CALCULATED MODE SHAPE

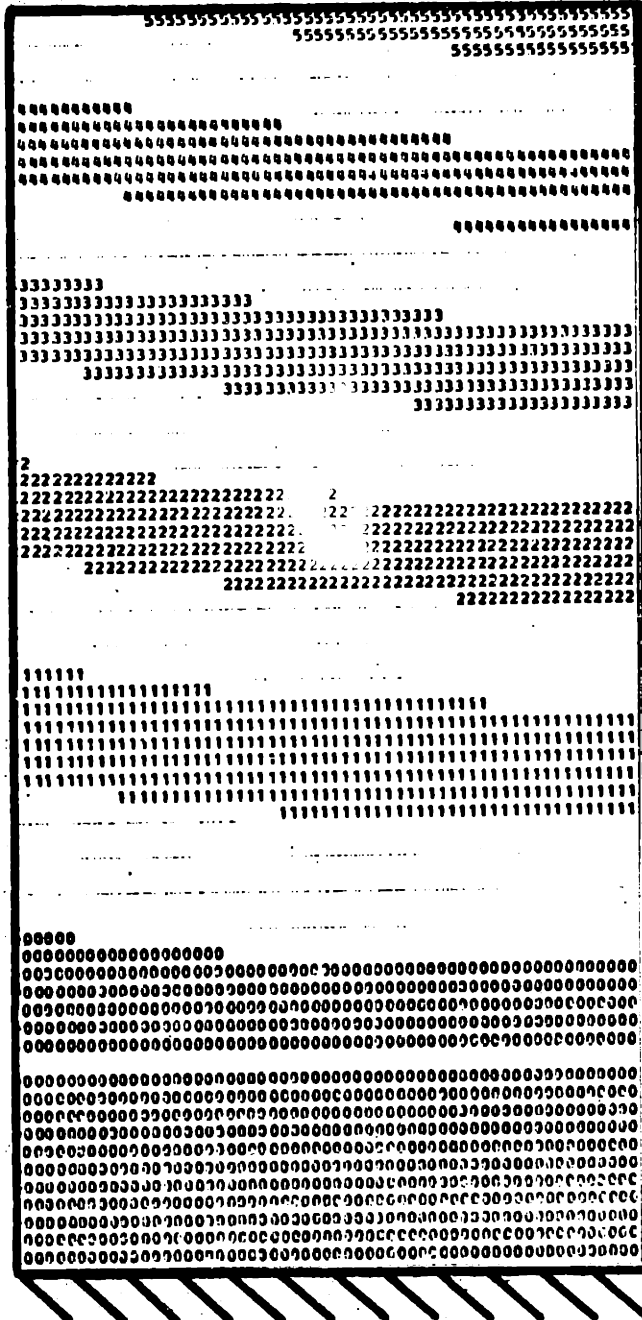
660.2 Hz



OBSERVED MODE SHAPE

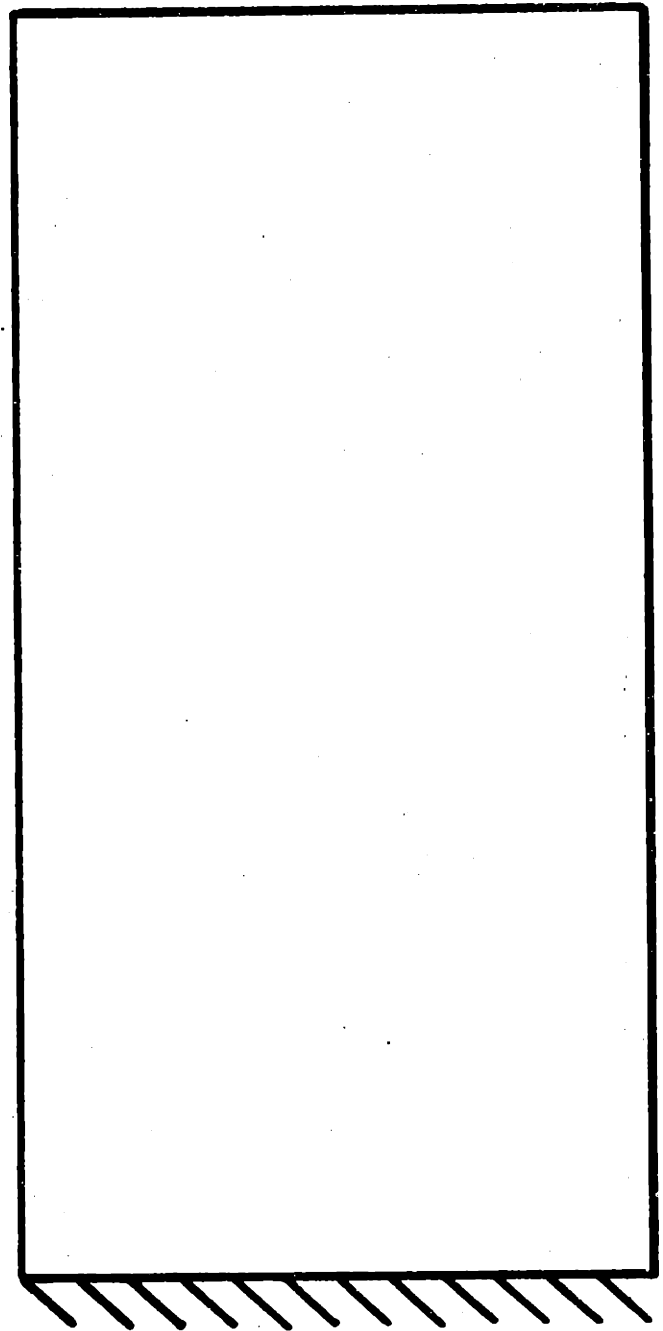
658.1 Hz

FIG. 29 3rd BENDING (5th) MODE OF AN
ALUMINUM PLATE



CALCULATED MODE SHAPE

(68.98) Hz

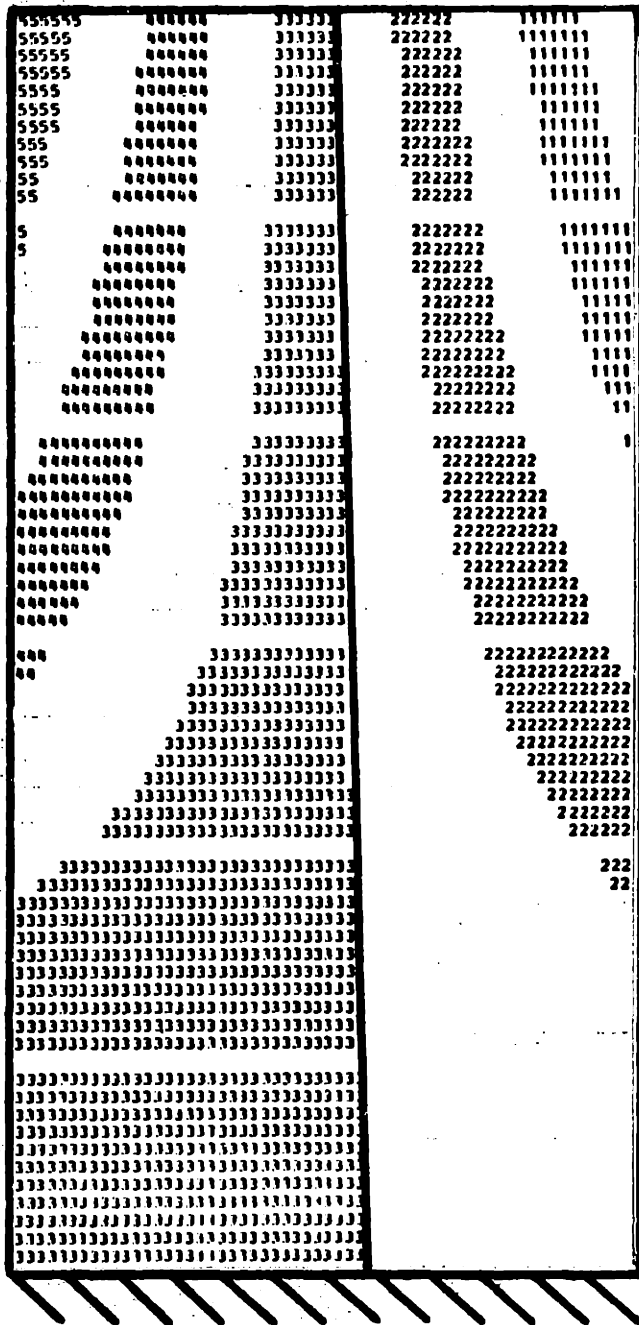


OBSERVED MODE SHAPE

58.3 Hz

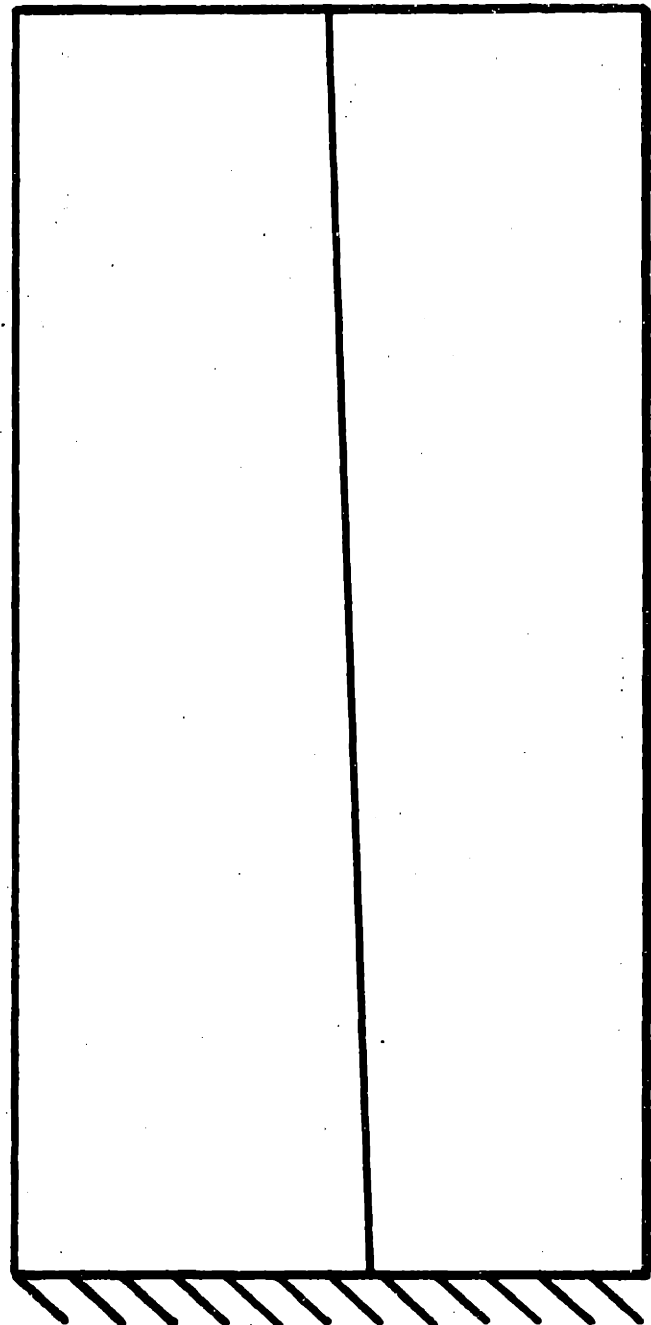
FIG. 30 1st BENDING (1st) MODE OF A

[0₂/+30]_s PLATE



CALCULATED MODE SHAPE

139.1 Hz

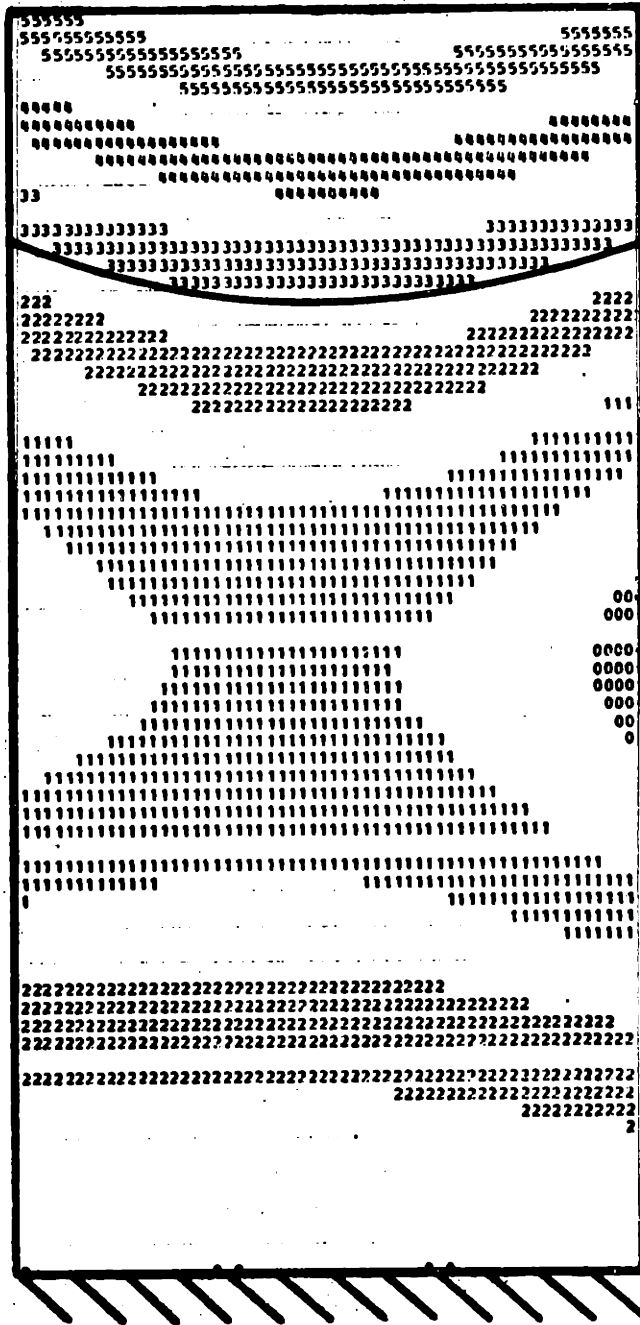


OBSERVED MODE SHAPE

148. Hz

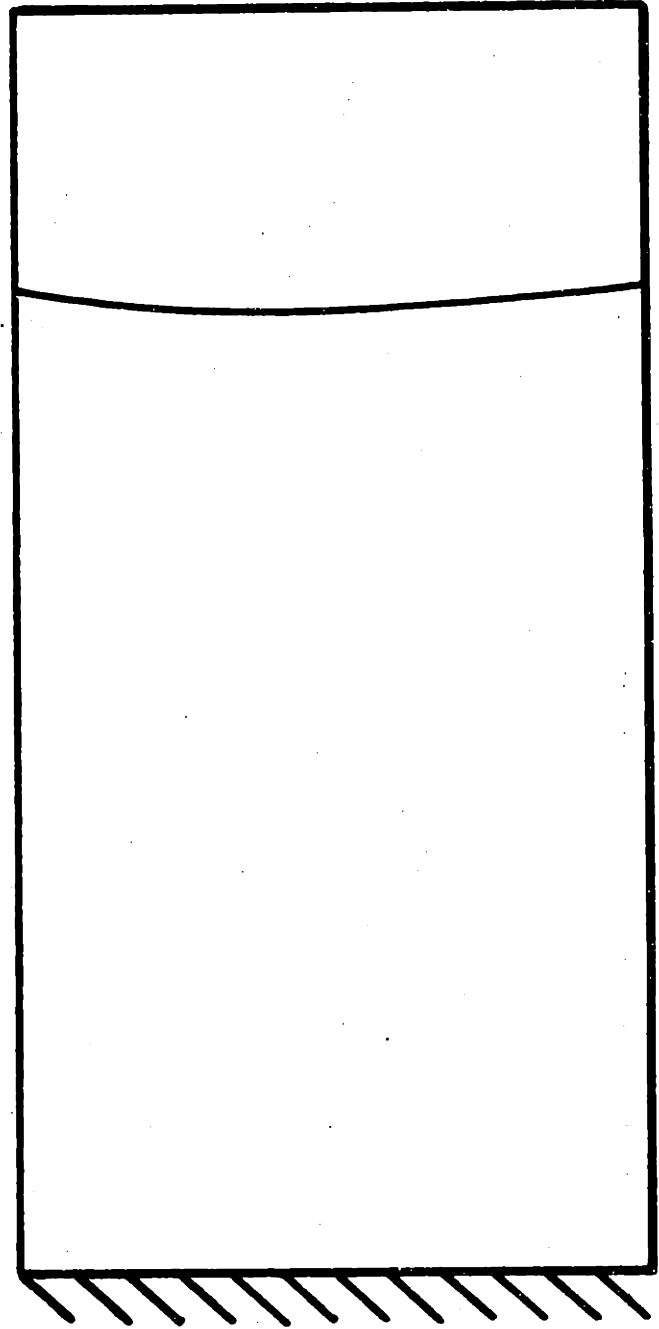
FIG. 31 1st TORSION (2nd) MODE OF A

[0₂/+30]_s PLATE



CALCULATED MODE SHAPE

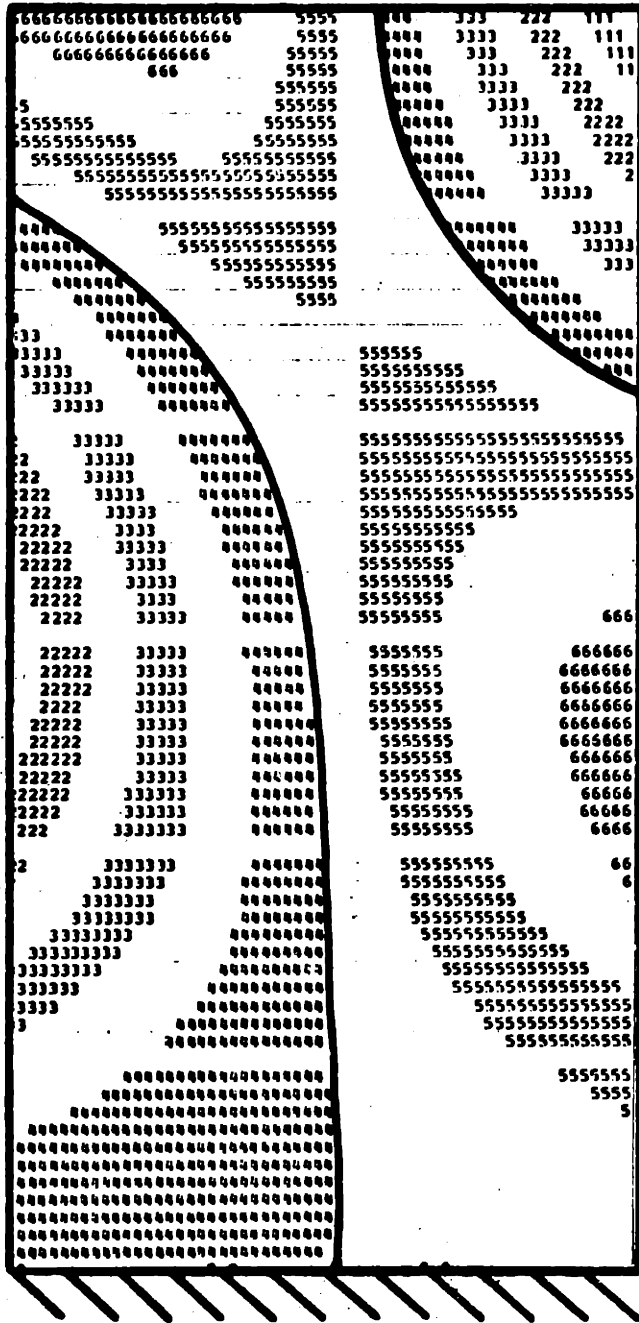
408.7 Hz



OBSERVED MODE SHAPE

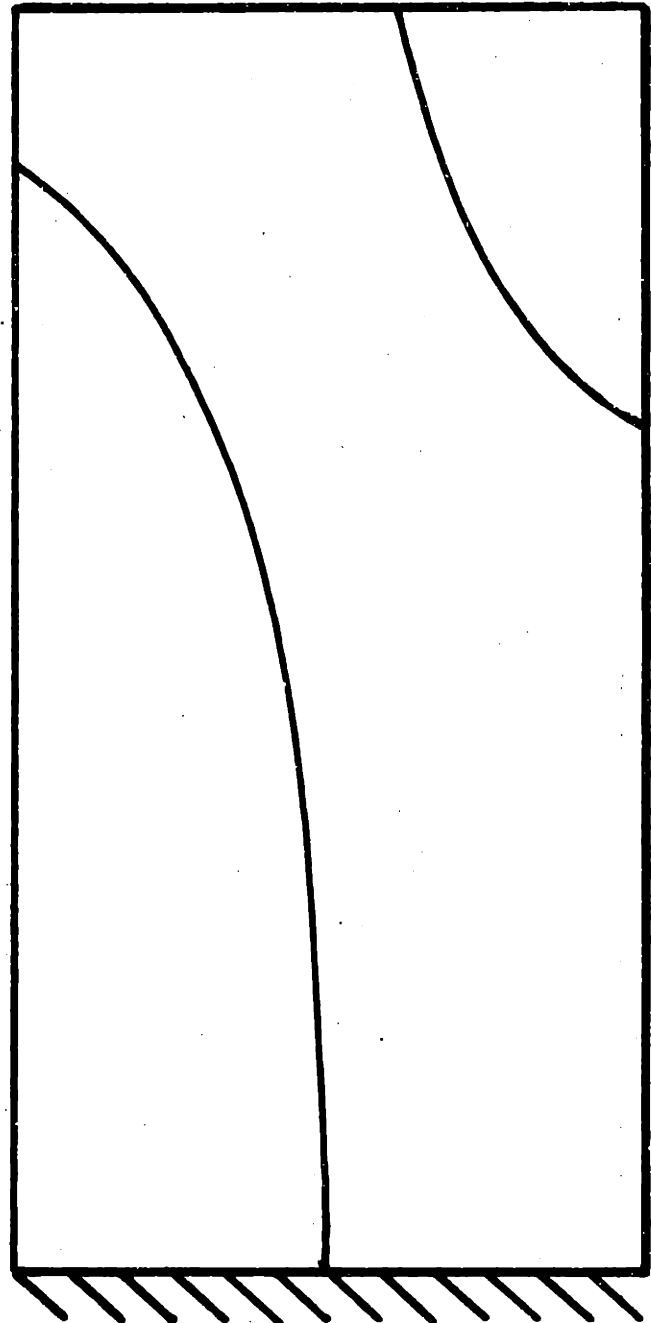
362.7 Hz

FIG. 32 2nd BENDING (3rd) MODE OF A
 $[0_2/+30]_s$ PLATE



CALCULATED MODE SHAPE

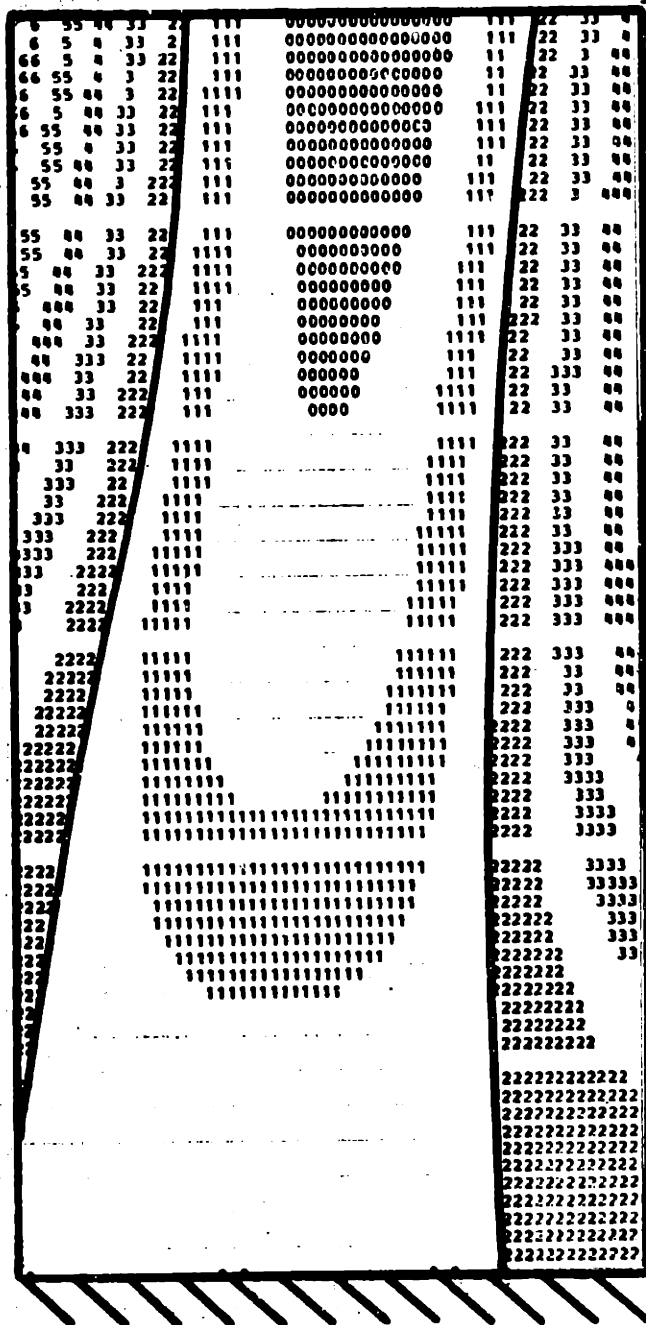
526.0 Hz



OBSERVED MODE SHAPE

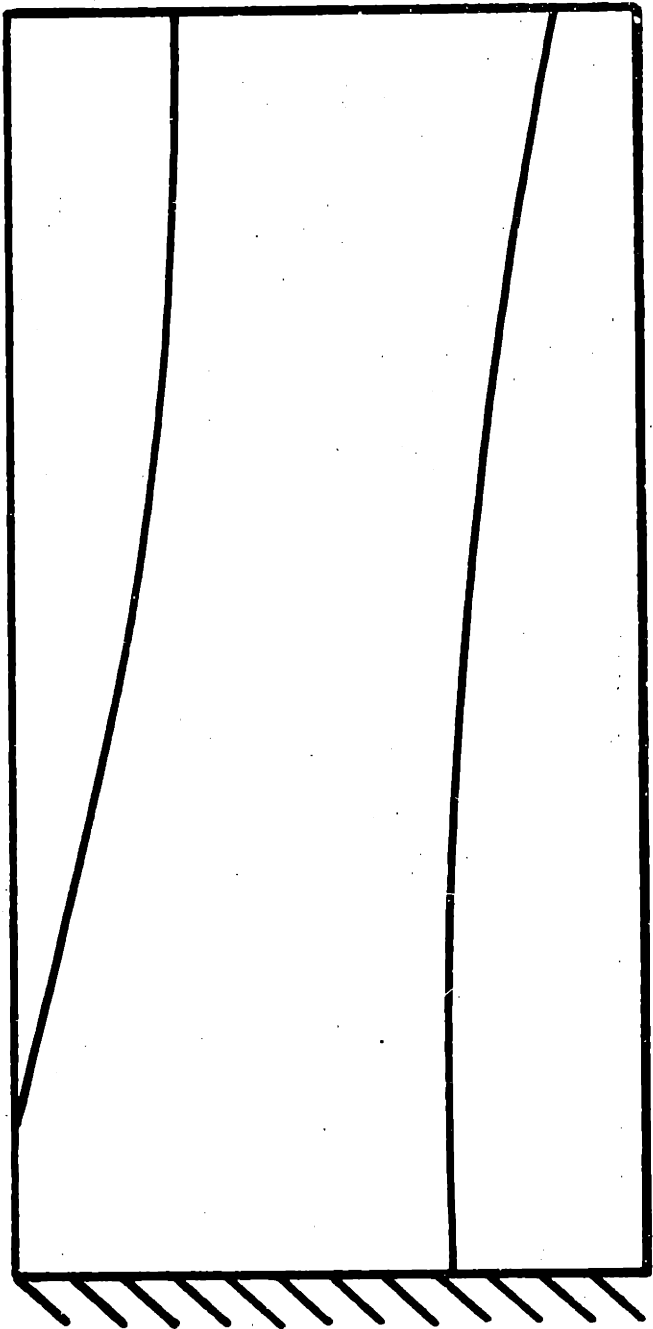
508. Hz

FIG. 33 2nd TORSION (4th) MODE OF A
 $[0_2/\pm 30]_S$ PLATE



CALCULATED MODE SHAPE

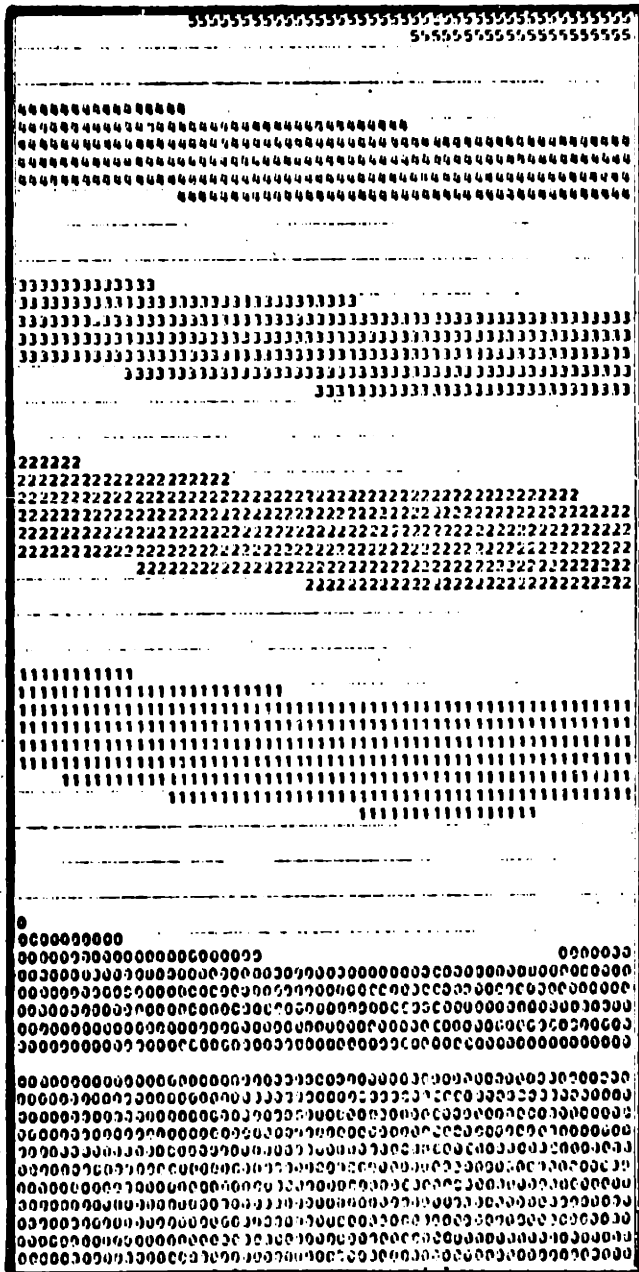
588.8 Hz



OBSERVED MODE SHAPE

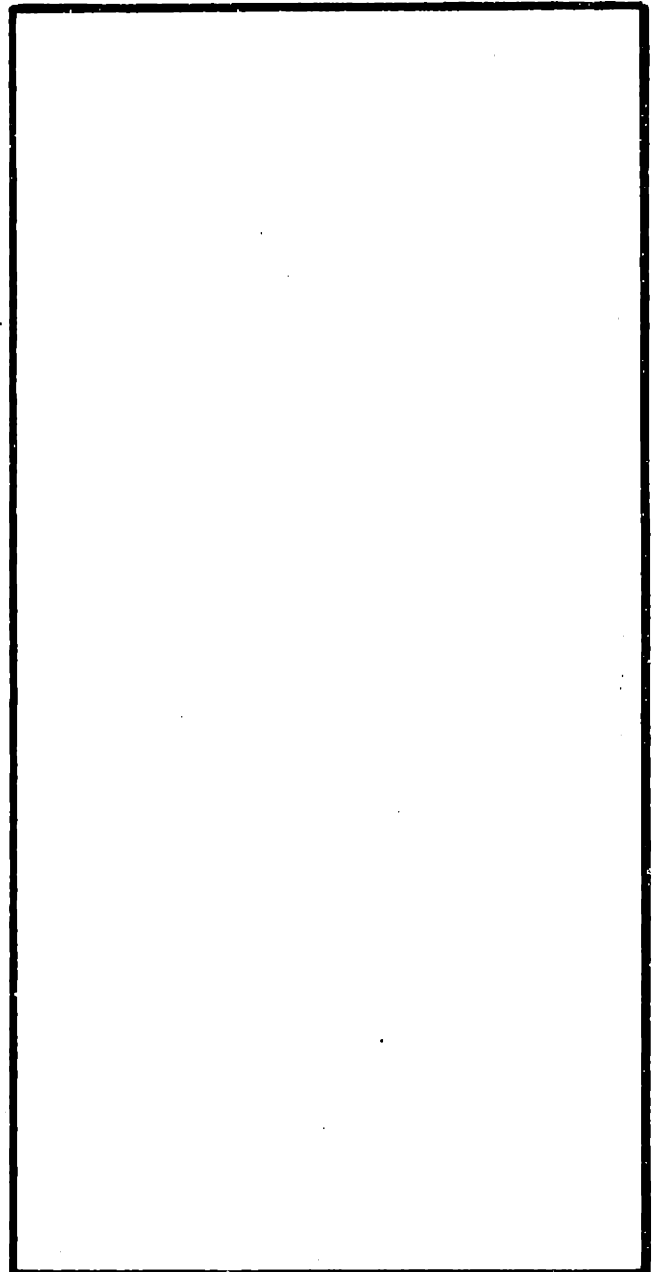
546 Hz

FIG. 34 1st CHORDWISE (5th) MODE OF A
 $[0_2/+30]_s$ PLATE



CALCULATED MODE SHAPE

(59.63) Hz

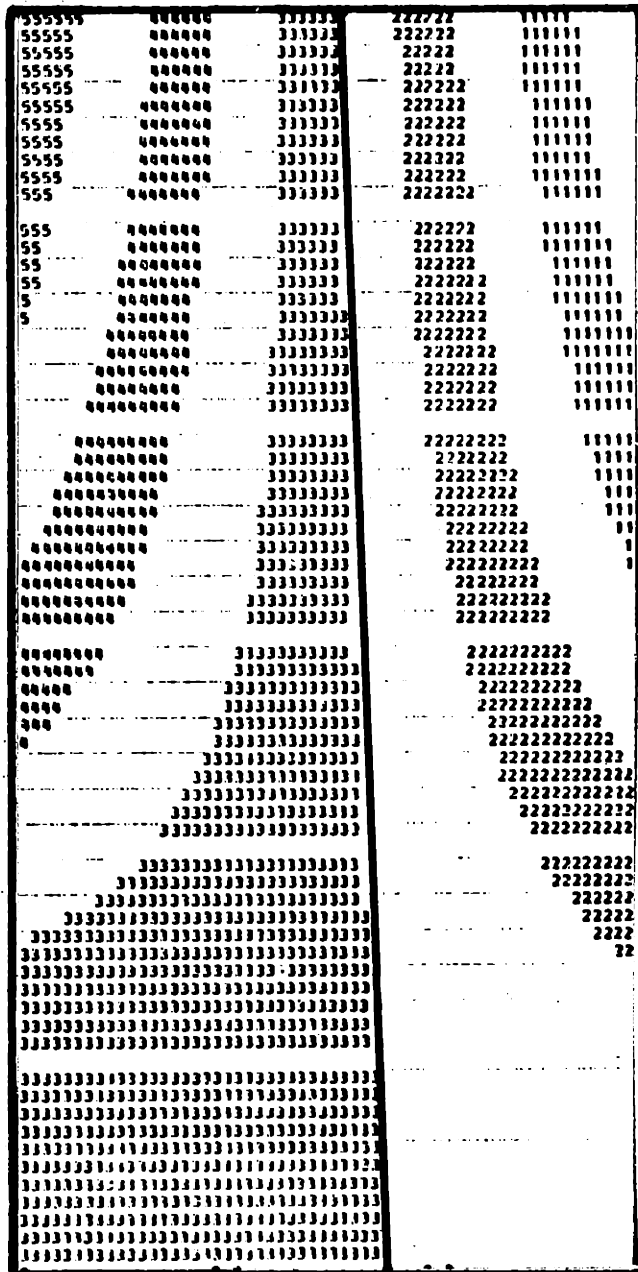


OBSERVED MODE SHAPE

48.6 Hz

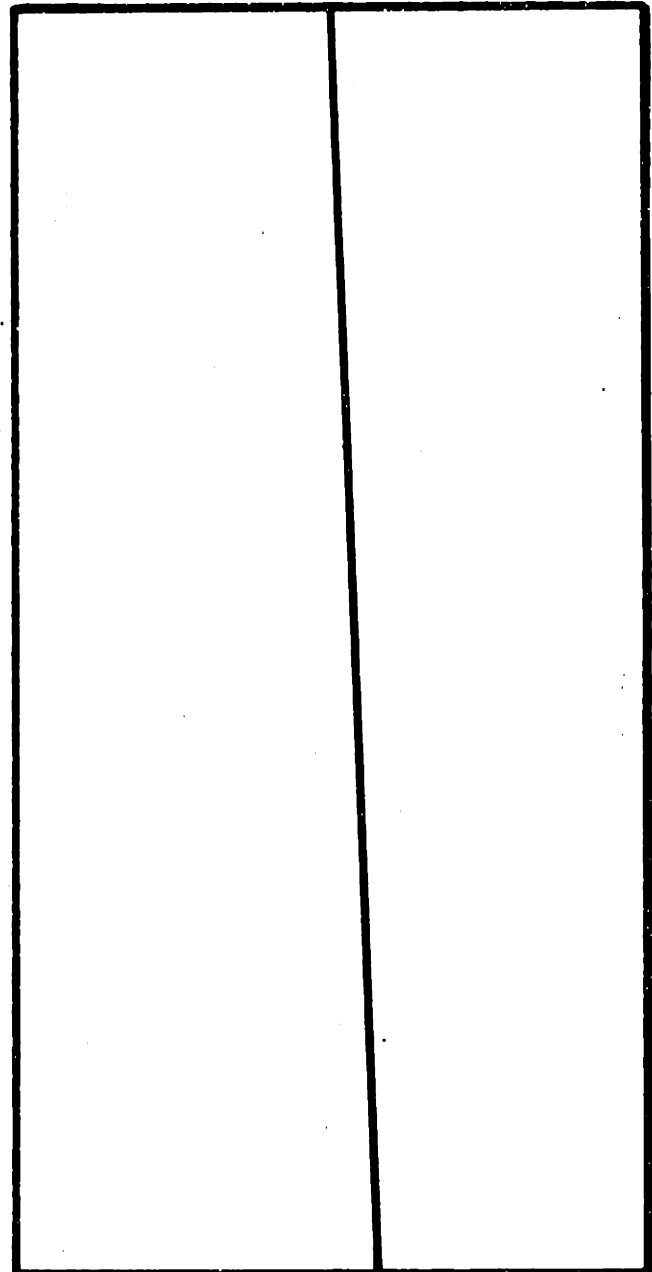
FIG. 35 1st BENDING (1st) MODE OF A

[0/+45/90]_s PLATE



CALCULATED MODE SHAPE

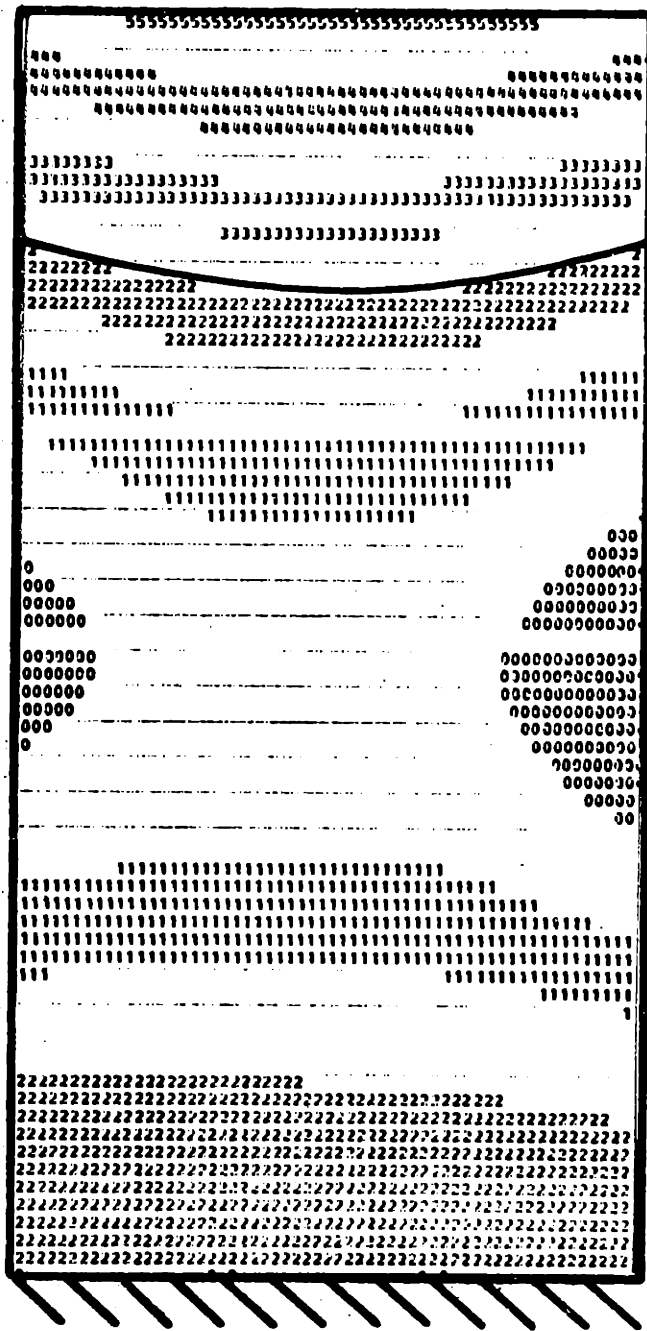
176.3 Hz



OBSERVED MODE SHAPE

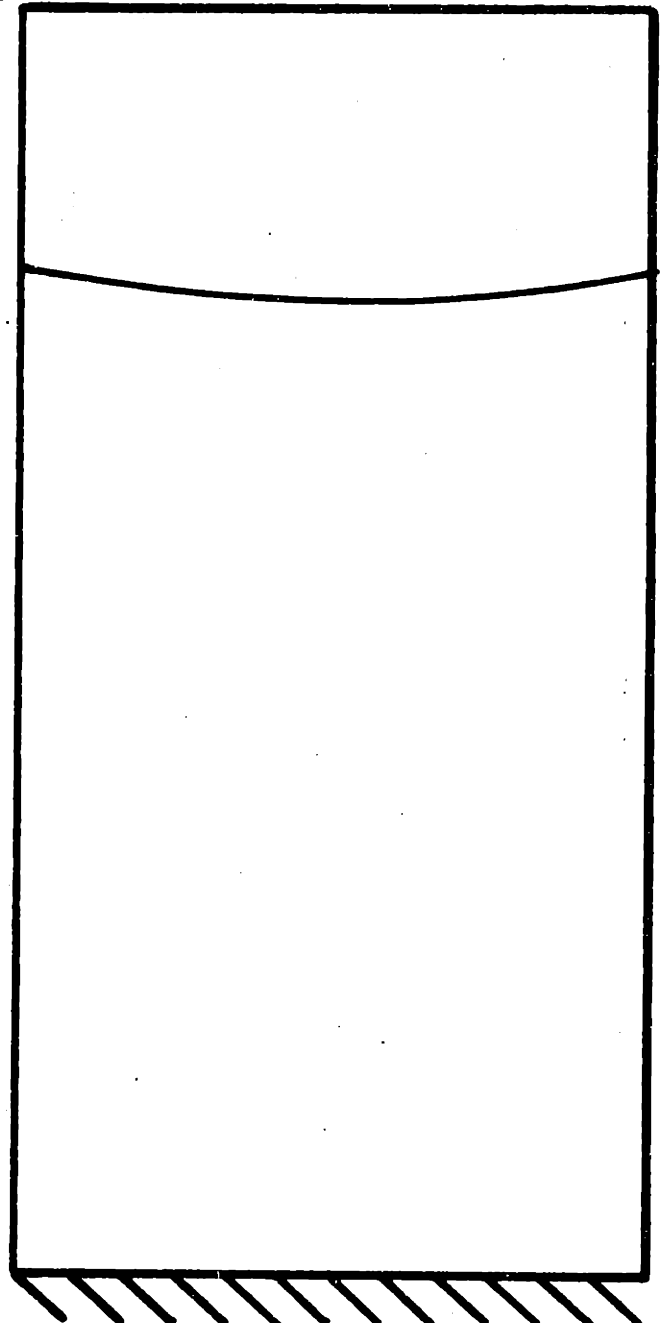
169 Hz

FIG. 36 1st TORSION (2nd) MODE OF A
 $[0/_{\pm}45/90]_s$ PLATE



CALCULATED MODE SHAPE

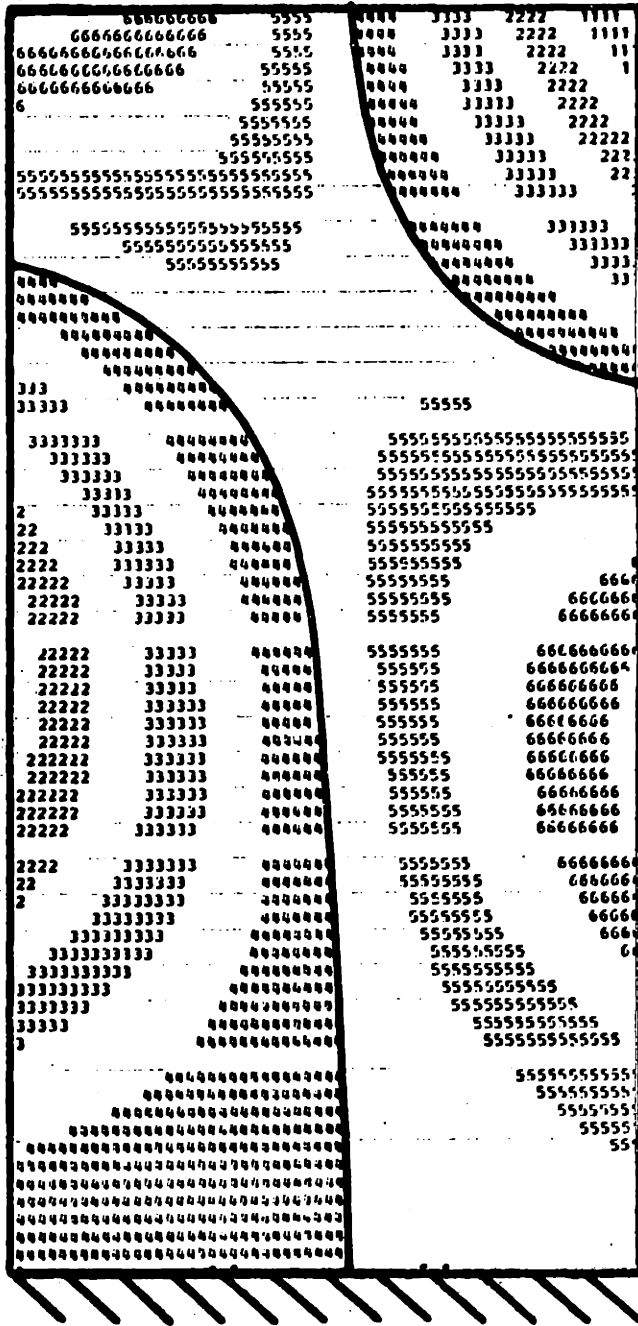
345.9 Hz



OBSERVED MODE SHAPE

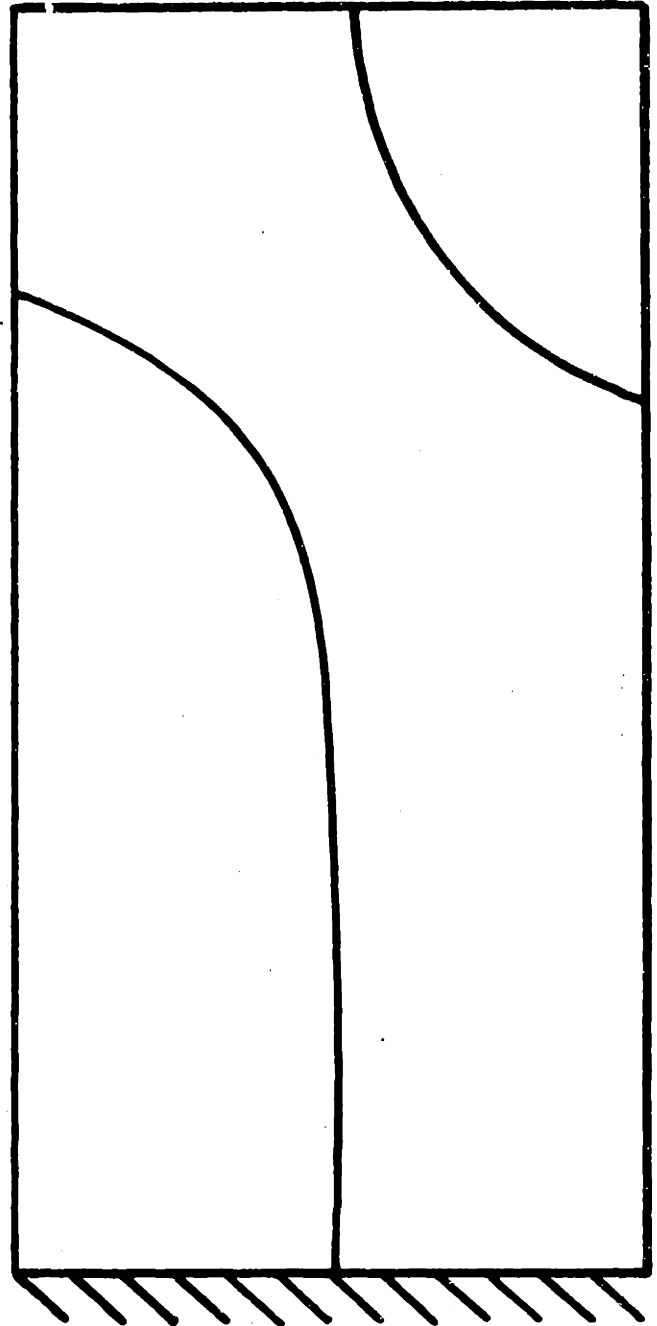
303.0 Hz

FIG. 37 2nd BENDING (3rd) MODE OF A
 $[0/+45/90]_s$ PLATE



CALCULATED MODE SHAPE

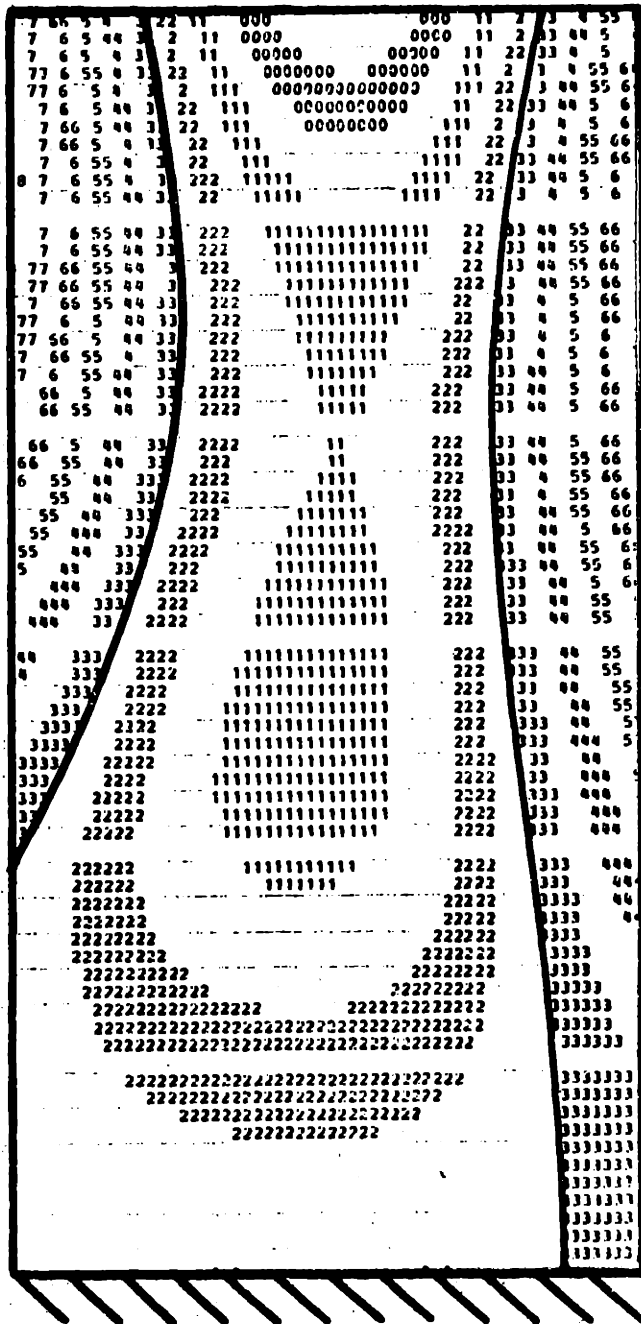
592.2 Hz



OBSERVED MODE SHAPE

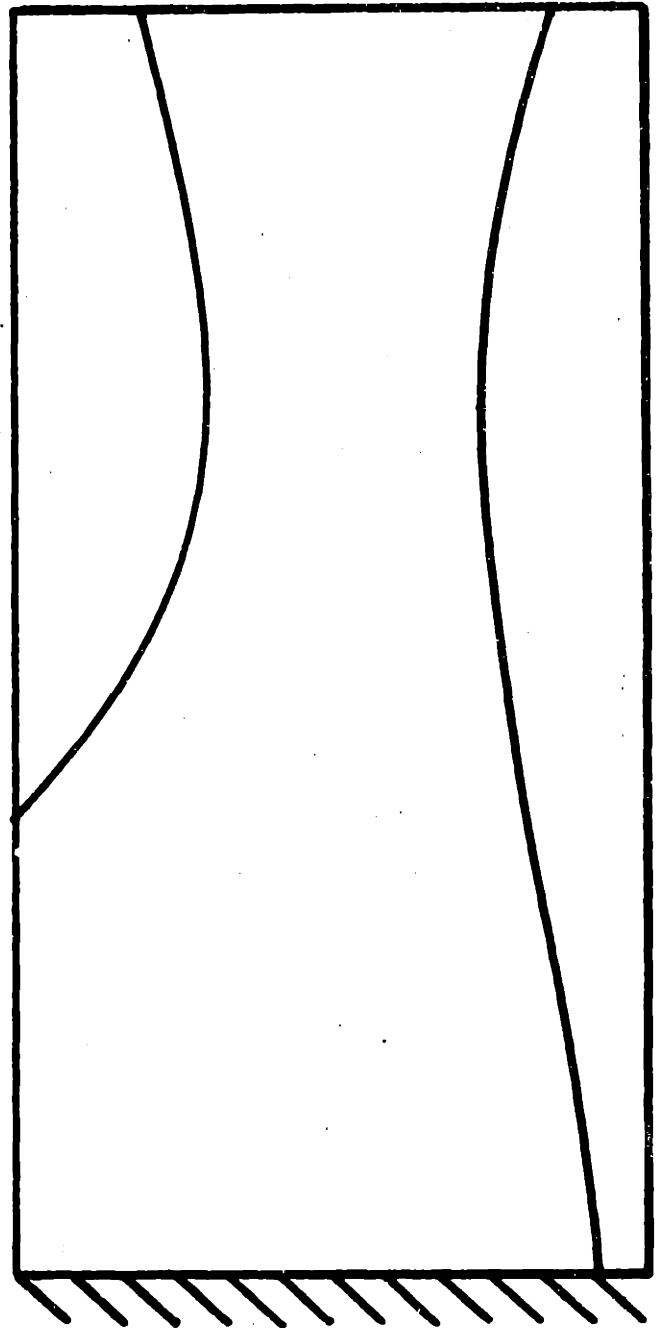
554. Hz

FIG. 38 2nd TORSION (4th) MODE OF A
 $[0/+45/90]_s$ PLATE



CALCULATED MODE SHAPE

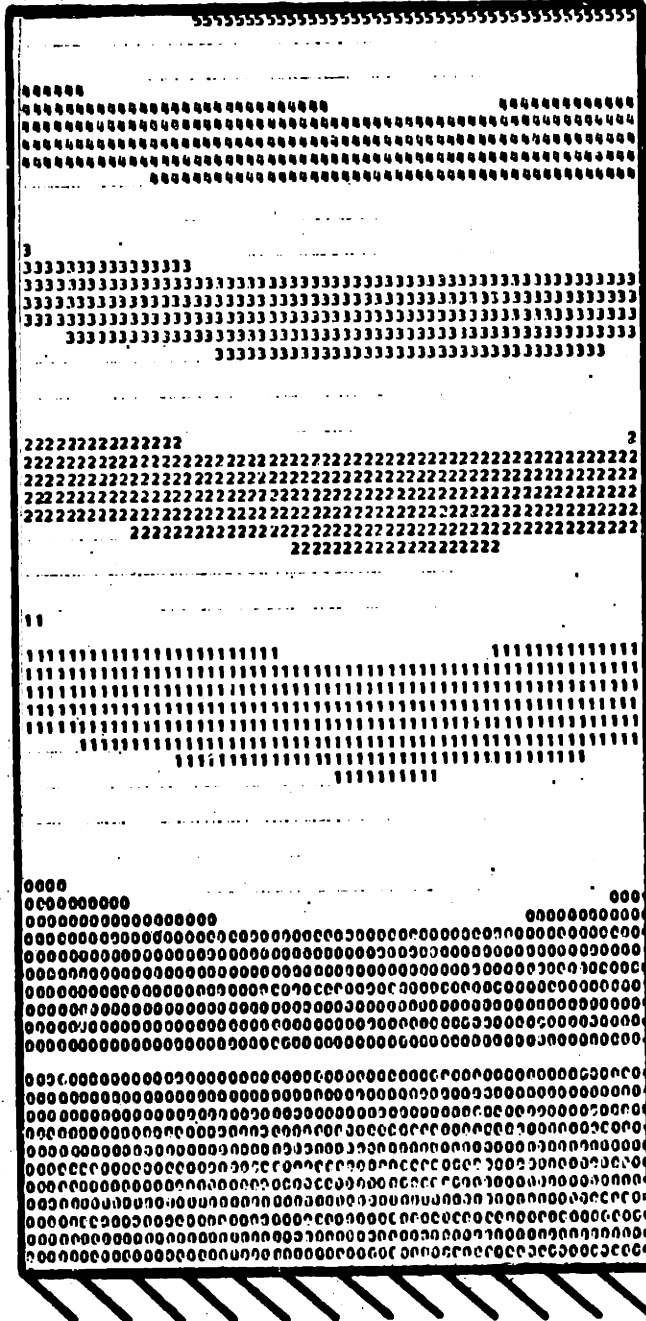
820.4 Hz



OBSERVED MODE SHAPE

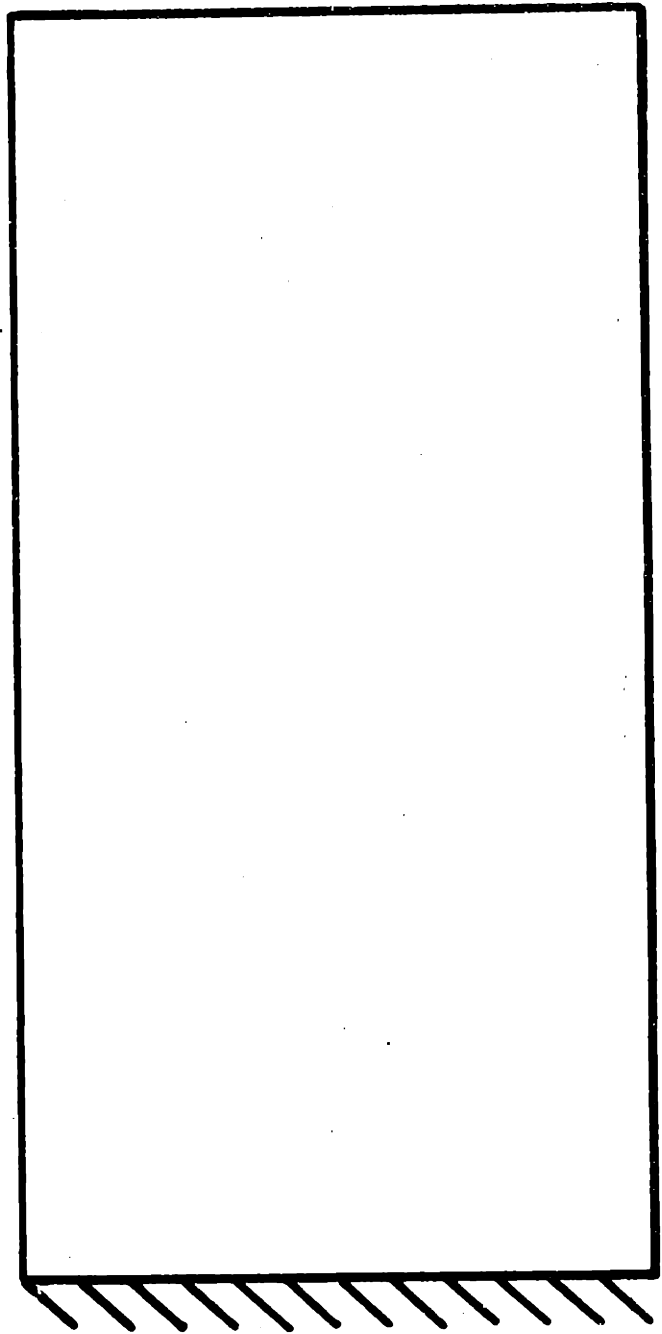
739 Hz

FIG. 39 1st CHORDWISE (5th) MODE OF A
 $[0/_{\pm 45/90}]_s$ PLATE



CALCULATED MODE SHAPE

(39.05) Hz

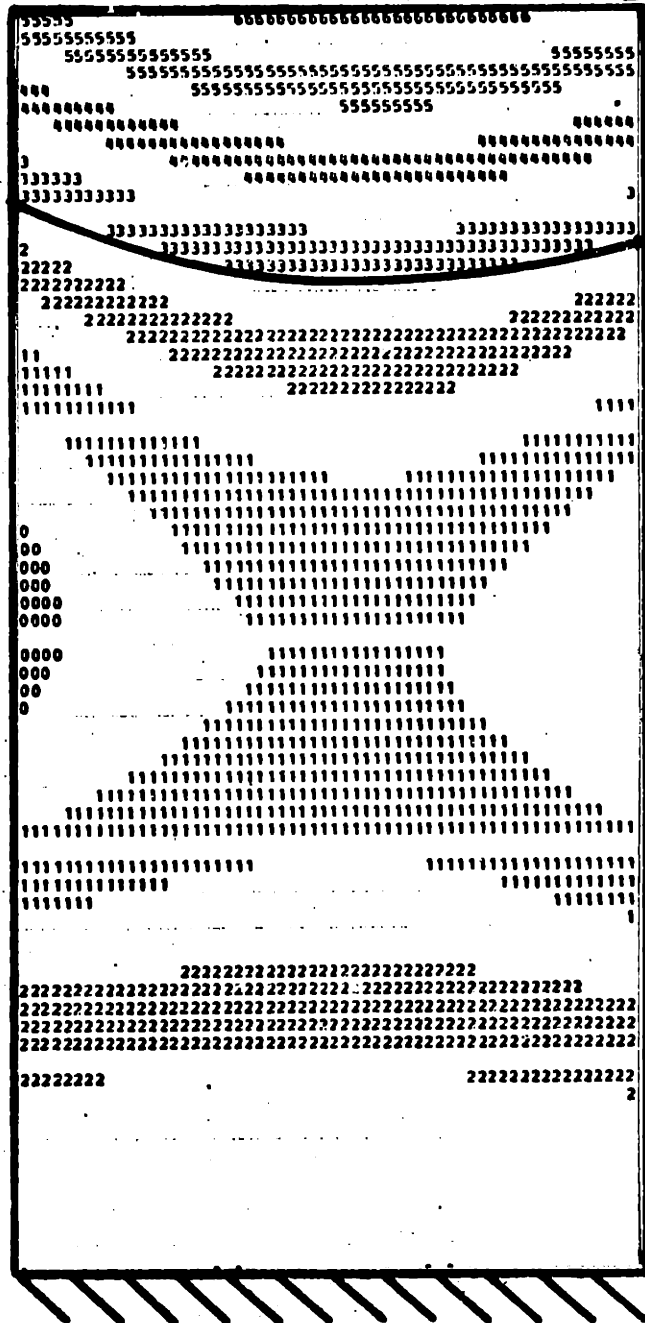


OBSERVED MODE SHAPE

31.3 Hz

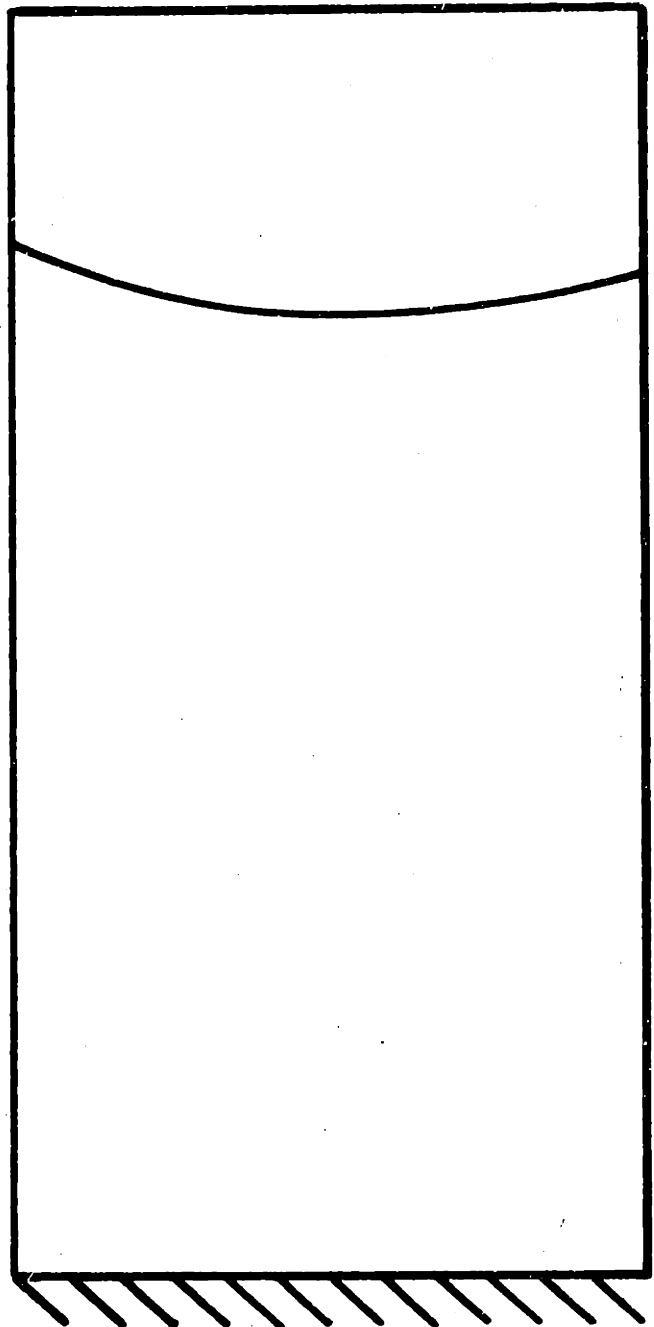
FIG. 40 1st BENDING (1st) MODE OF A

[+45/-45]_s PLATE



CALCULATED MODE SHAPE

192.8 Hz

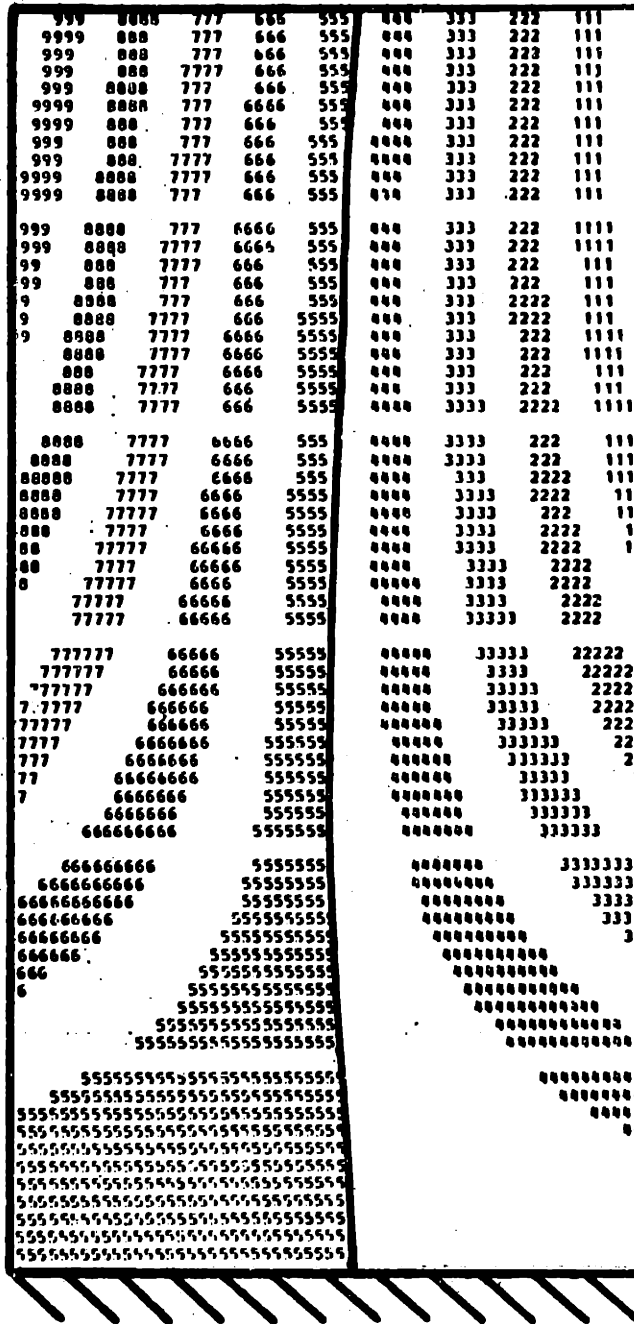


OBSERVED MODE SHAPE

185.8 Hz

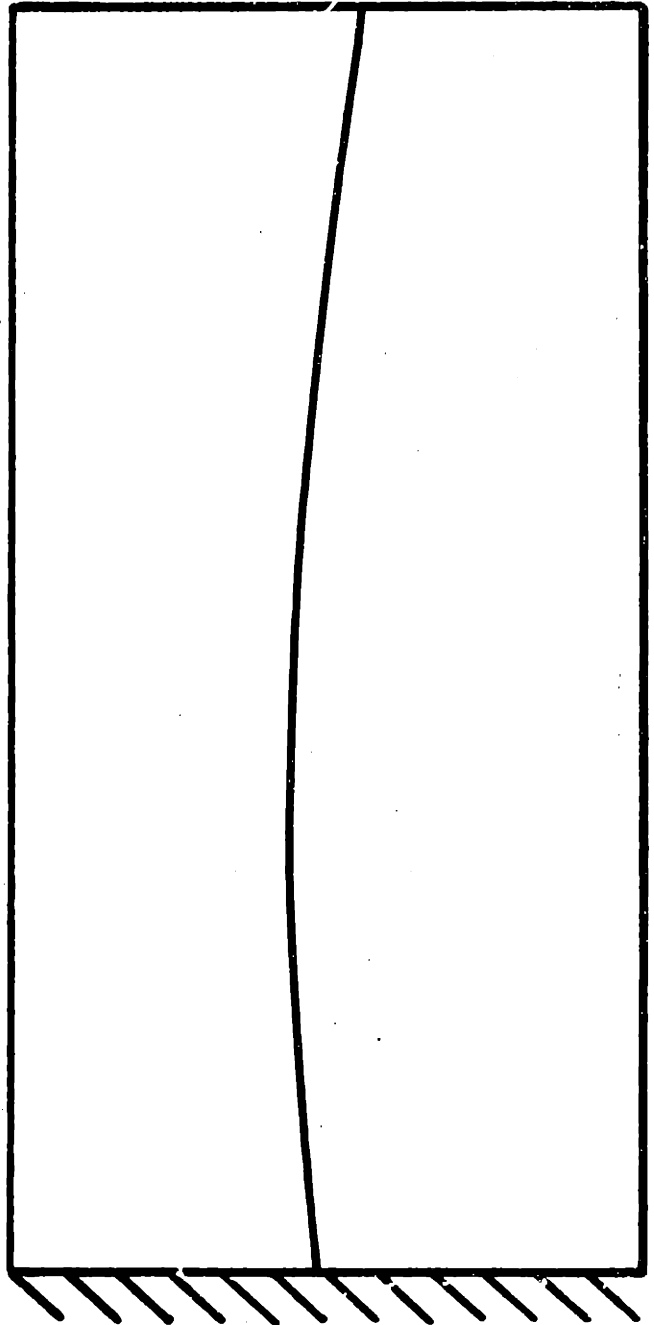
FIG. 41 2nd BENDING (2nd) MODE OF A

[+45/-45]_s PLATE



CALCULATED MODE SHAPE

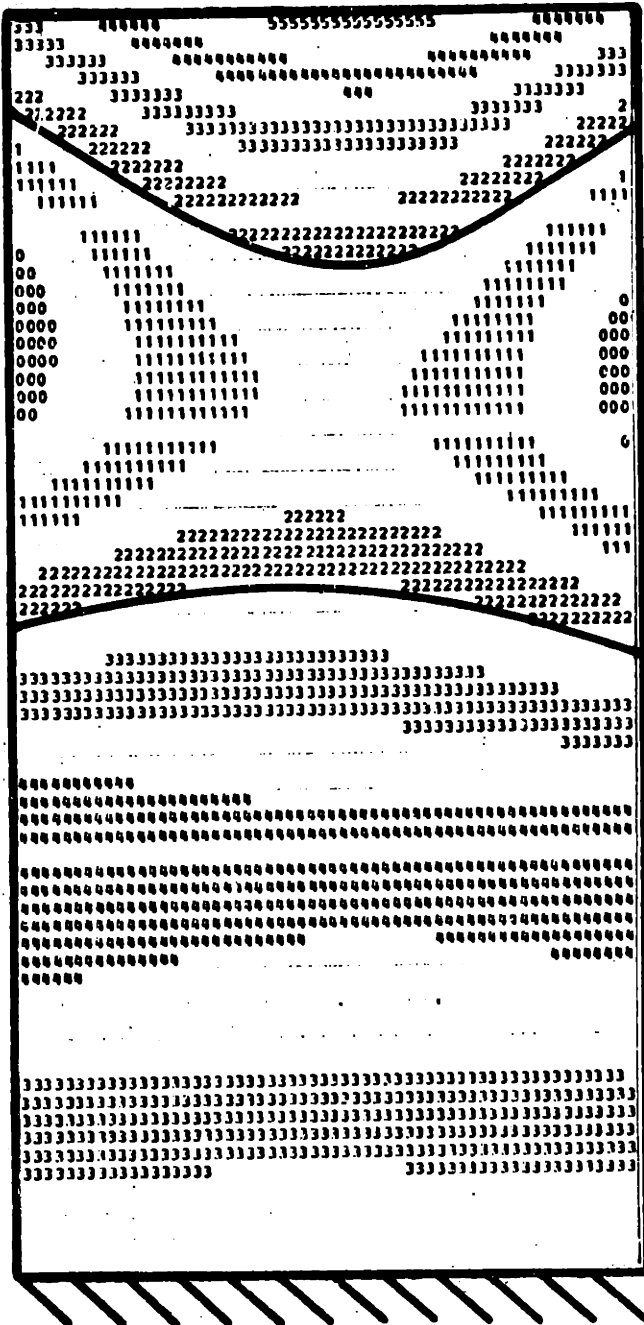
229.3 Hz



OBSERVED MODE SHAPE

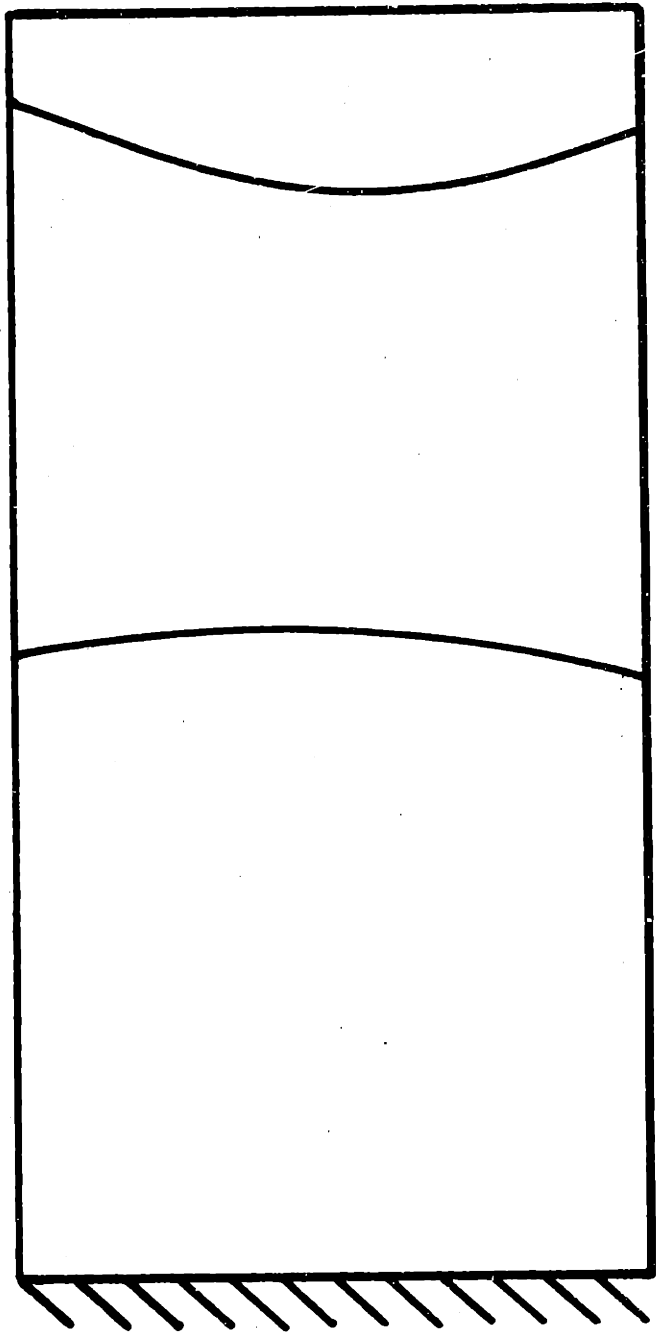
214 Hz

FIG. 42 1st TORSION (3rd) MODE OF A
 $[+45/\bar{+45}]_s$ PLATE



CALCULATED MODE SHAPE

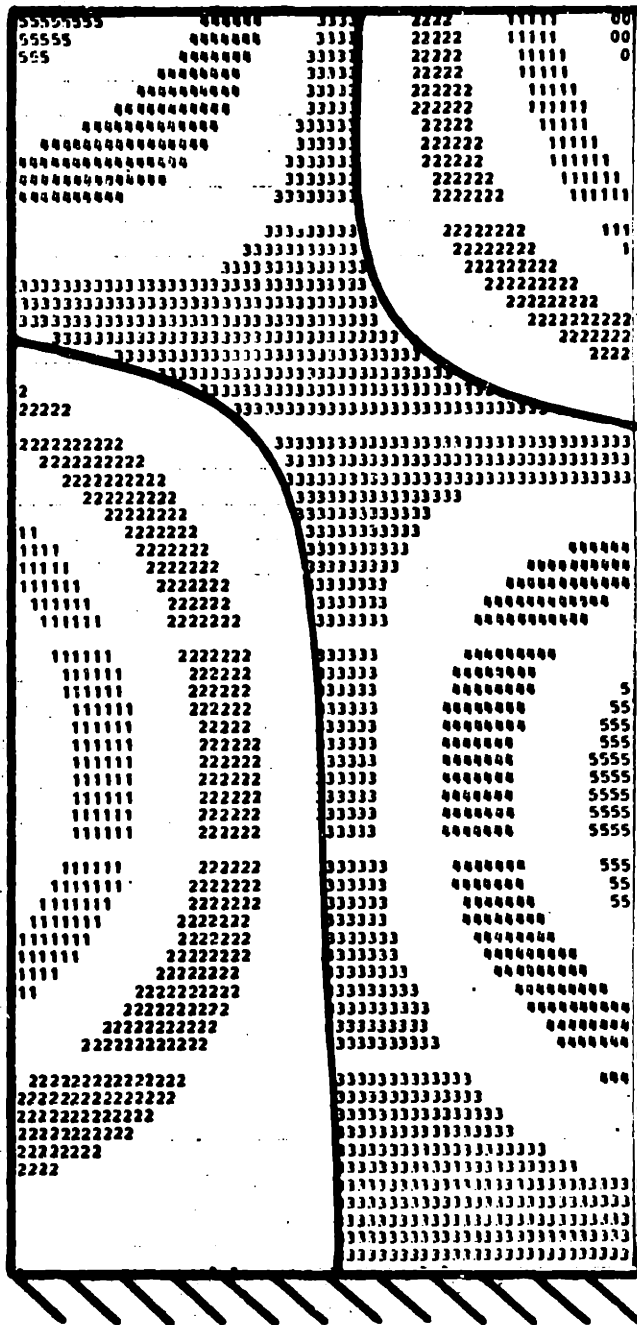
565.8 Hz



OBSERVED MODE SHAPE

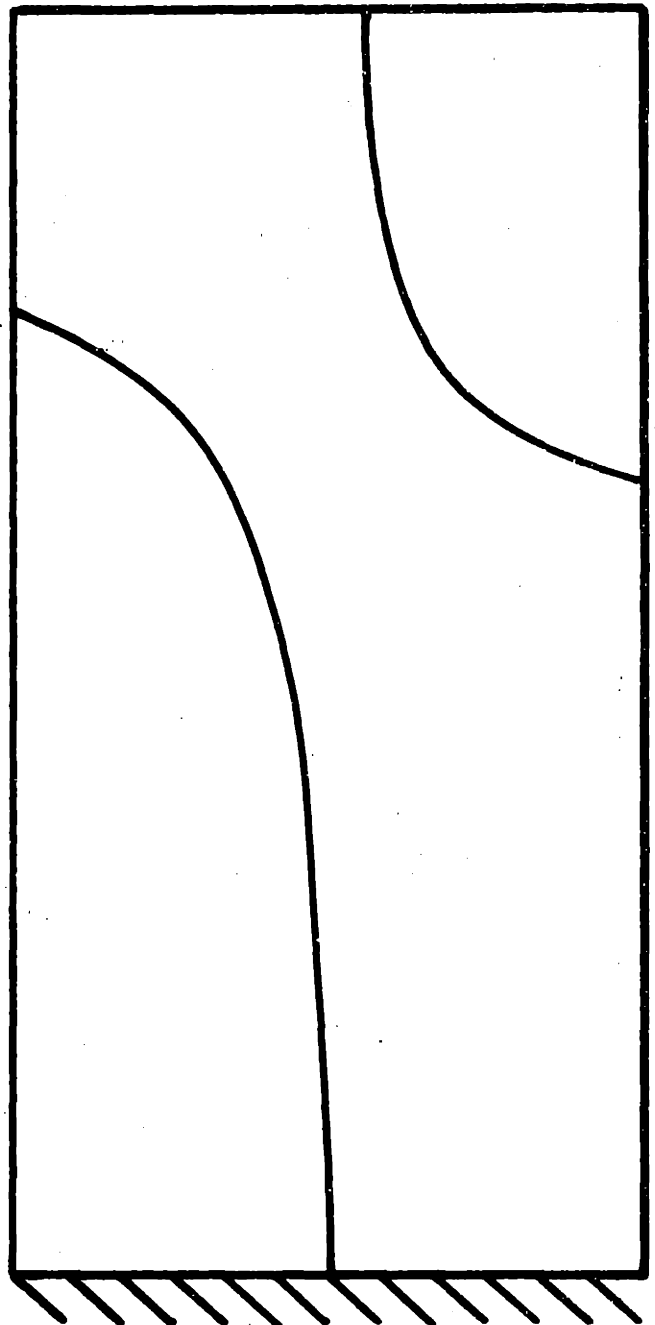
533. Hz

FIG. 43 3rd BENDING (4th) MODE OF A
 $[\pm 45/\mp 45]_s$ PLATE



CALCULATED MODE SHAPE

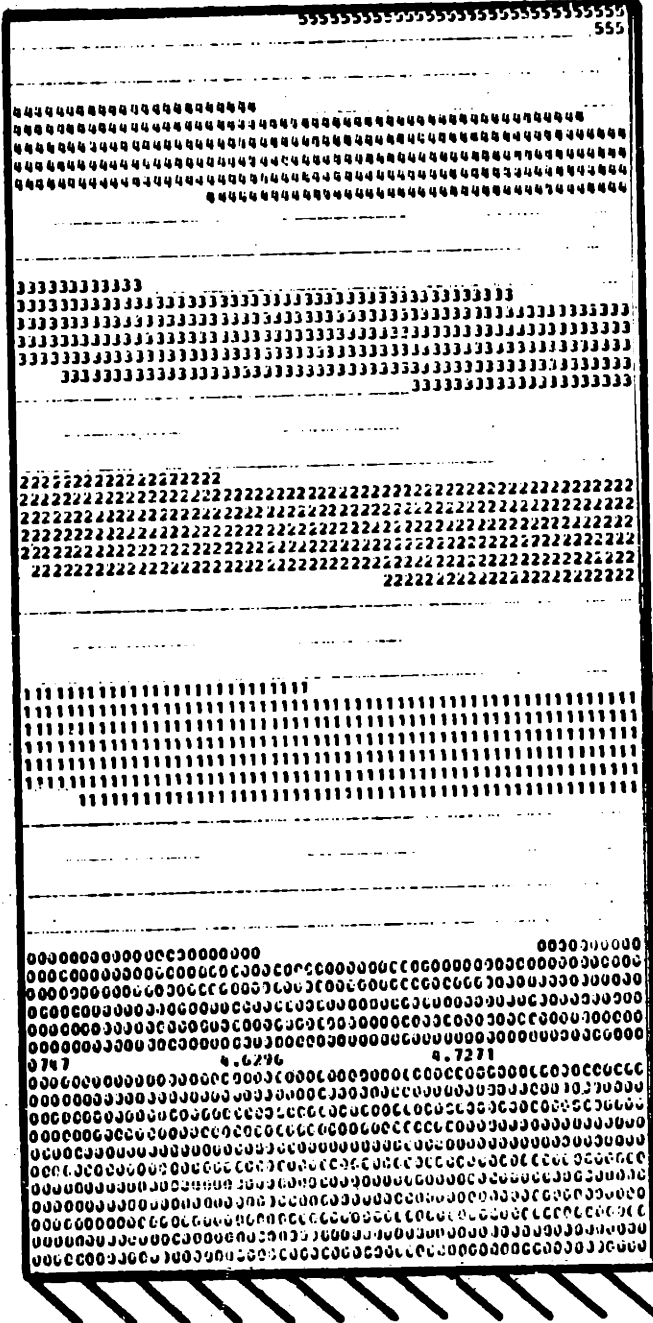
707.6 Hz



OBSERVED MODE SHAPE

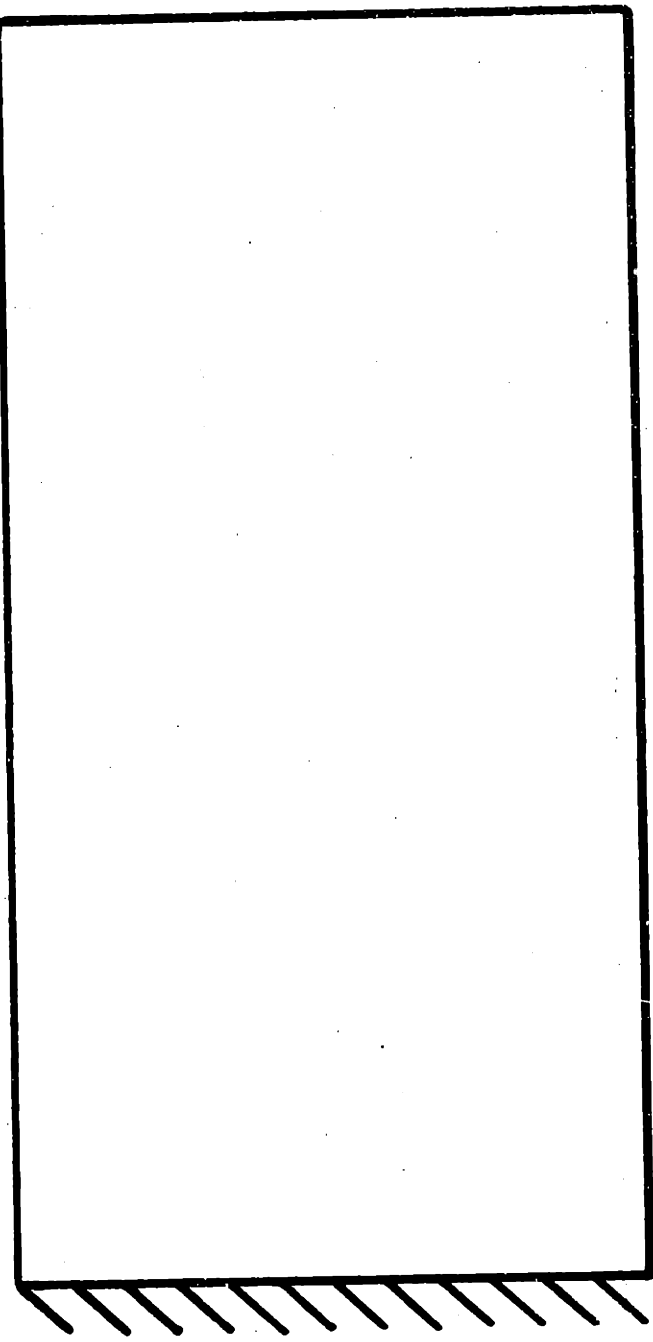
653. Hz

FIG. 44 2nd TORSION (5th) MODE OF A
 $[+45/\bar{45}]_s$ PLATE



CALCULATED MODE SHAPE

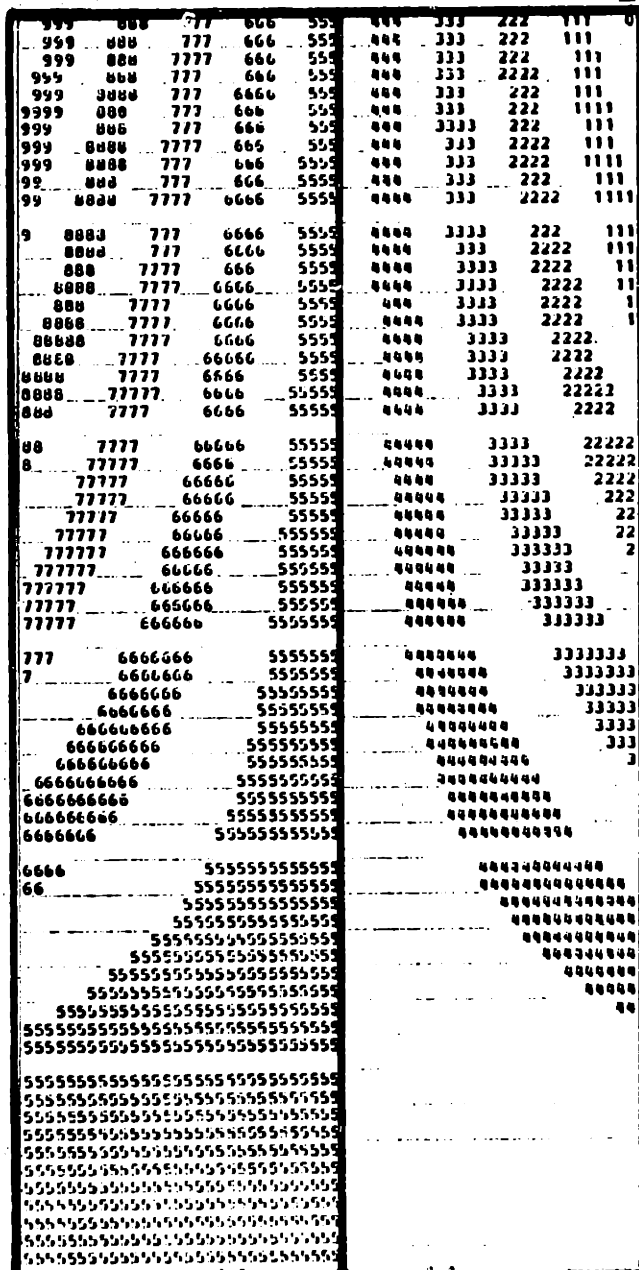
113.8 Hz



OBSERVED MODE SHAPE

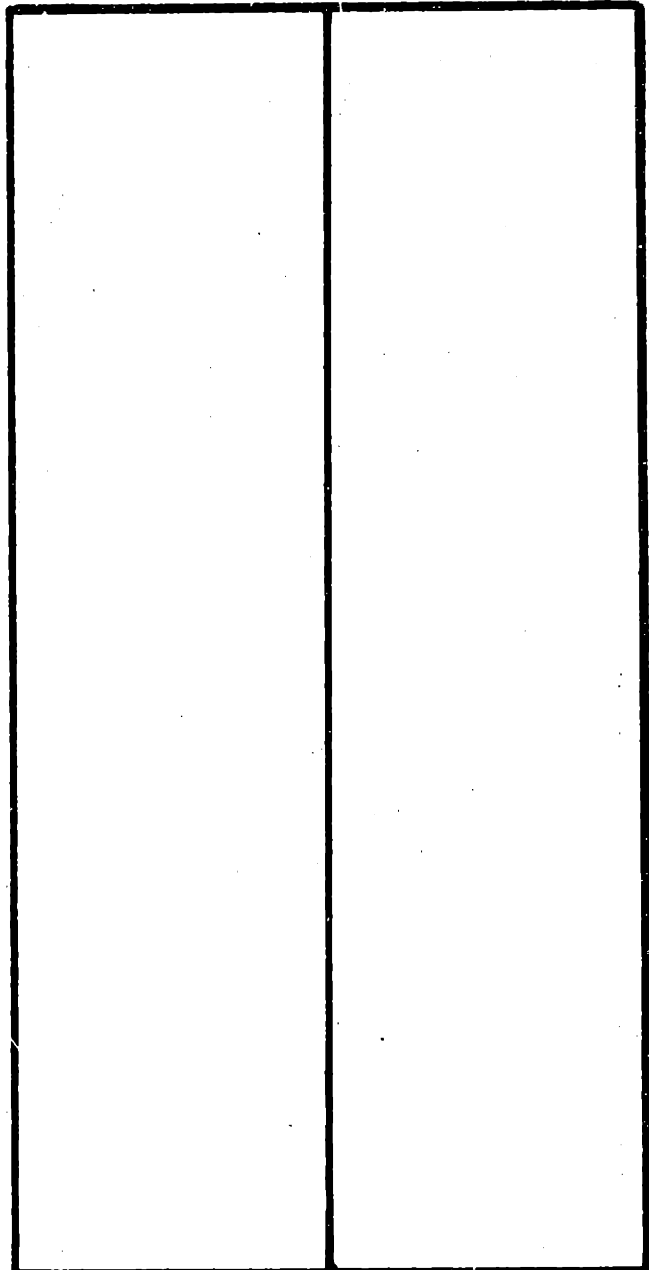
101.7 Hz

FIG. 45 1st BENDING (1st) MODE OF A
[0₄/Al]_s PLATE



CALCULATED MODE SHAPE

229.3 Hz

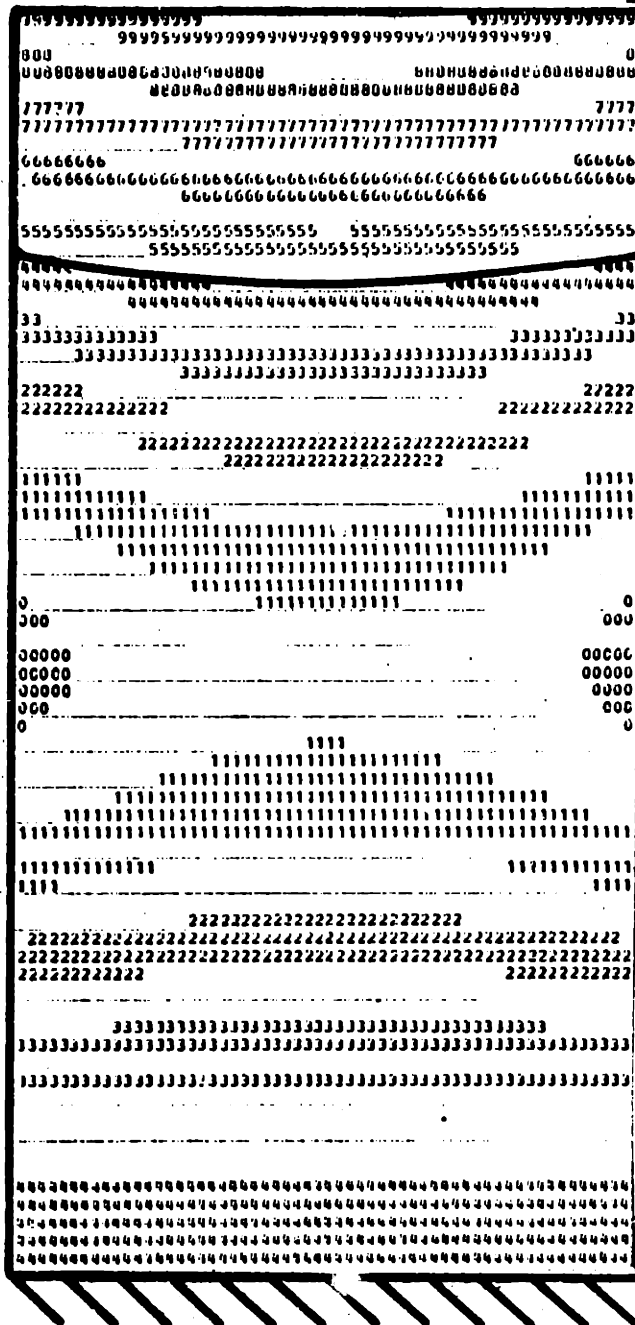


OBSERVED MODE SHAPE

229. Hz

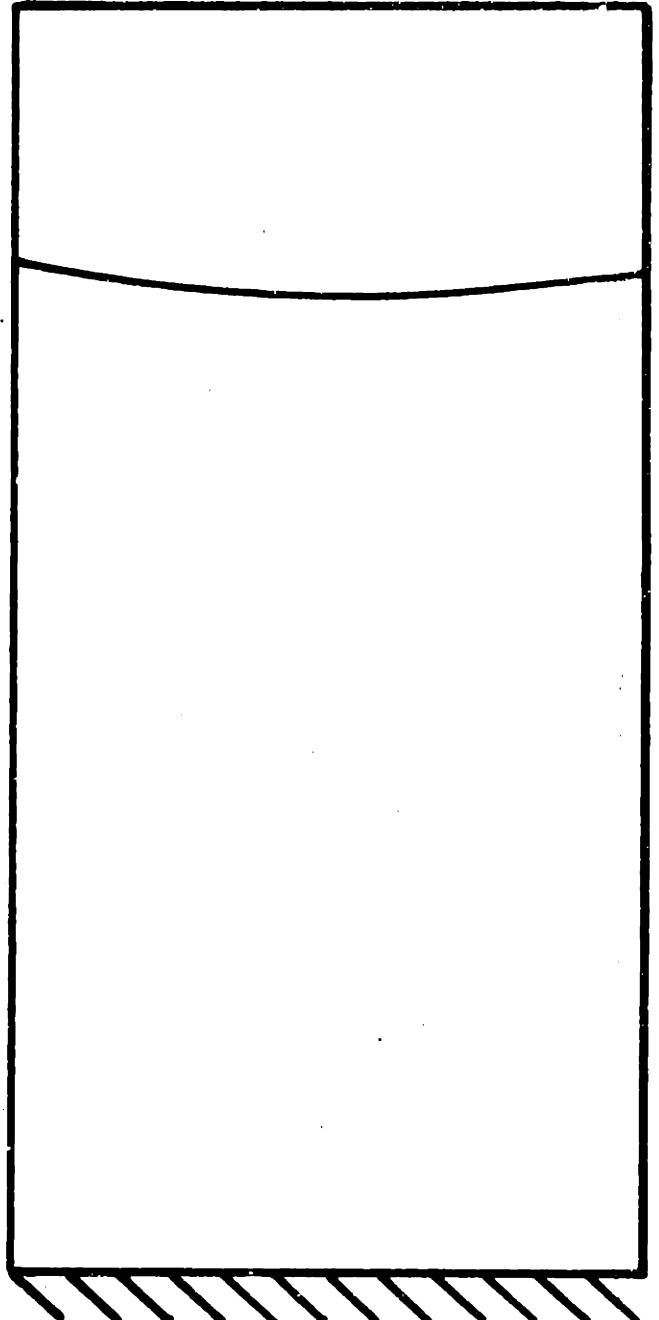
FIG. 46 1st TORSION (2nd) MODE OF A

[0₄/A1]₈ PLATE



CALCULATED MODE SHAPE

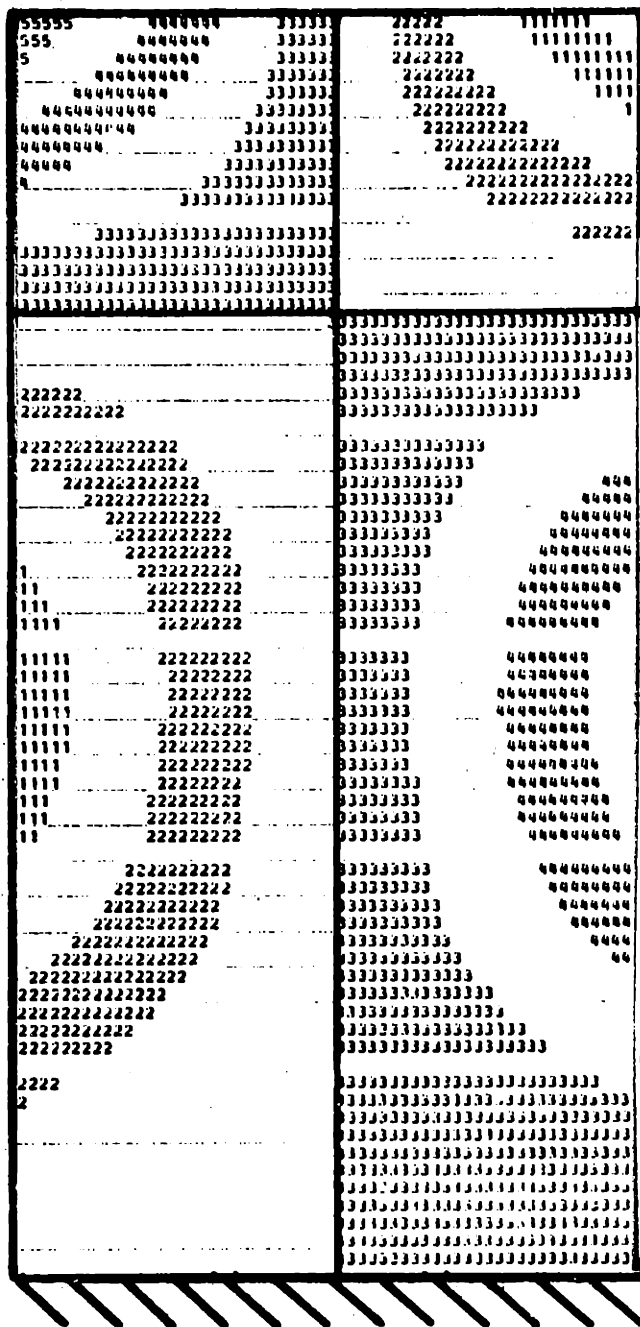
680.9 Hz



OBSERVED MODE SHAPE

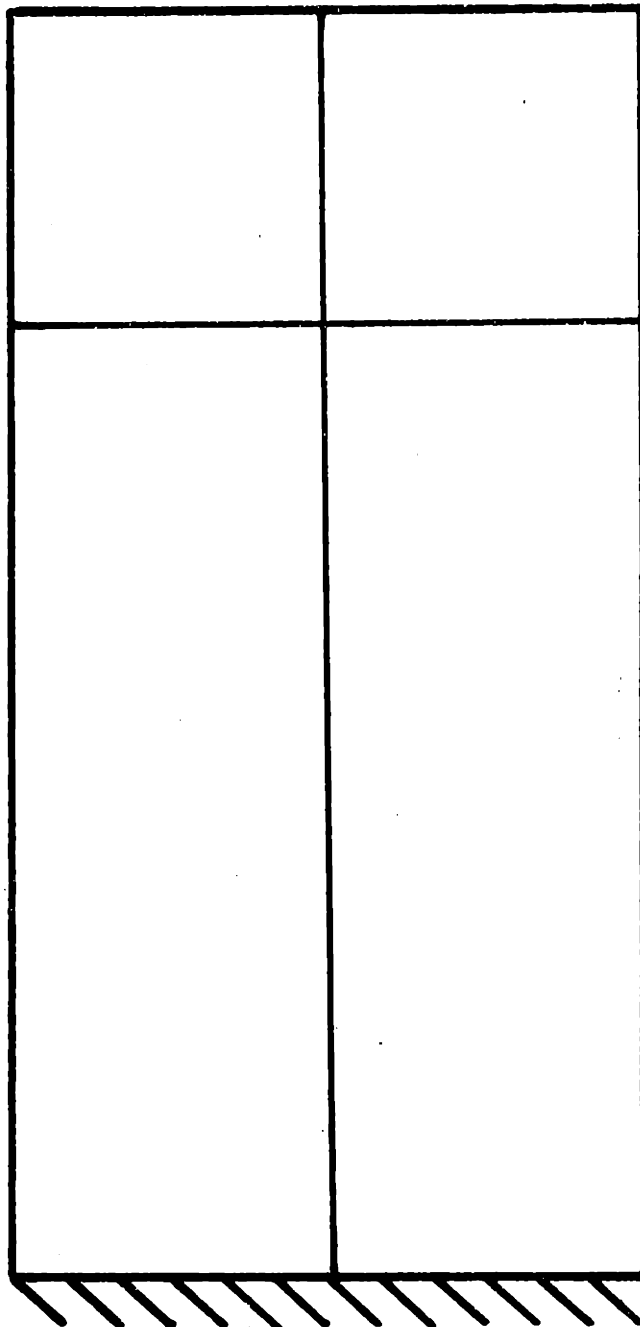
631.2 Hz

FIG. 47 2nd BENDING (3rd) MODE OF A
 $[0_4/A1]_s$ PLATE



CALCULATED MODE SHAPE

885.8 Hz

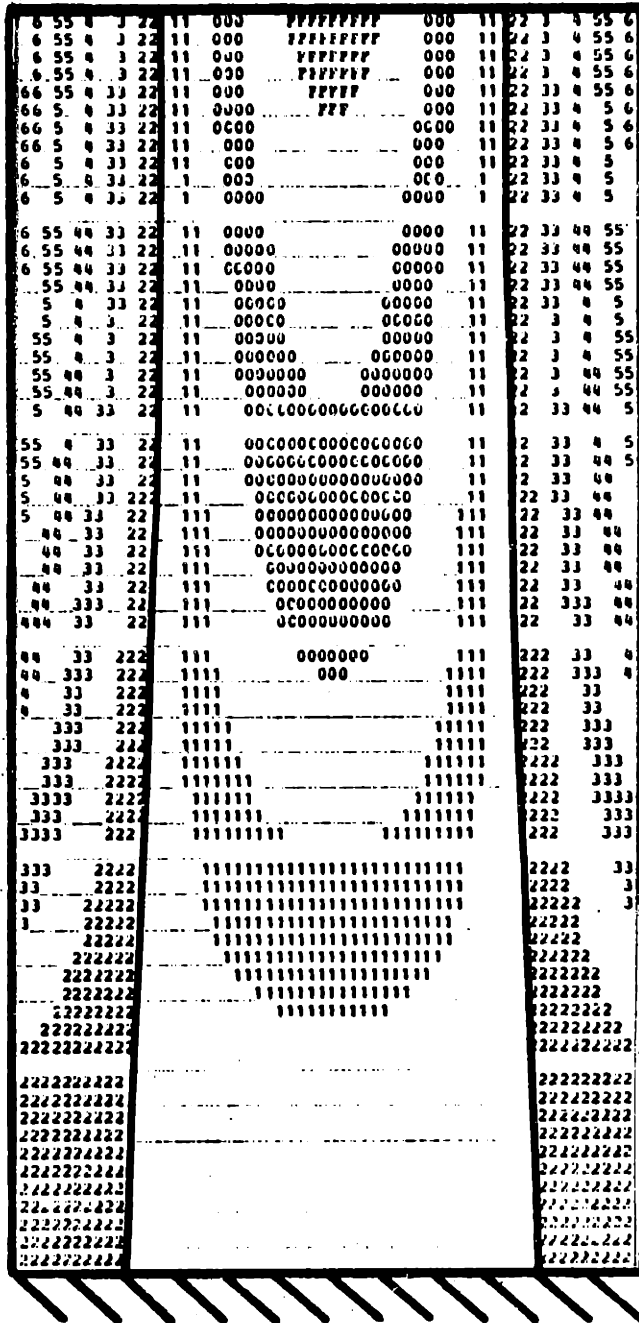


OBSERVED MODE SHAPE

865 Hz

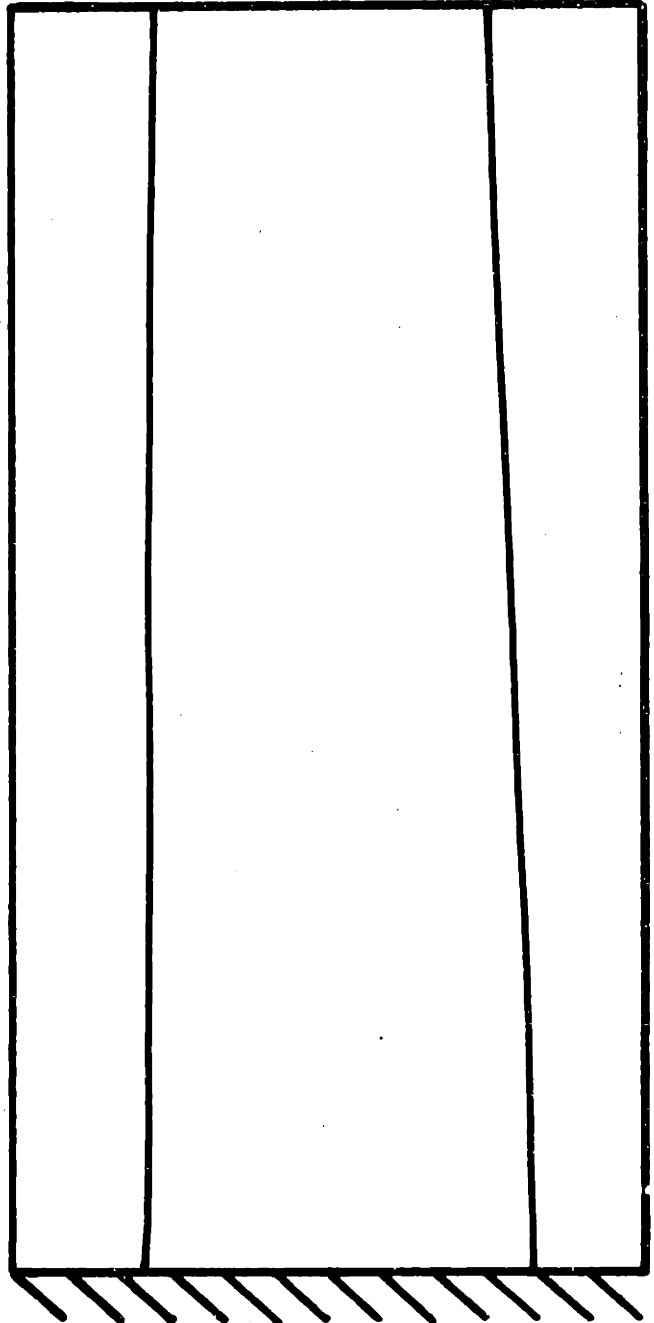
FIG. 48 2nd TORSION (4th) MODE OF A

[0₄/A1]₈ PLATE



CALCULATED MODE SHAPE

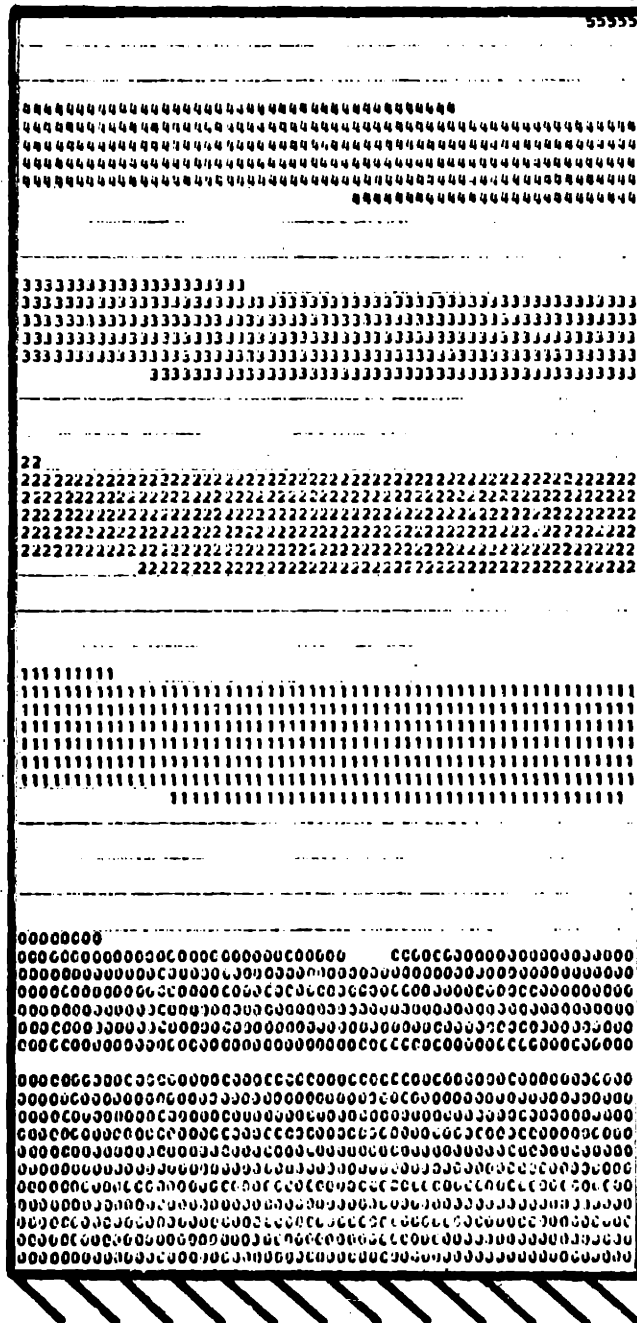
1168. Hz



OBSERVED MODE SHAPE

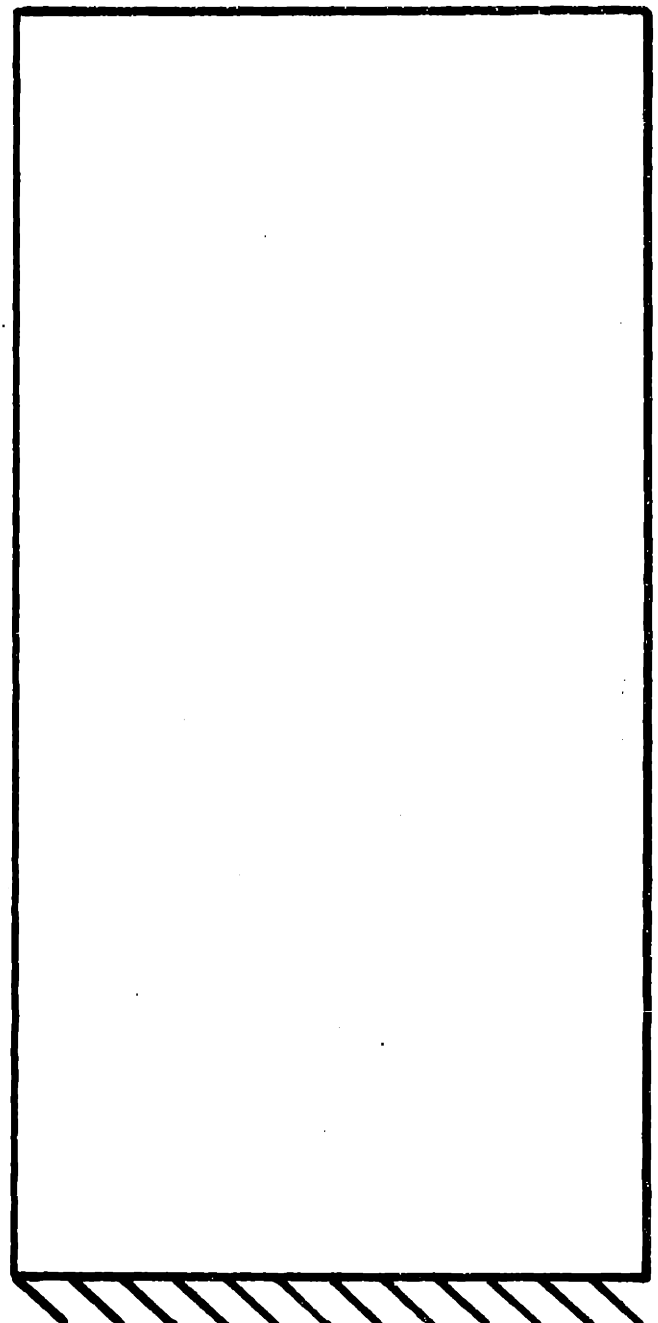
1129. Hz

FIG. 49 1st CHORDWISE (5th) MODE OF A
 $[0_4/A1]_s$ PLATE



CALCULATED MODE SHAPE

86.41 Hz

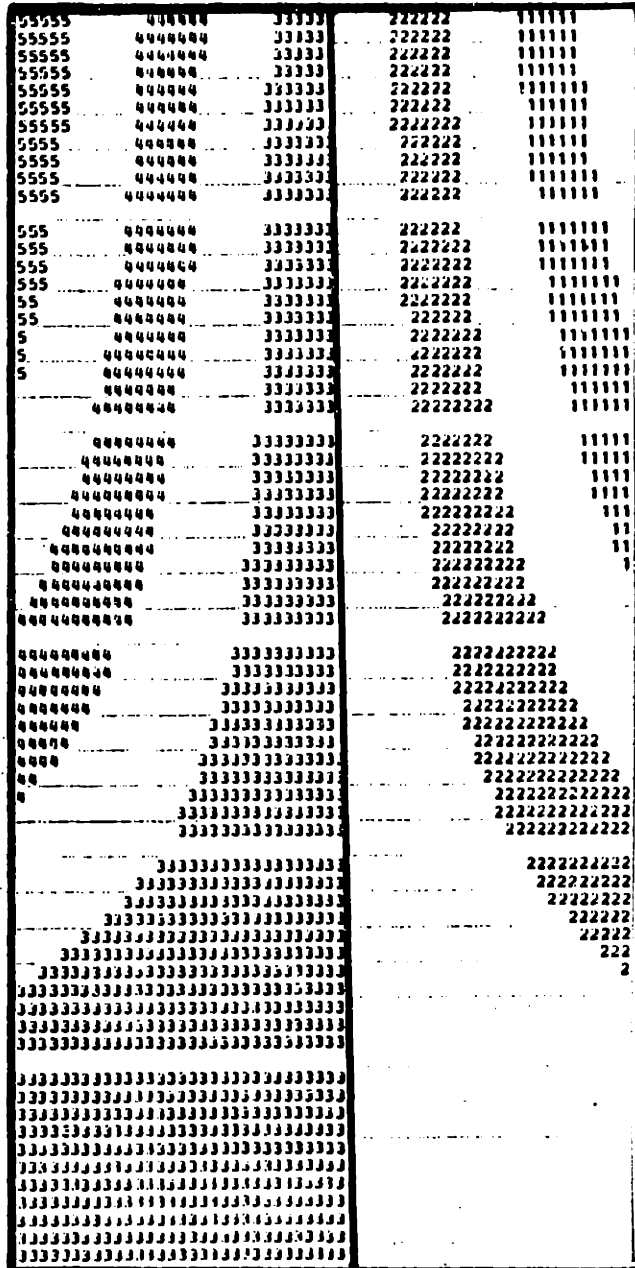


OBSERVED MODE SHAPE

75.9 Hz

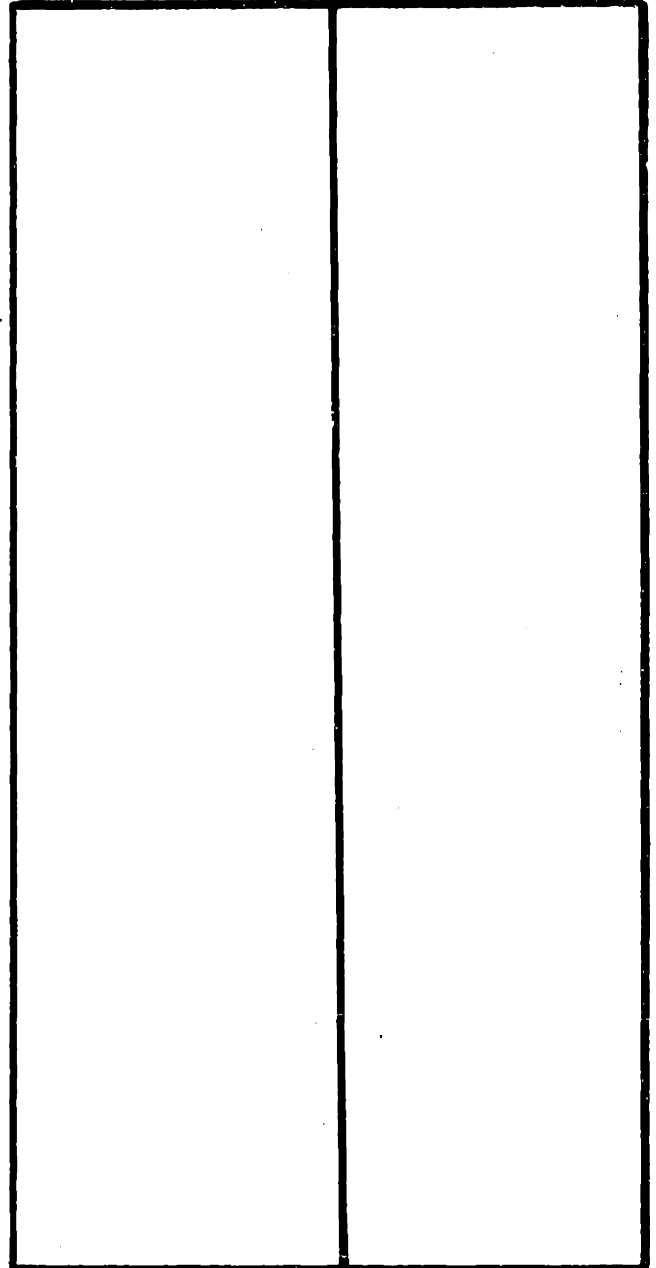
FIG. 50 1st BENDING (1st) MODE OF A

[0/+45/90/A1]_g PLATE



CALCULATED MODE SHAPE

314.6 Hz



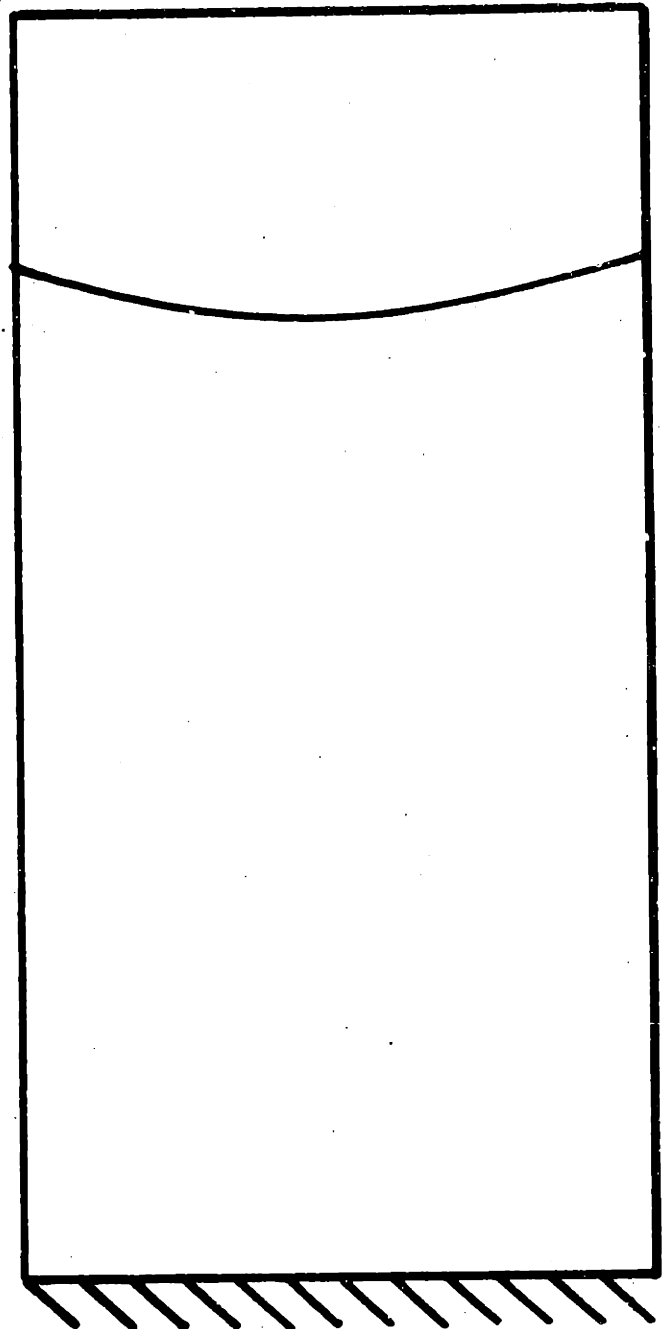
OBSERVED MODE SHAPE

302 Hz

FIG. 51 1st TORSION (2nd) MODE OF A

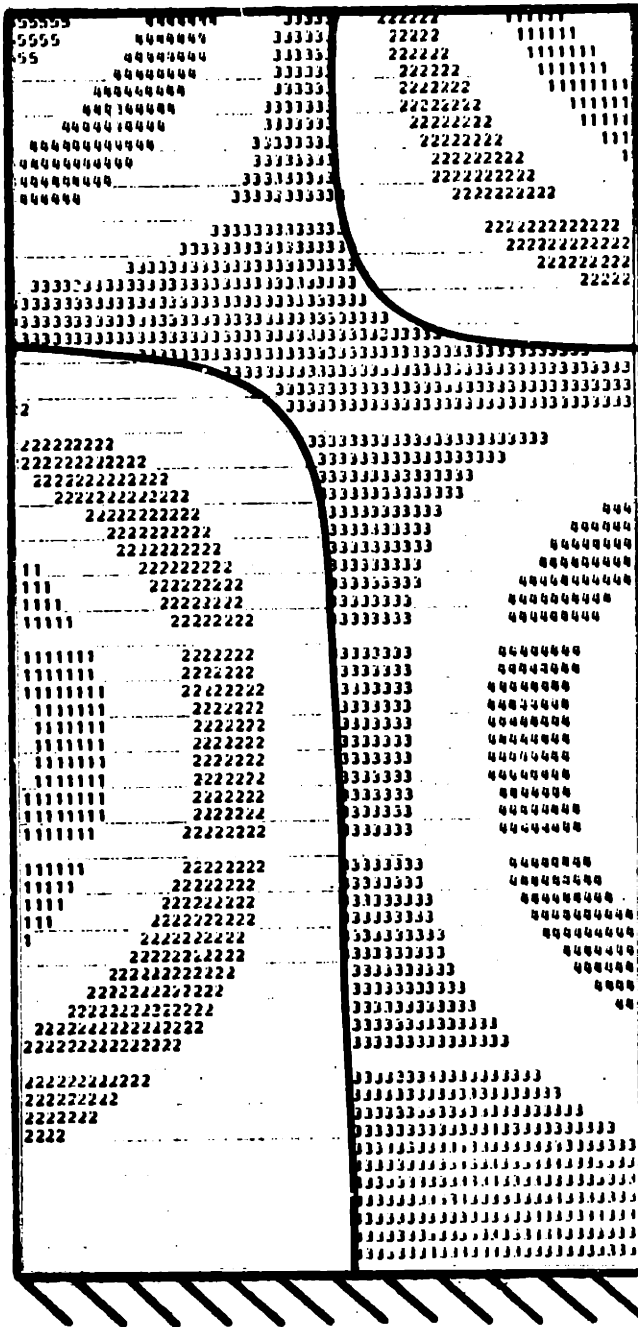
[0/+45/90/A1]_s PLATE

506.1 Hz



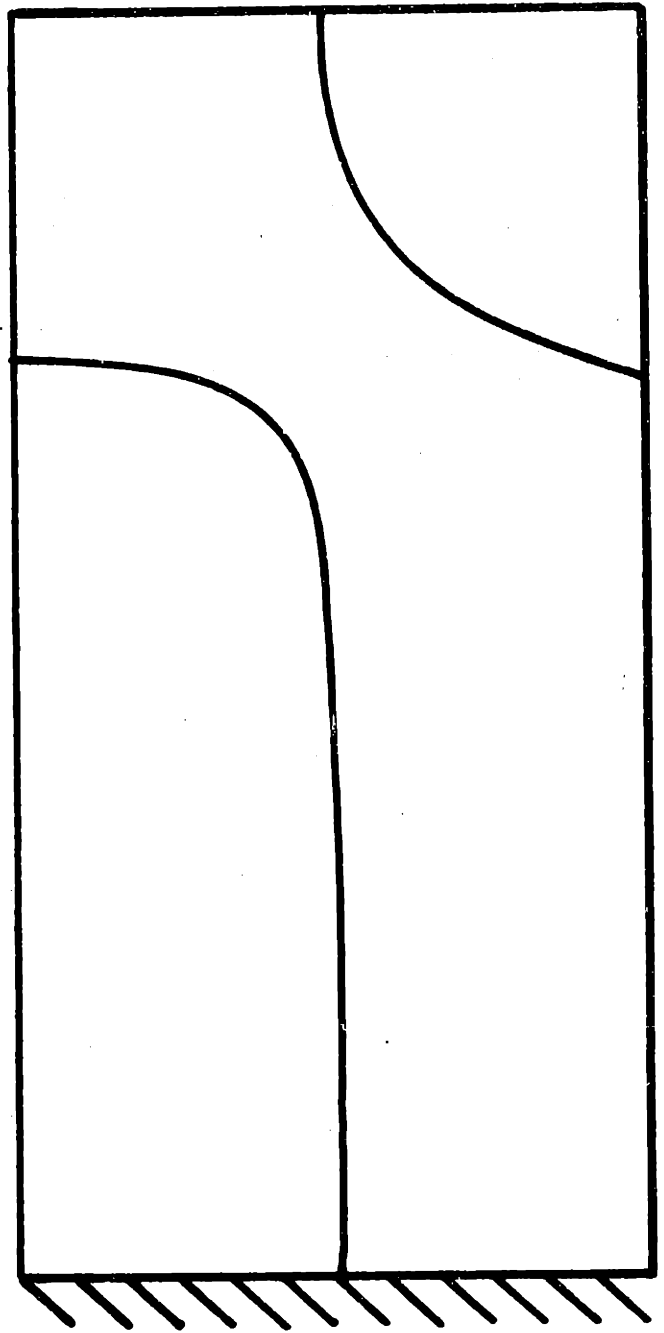
469.6 Hz

**FIG. 52 2nd BENDING (3rd) MODE OF A
[0/+45/90/A1]₈ PLATE**



CALCULATED MODE SHAPE

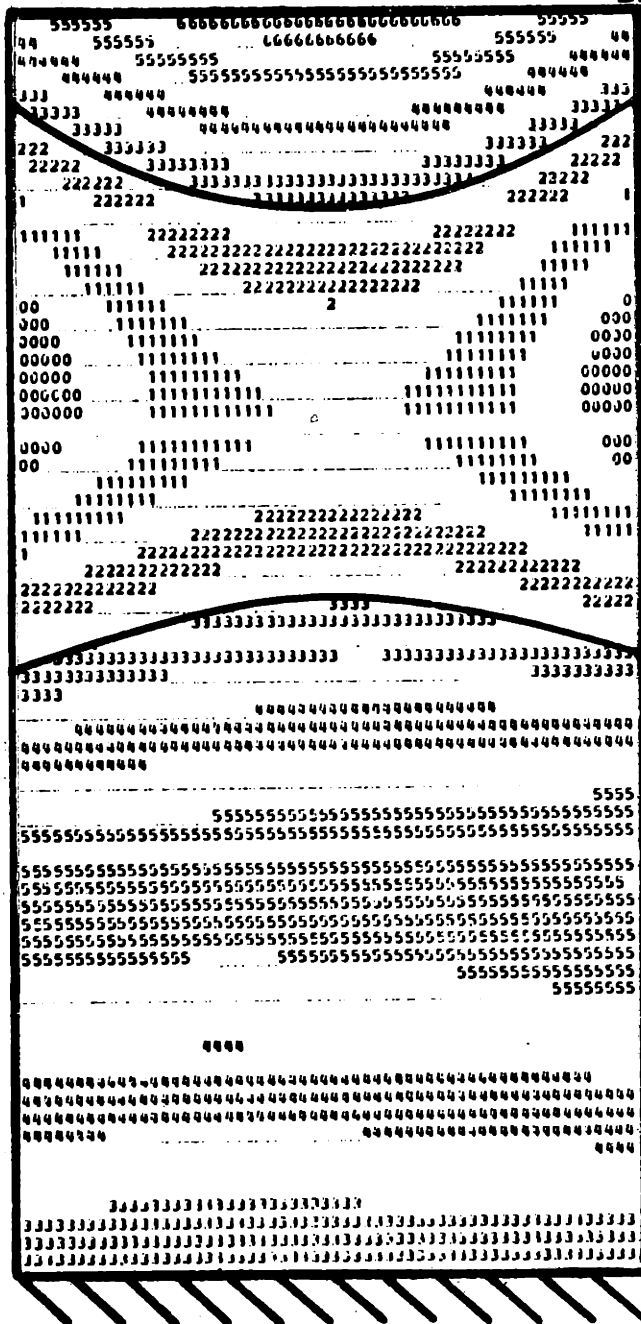
1035 Hz



OBSERVED MODE SHAPE

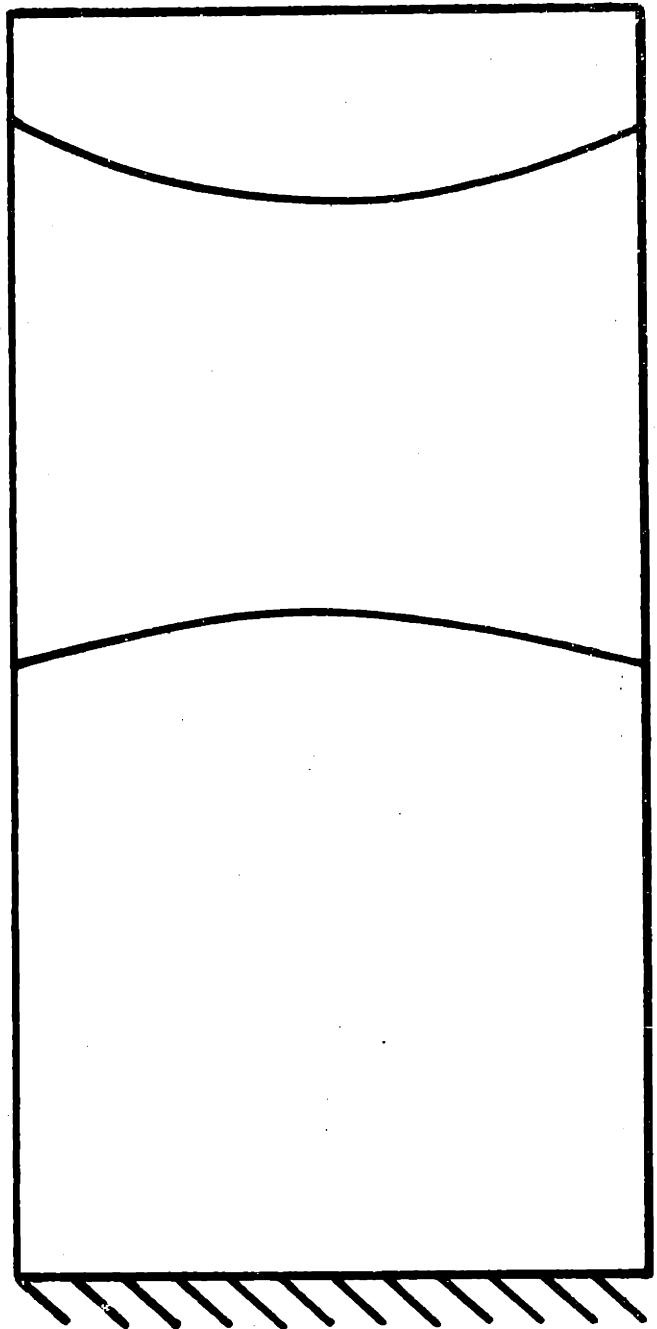
983 Hz

FIG. 53 2nd TORSION (4th) MODE OF A
 $[0/+45/90/A1]_s$ PLATE



CALCULATED MODE SHAPE

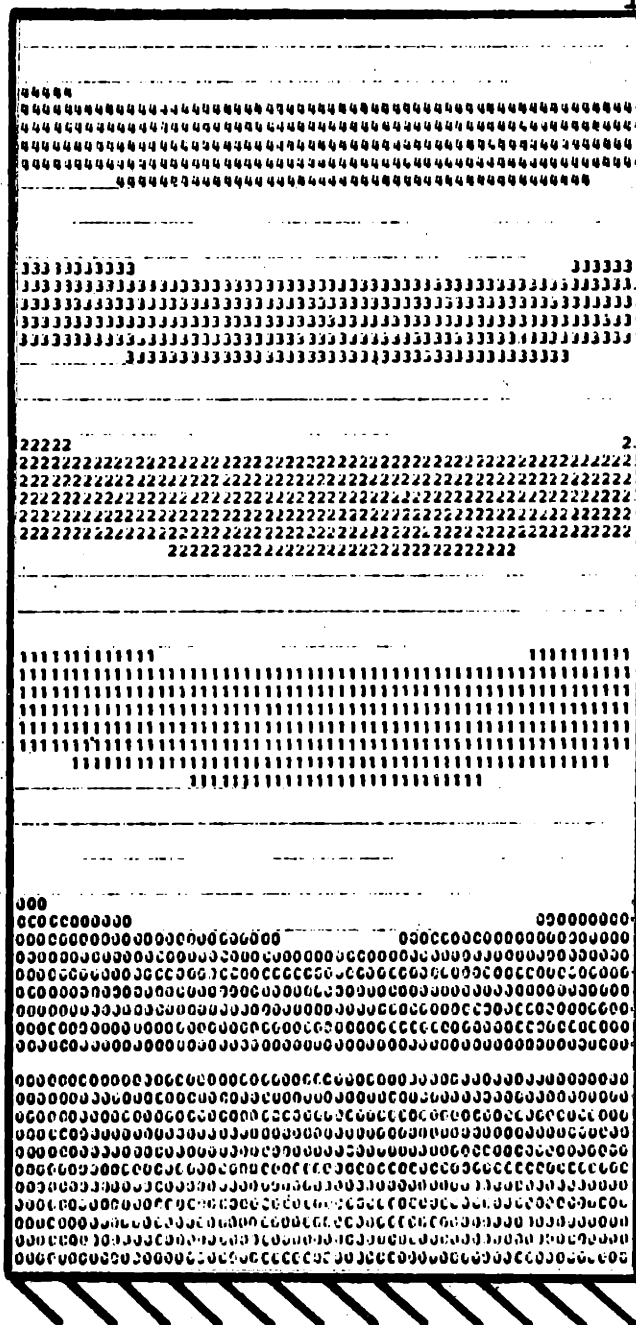
1418 Hz



OBSERVED MODE SHAPE

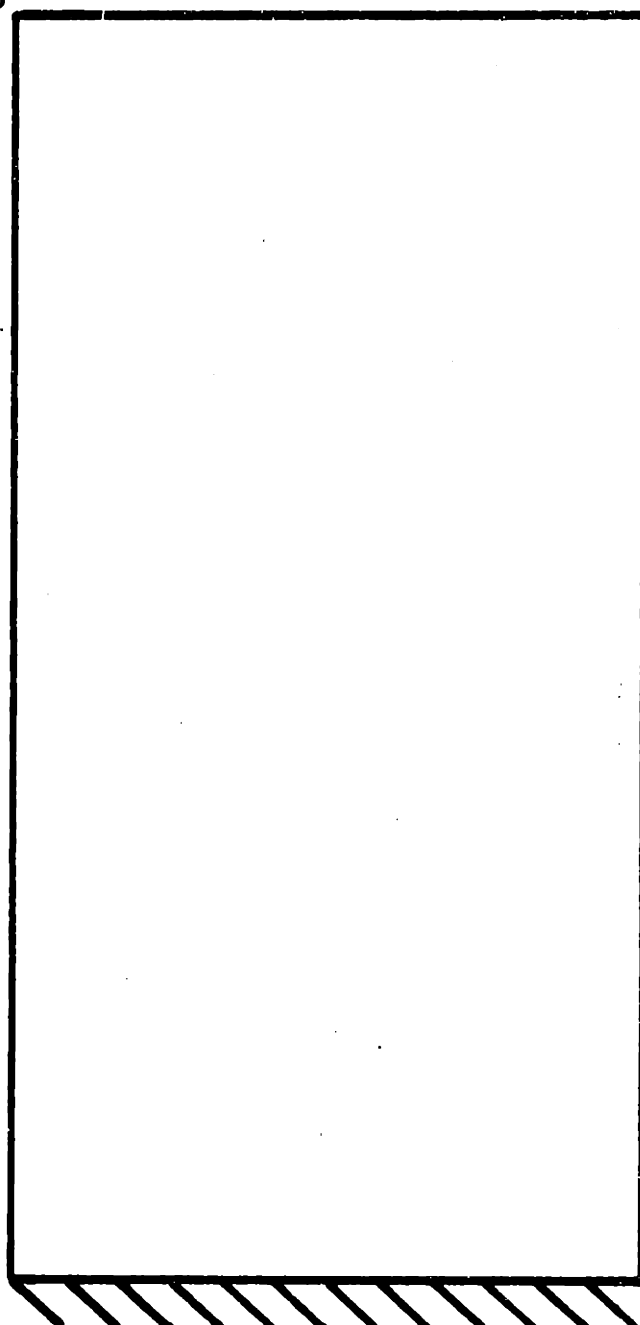
1306 Hz

FIG. 54 3rd BENDING (5th) MODE OF A
 $[0/+45/90/A1]_s$ PLATE



CALCULATED MODE SHAPE

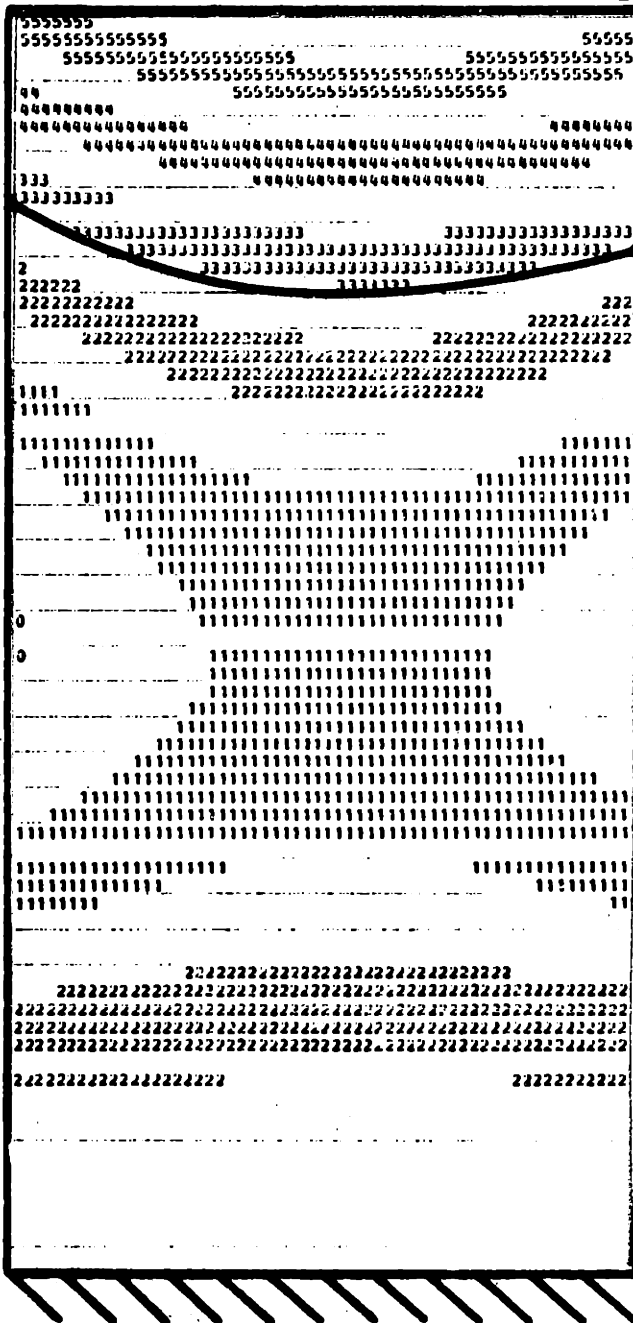
67.32 Hz



OBSERVED MODE SHAPE

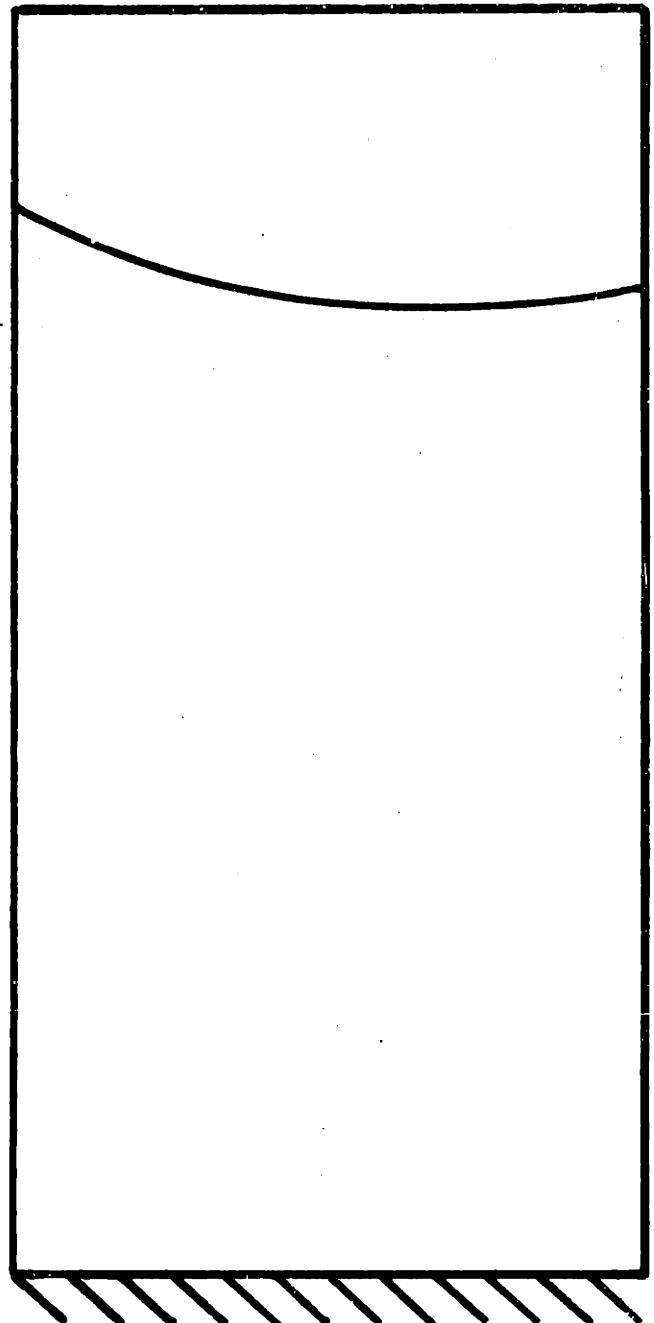
58.3 Hz

FIG. 55 1st BENDING (1st) MODE OF A
[+45/-45/A1]₈ PLATE



CALCULATED MODE SHAPE

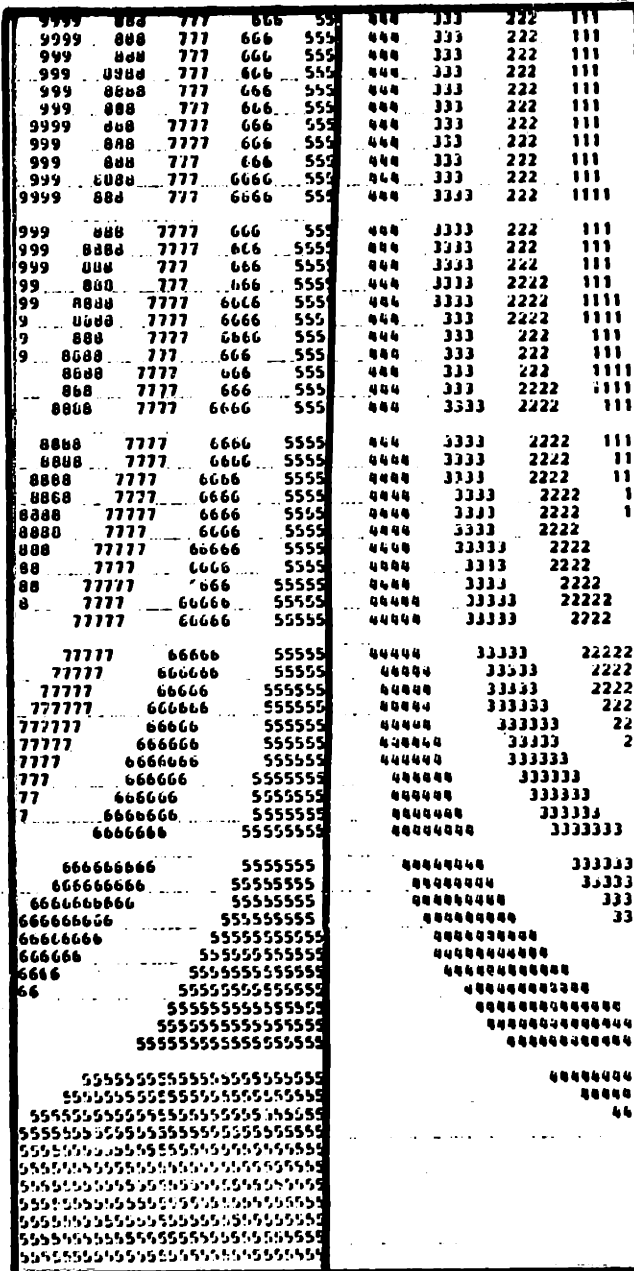
355.9 Hz



OBSERVED MODE SHAPE

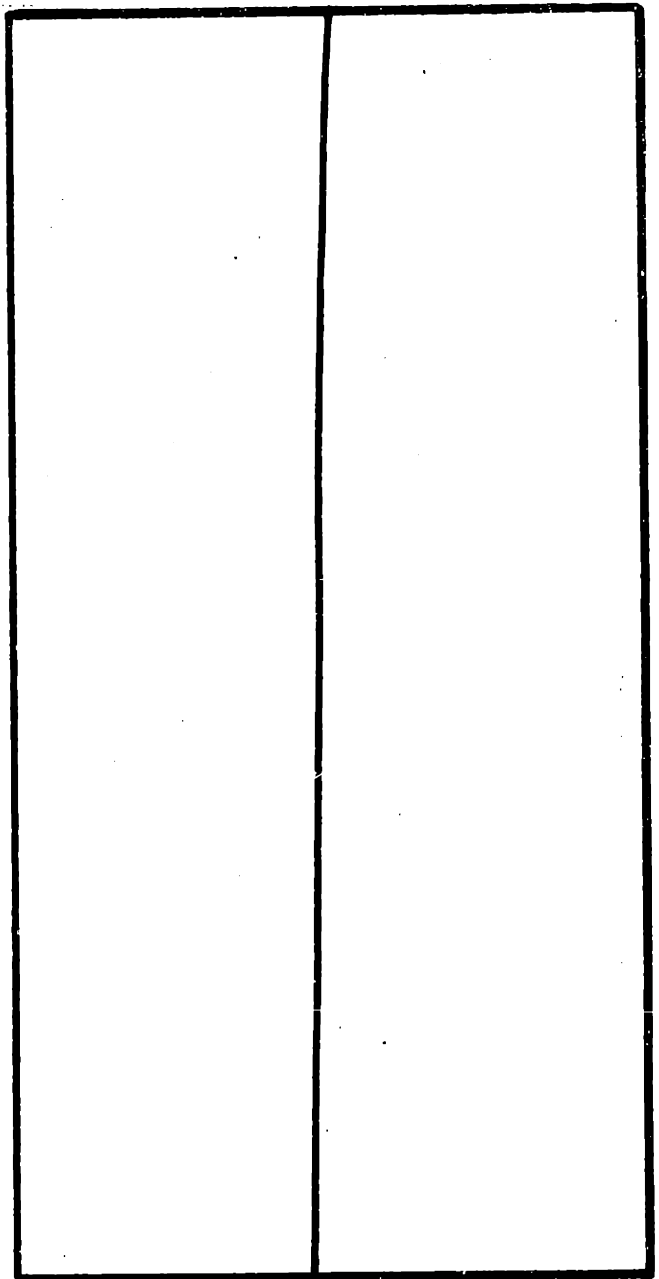
351.6 Hz

FIG. 56 2nd BENDING (2nd) MODE OF A
 $[+45/\bar{+45}/A1]_8$ PLATE



CALCULATED MODE SHAPE

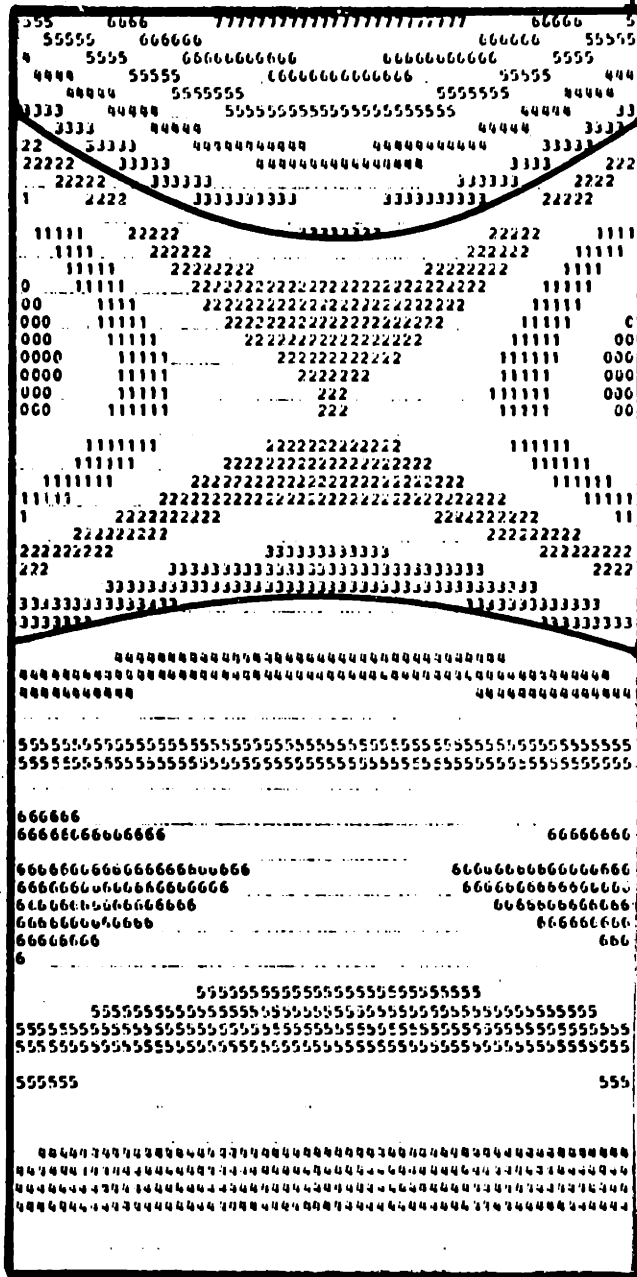
380.2 Hz



OBSERVED MODE SHAPE

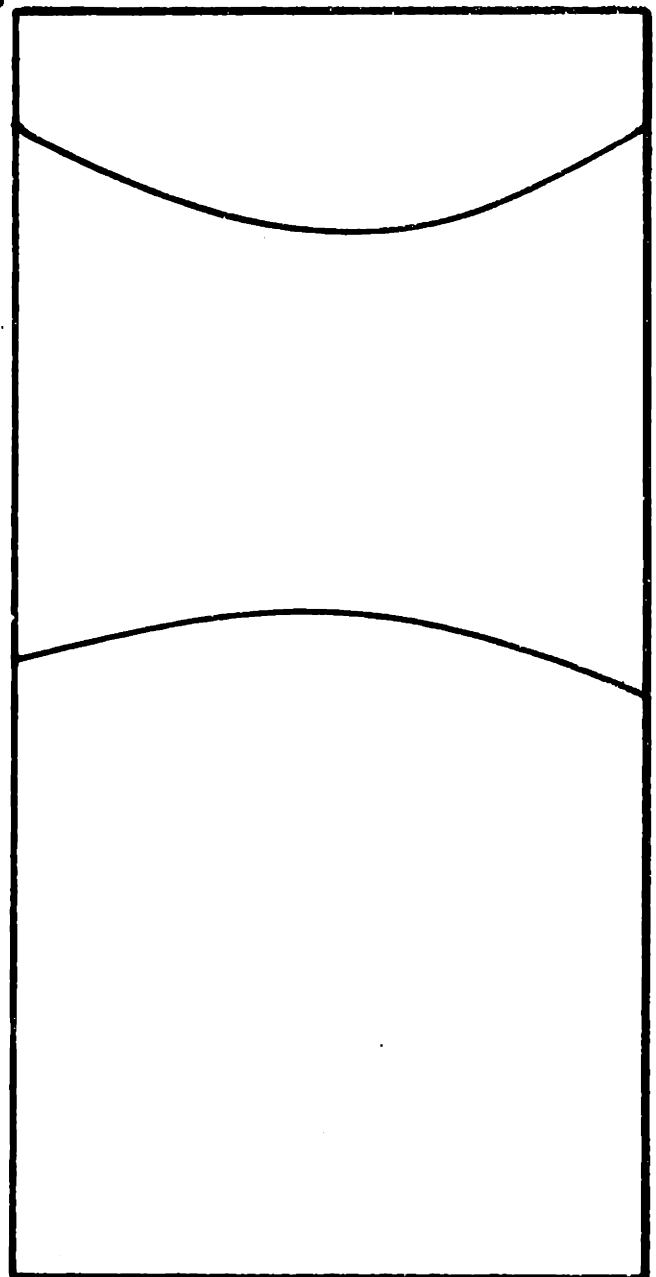
358. Hz

FIG. 57 1st TORSION (3rd) MODE OF A
 $[+45/-45/A1]_s$ PLATE



CALCULATED MODE SHAPE

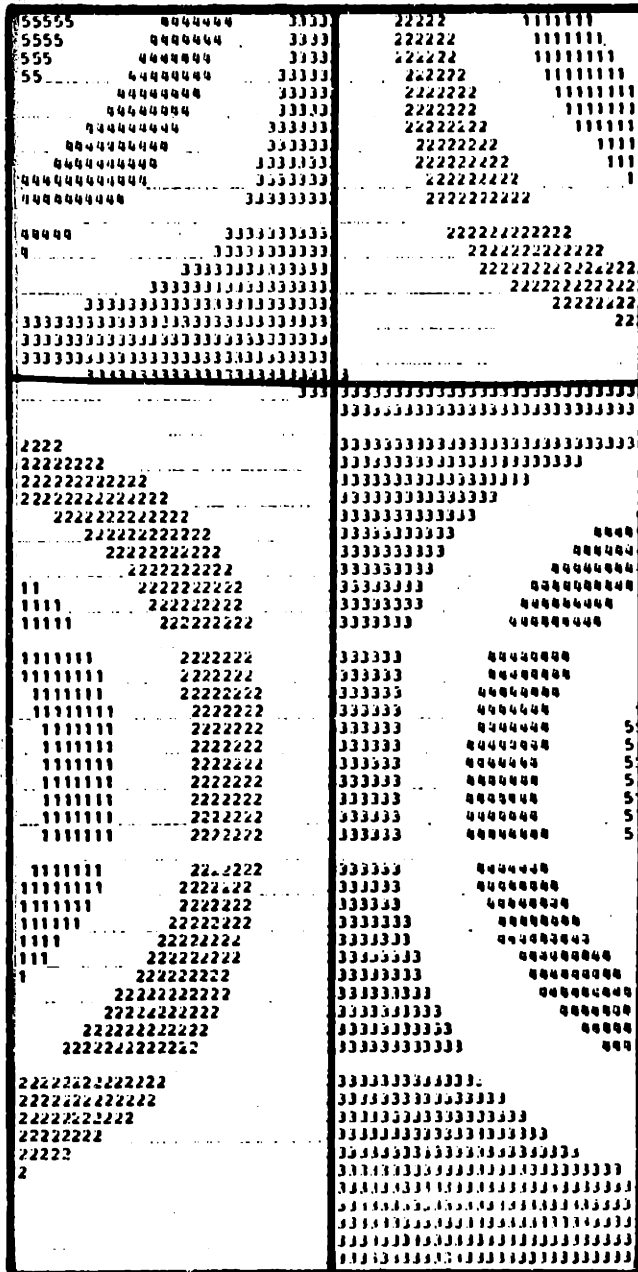
1029. Hz



OBSERVED MODE SHAPE

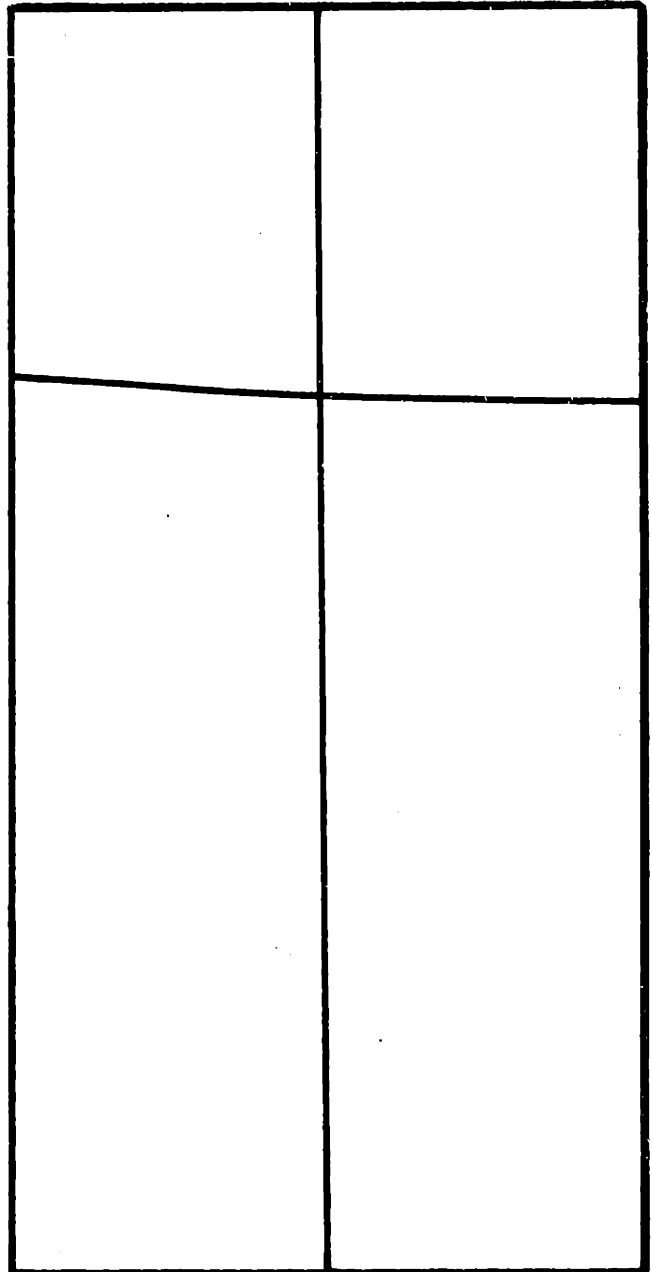
1006. Hz

FIG. 58 3rd BENDING (4th) MODE OF A
 $[+45/\bar{45}/A1]_s$ PLATE



CALCULATED MODE SHAPE

1187. Hz

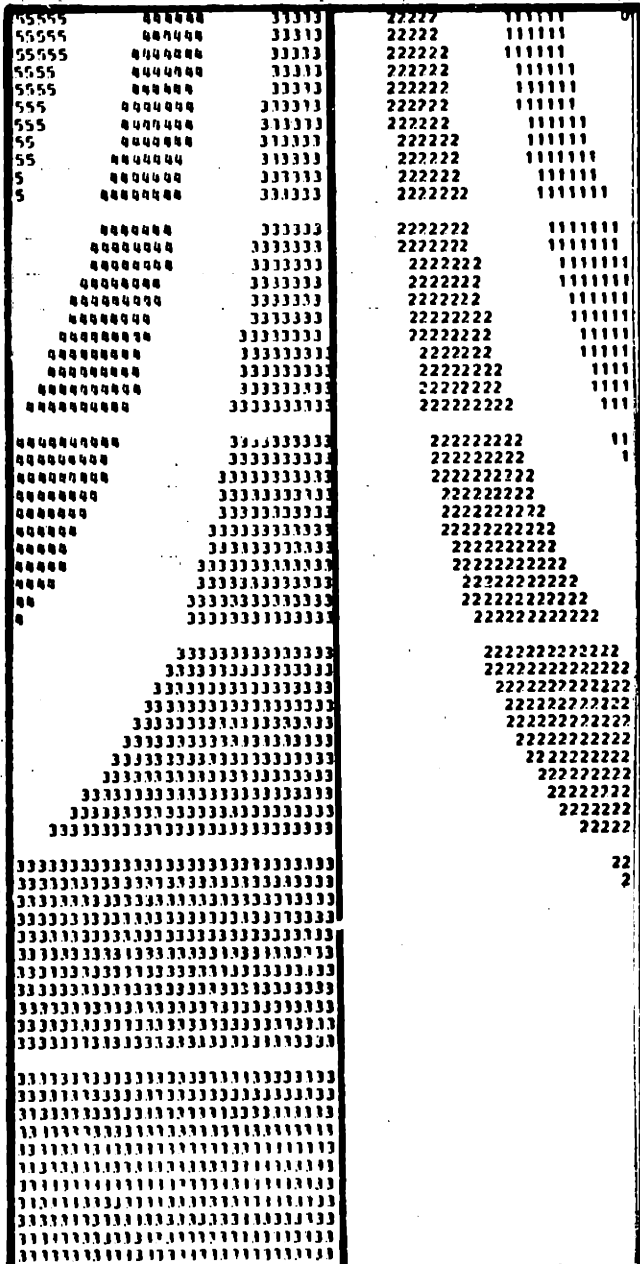


OBSERVED MODE SHAPE

1113. Hz

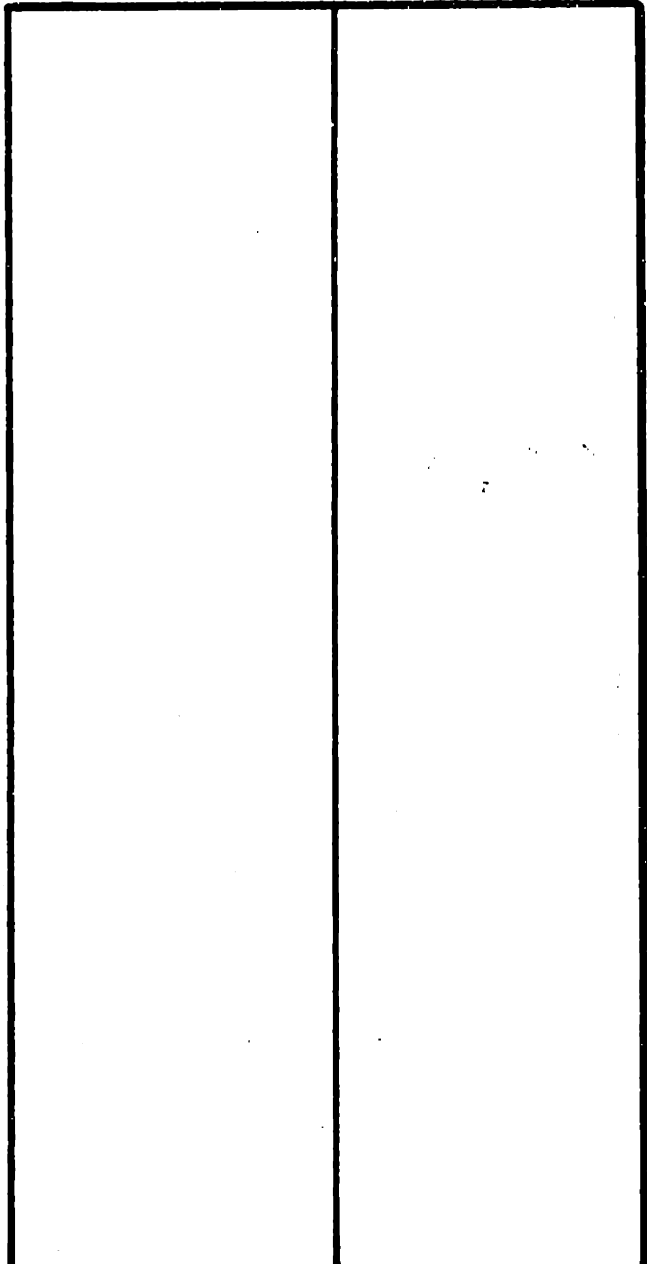
FIG. 59 2nd TORSION (5th) MODE OF A

[+45/-45/A1]_s PLATE



CALCULATED MODE SHAPE

169.9 Hz

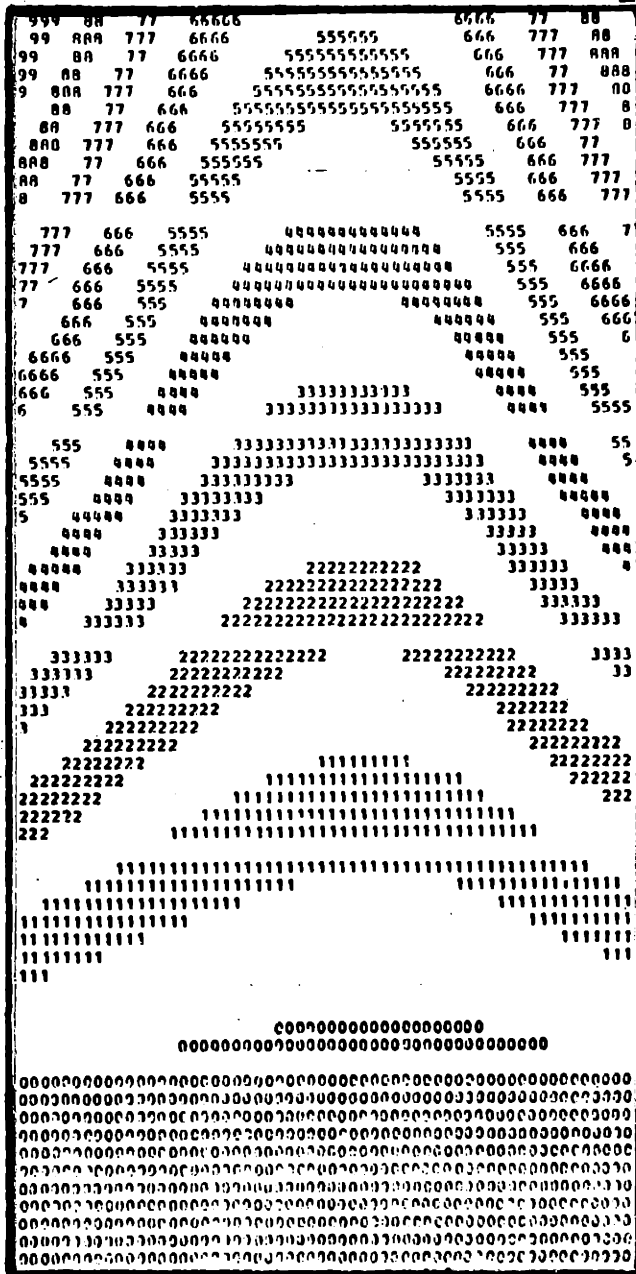


OBSERVED MODE SHAPE

161. Hz

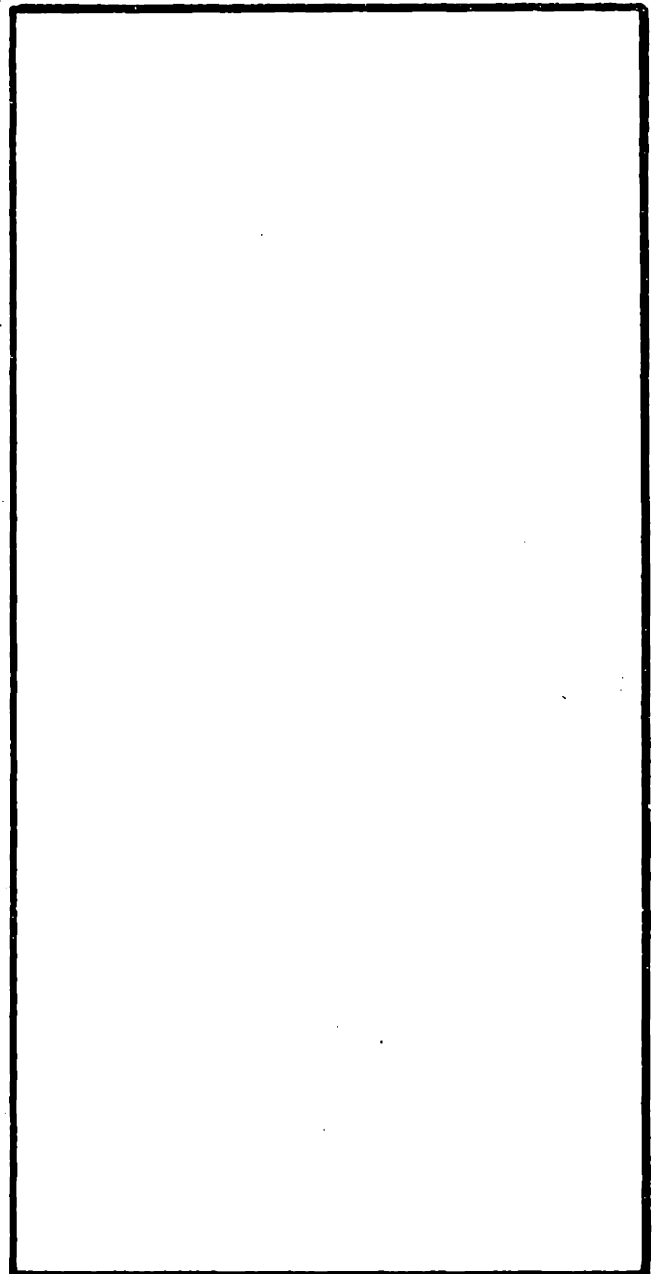
FIG. 60 1st TORSION (1st) MODE OF A

[0₂/+30]_s SHELL SECTION



CALCULATED MODE SHAPE

291.6 Hz

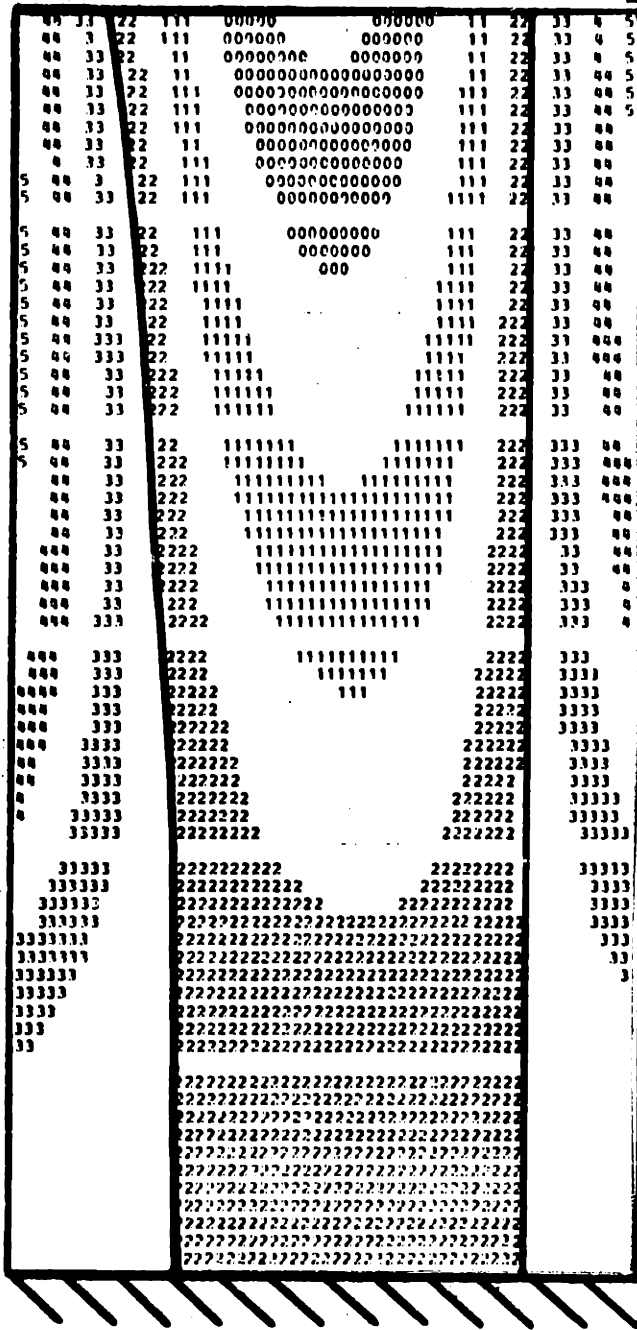


OBSERVED MODE SHAPE

254.1 Hz

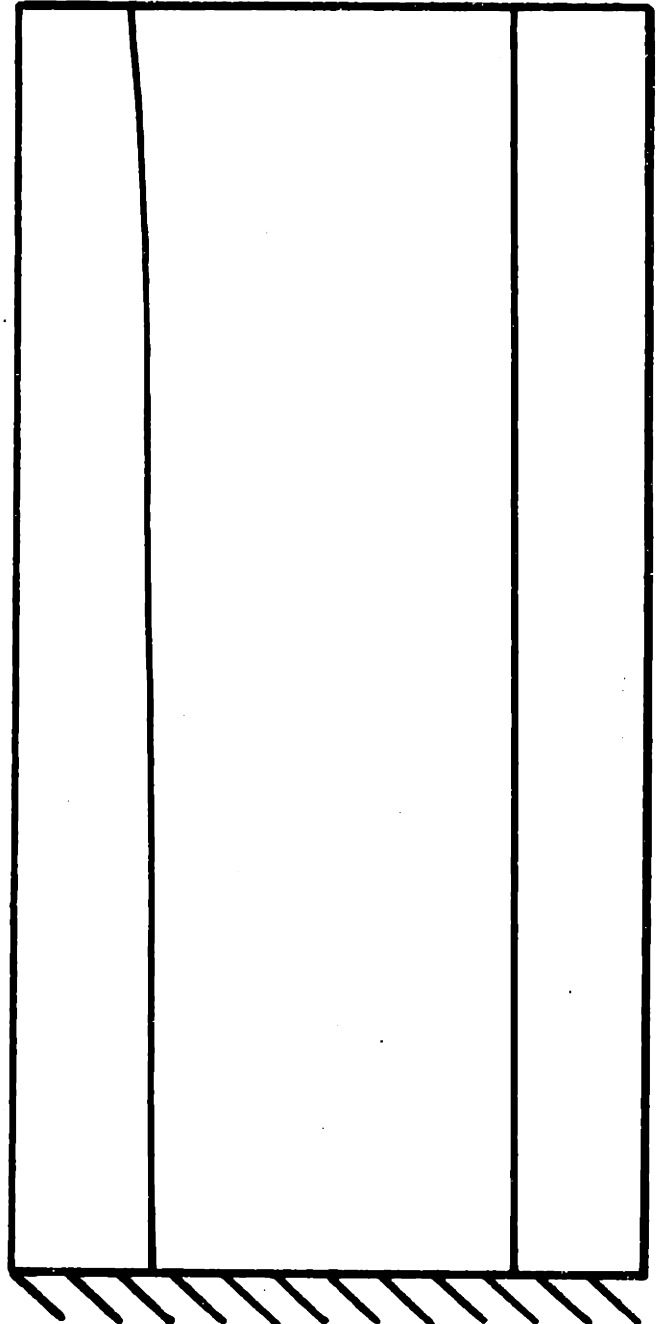
FIG. 61 1st BENDING (2nd) MODE OF A

[0₂/+30]_s SHELL SECTION



CALCULATED MODE SHAPE

597.2 Hz

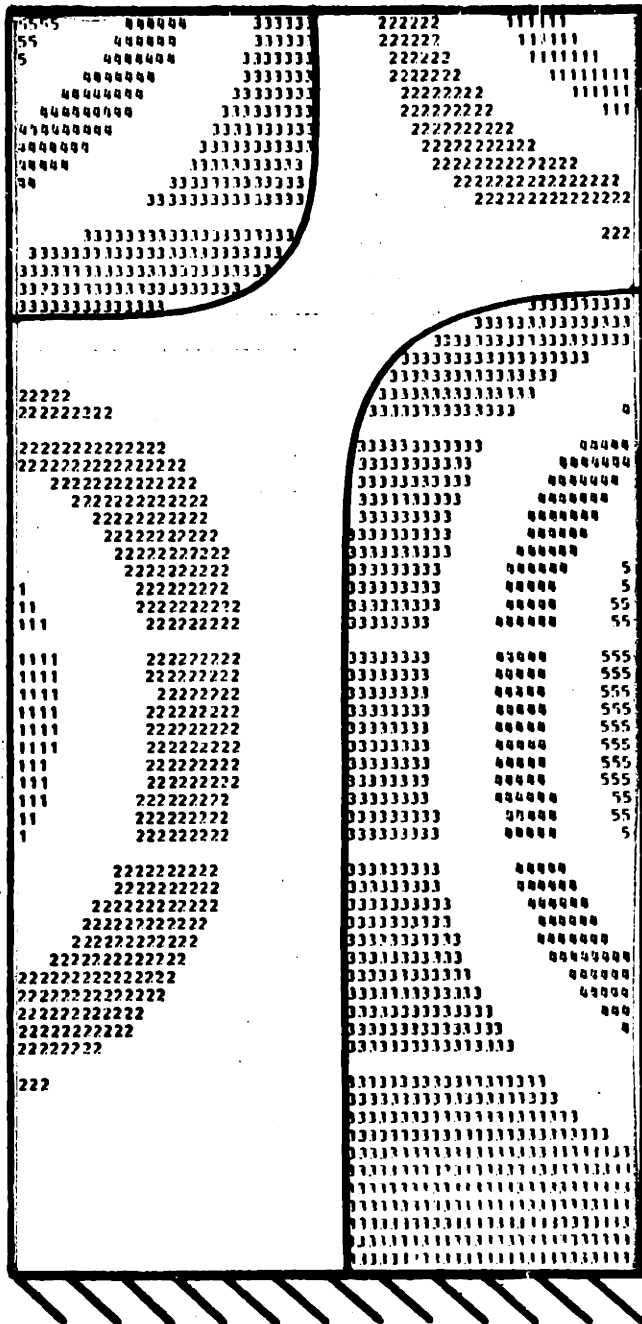


OBSERVED MODE SHAPE

555.6 Hz

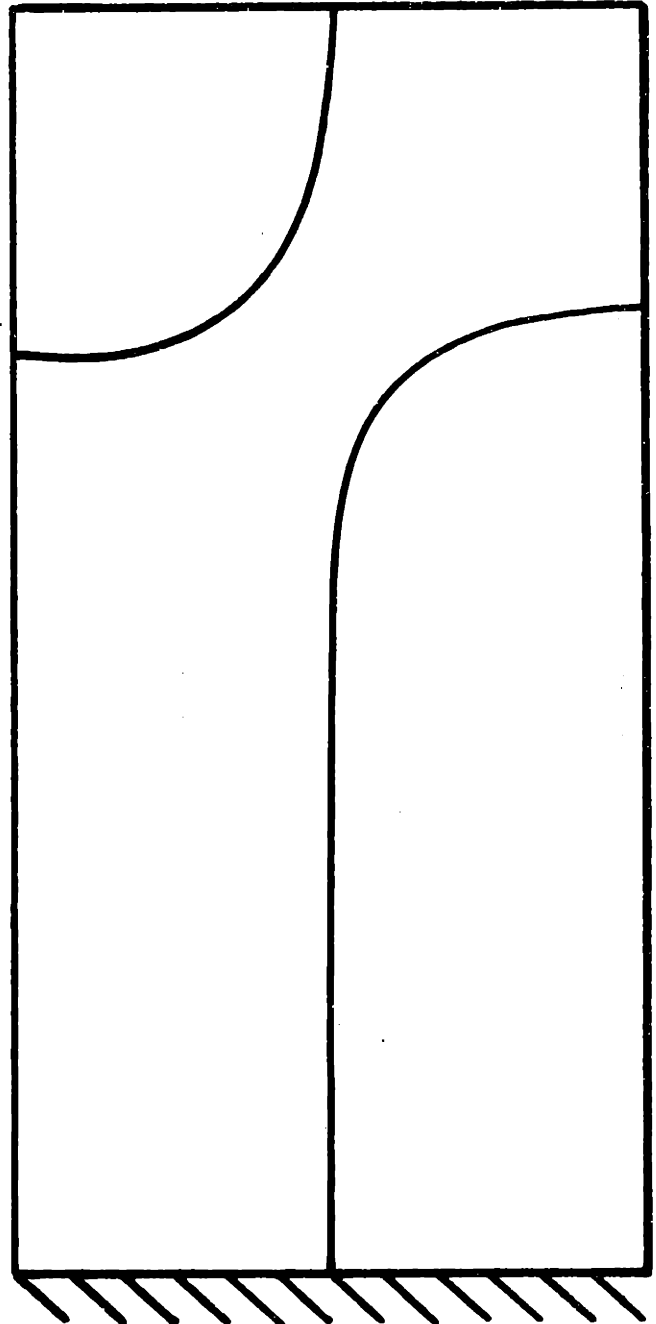
FIG. 62 1st CHORDWISE (3rd) MODE OF A

[0₂/+30]_s SHELL SECTION



CALCULATED MODE SHAPE

719.5 Hz

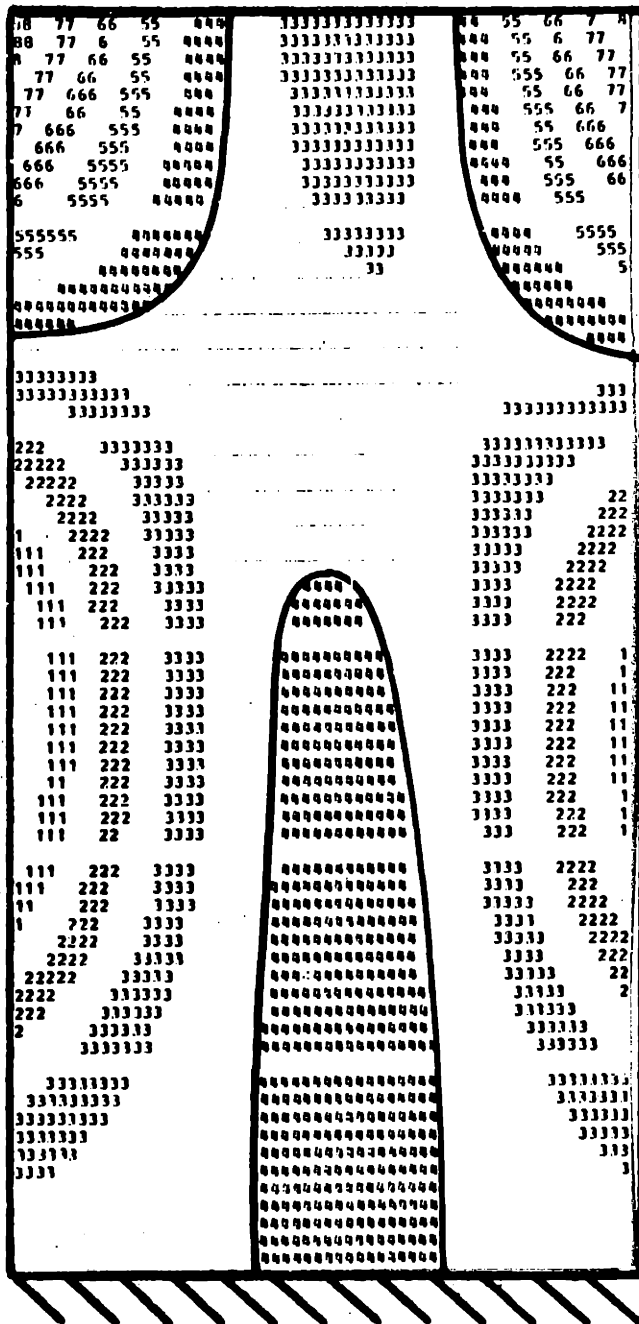


OBSERVED MODE SHAPE

670.0 Hz

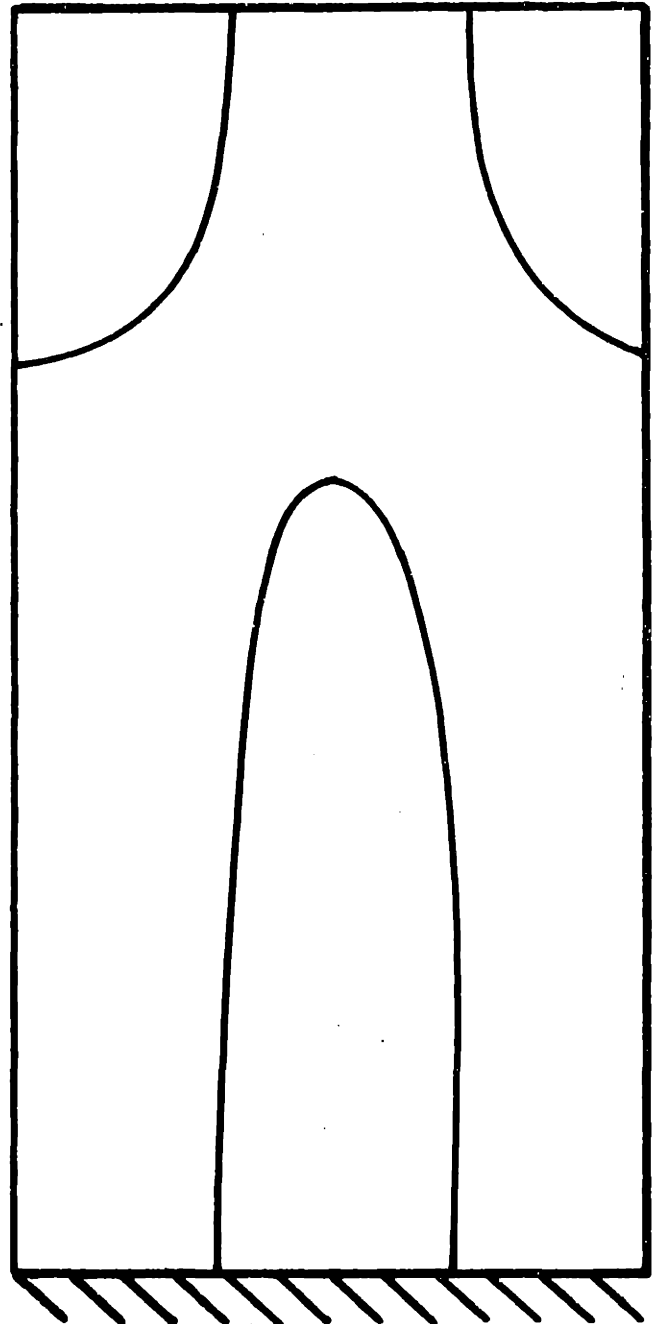
FIG. 63 2nd TORSION (4th) MODE OF A

[0₂/+30]_s SHELL SECTION



CALCULATED MODE SHAPE

834.0 Hz

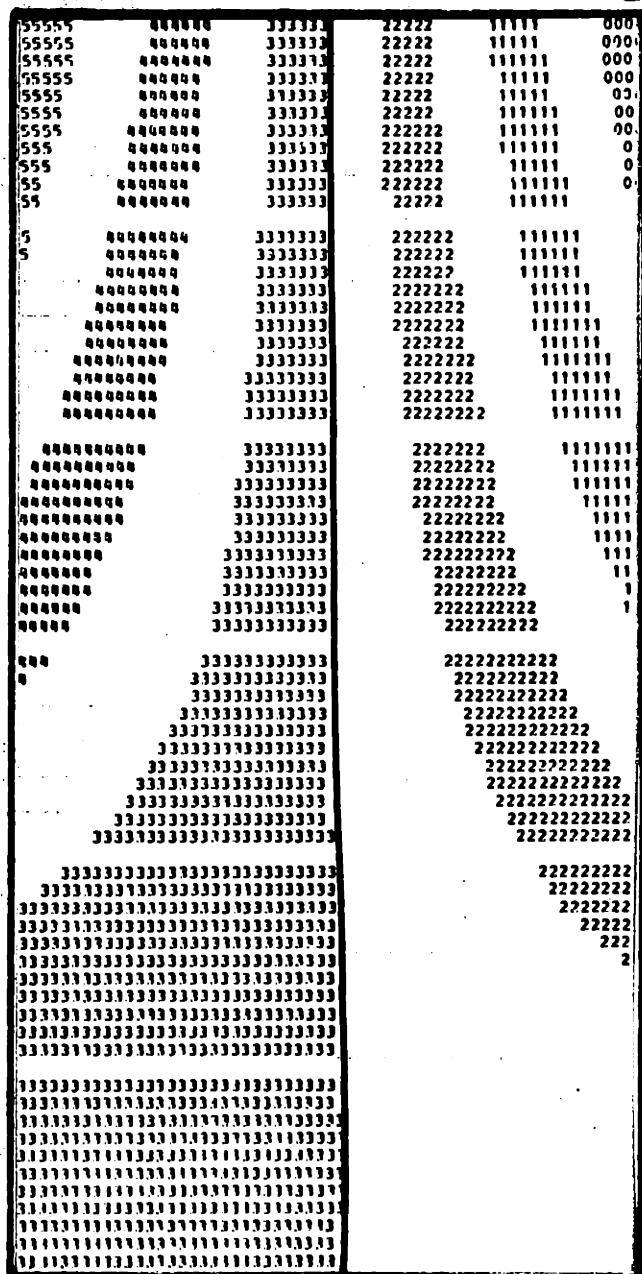


OBSERVED MODE SHAPE

794. Hz

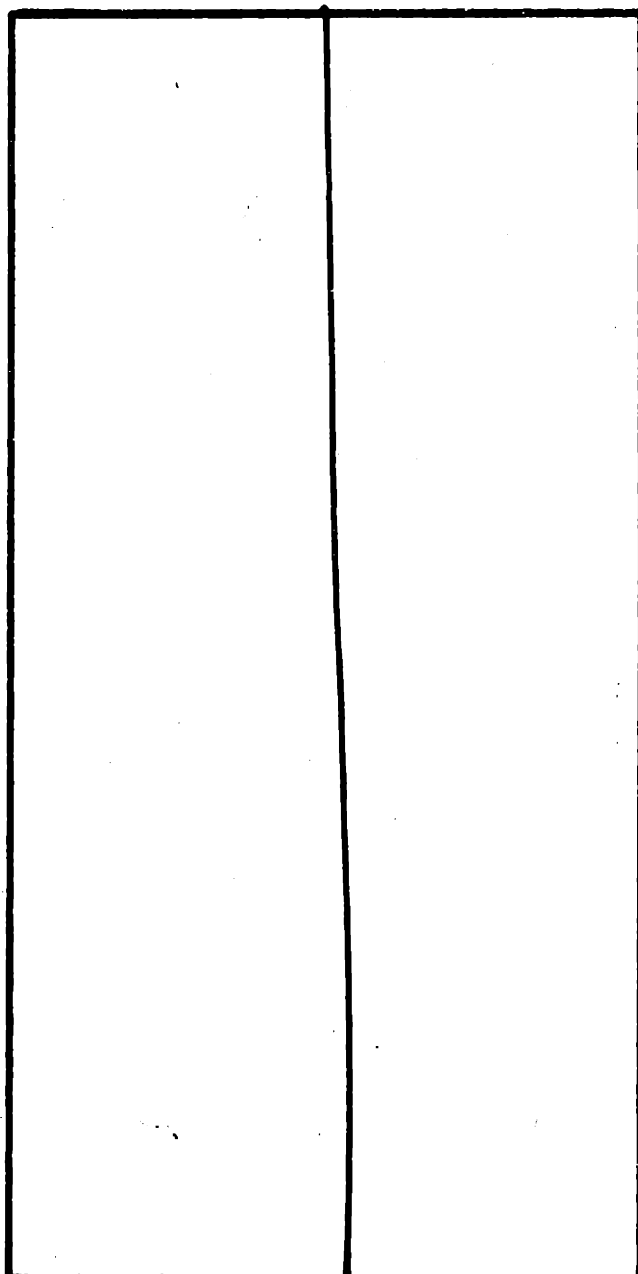
FIG. 64 5th MODE OF A $[0_2/+30]_s$

SHELL SECTION



CALCULATED MODE SHAPE

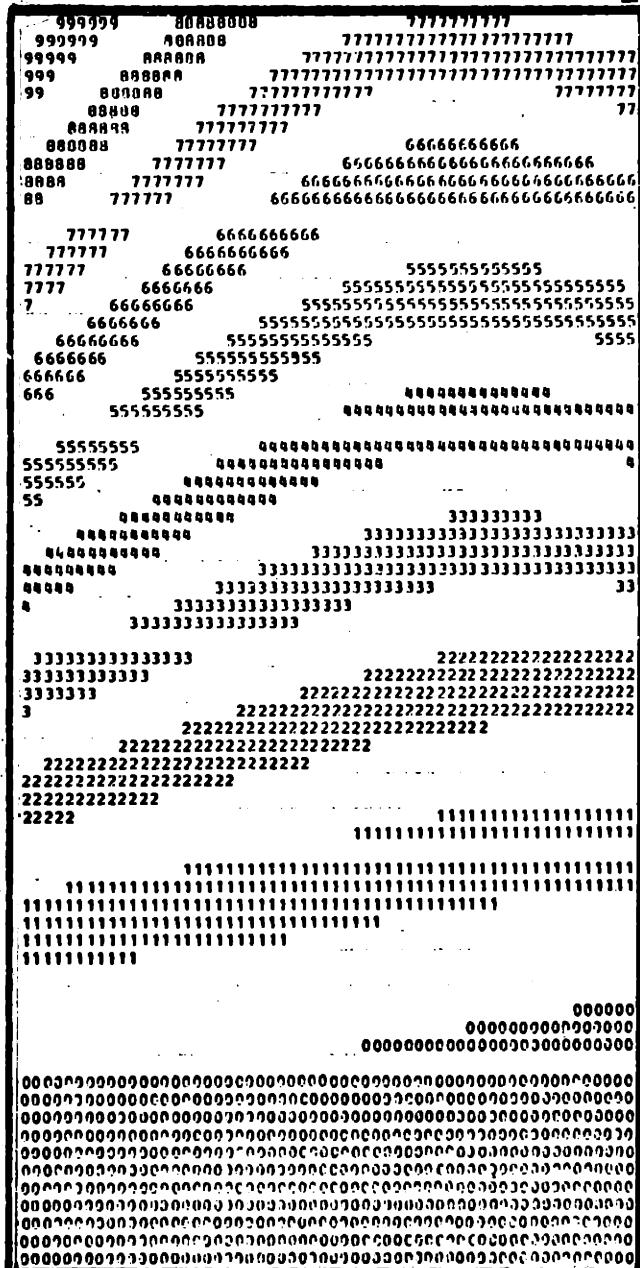
182.2 Hz



OBSERVED MODE SHAPE

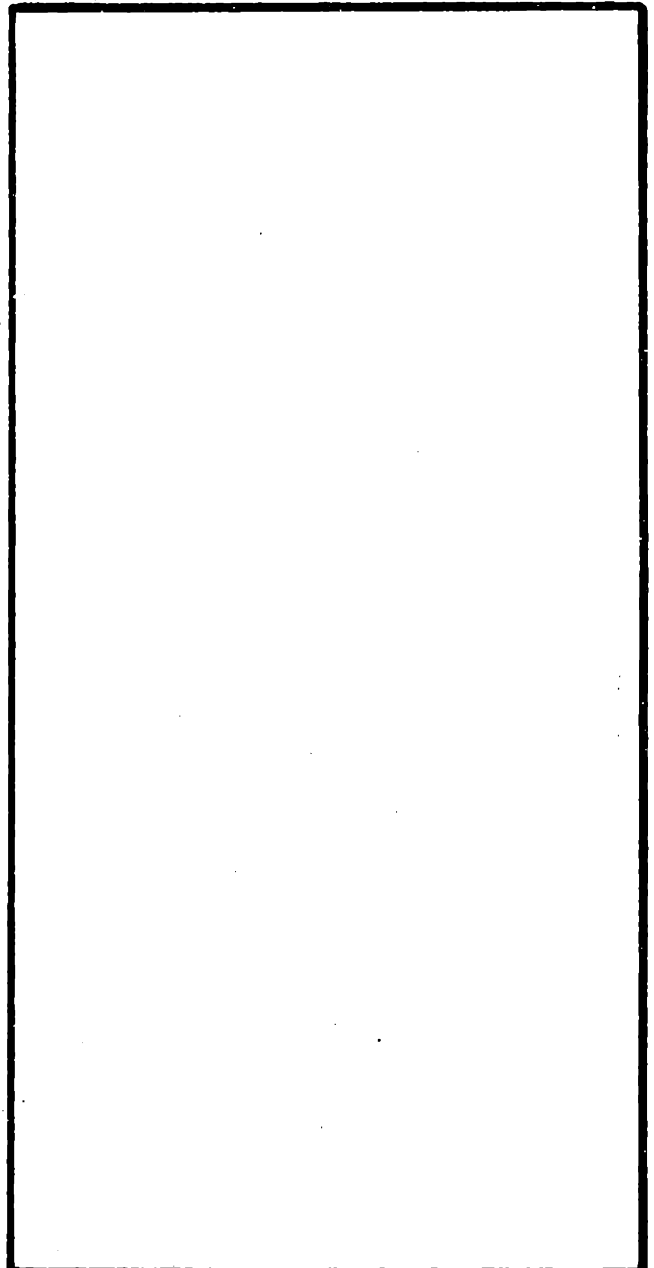
177. Hz

FIG. 65 1st TORSION (1st) MODE OF A
 $[0/+45/90]_8$ SHELL SECTION



CALCULATED MODE SHAPE

231.2 Hz

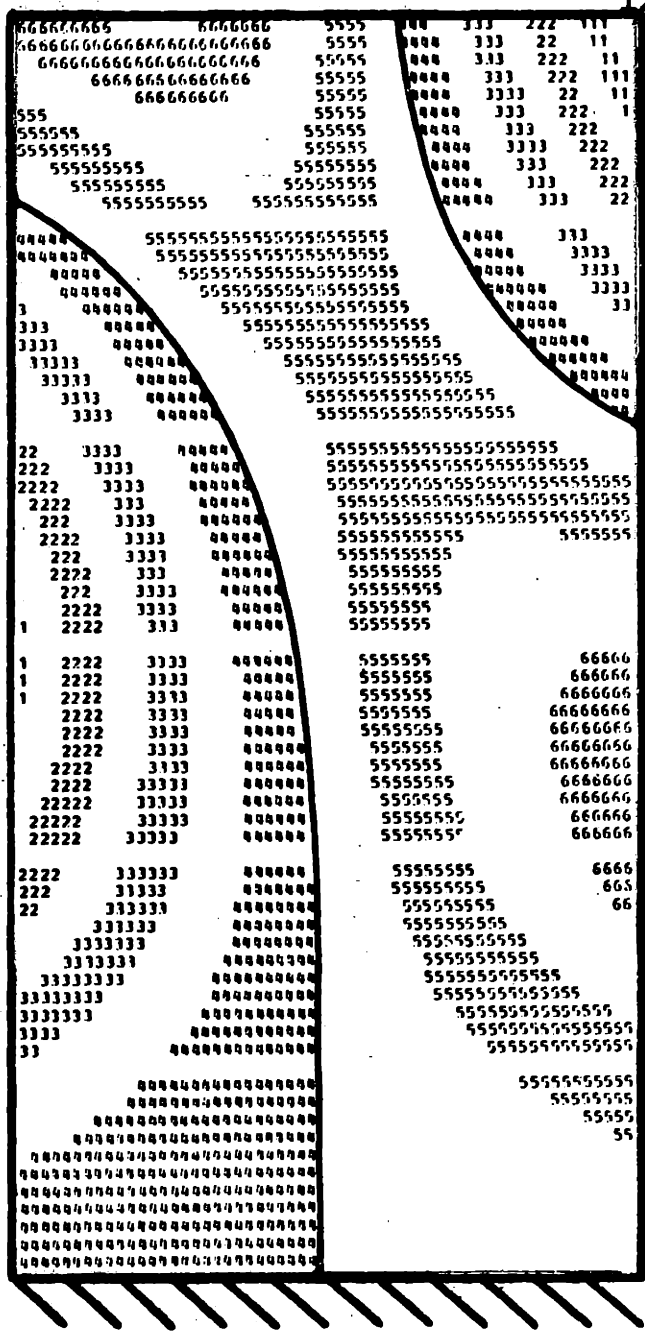


OBSERVED MODE SHAPE

201.8 Hz

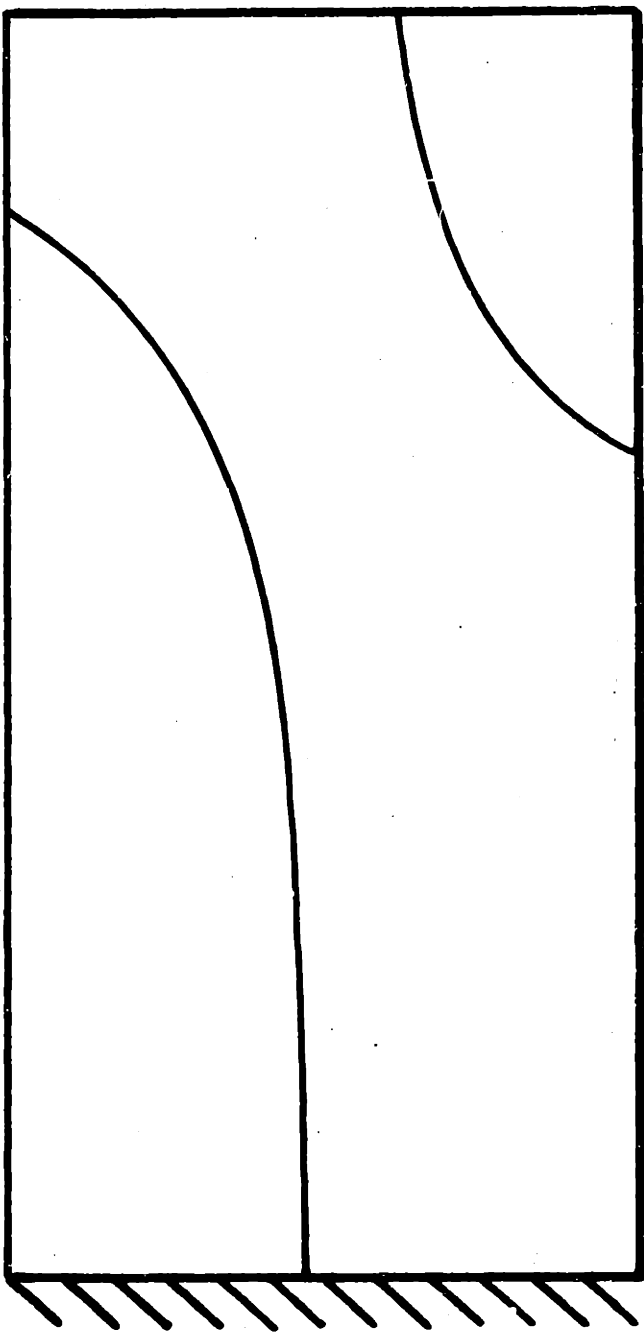
FIG. 66 1st BENDING (2nd) MODE OF A

[0/+45/90]_s SHELL SECTION



CALCULATED MODE SHAPE

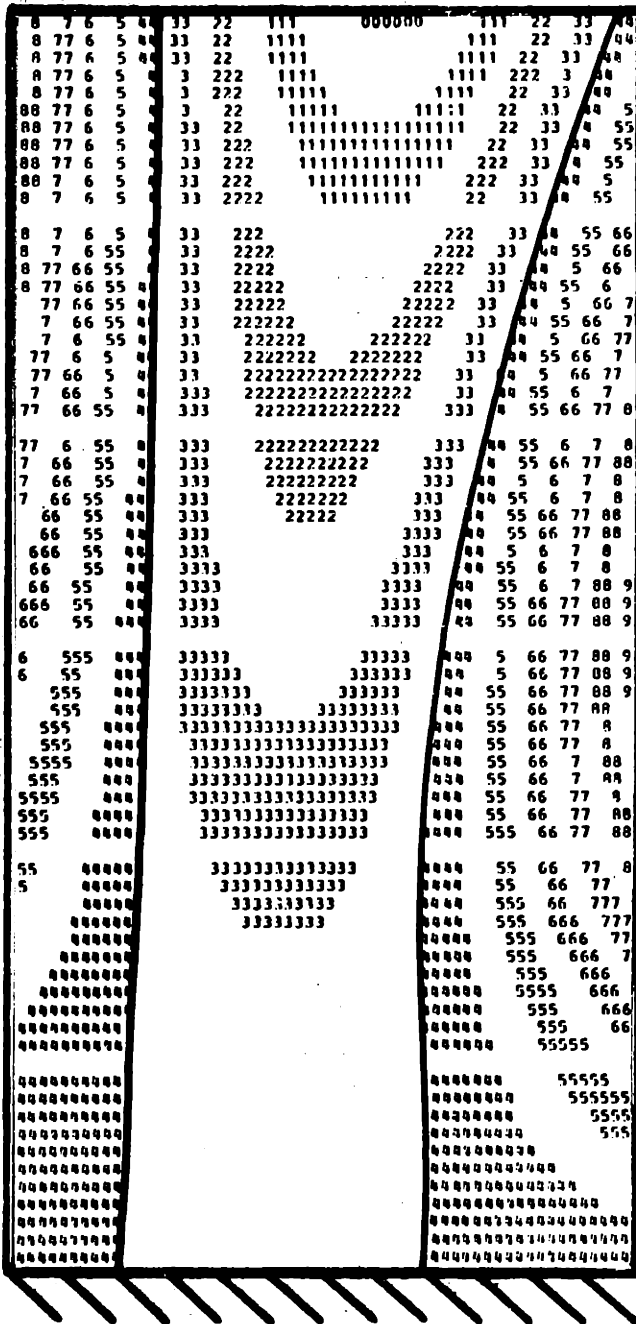
703.6 Hz



OBSERVED MODE SHAPE

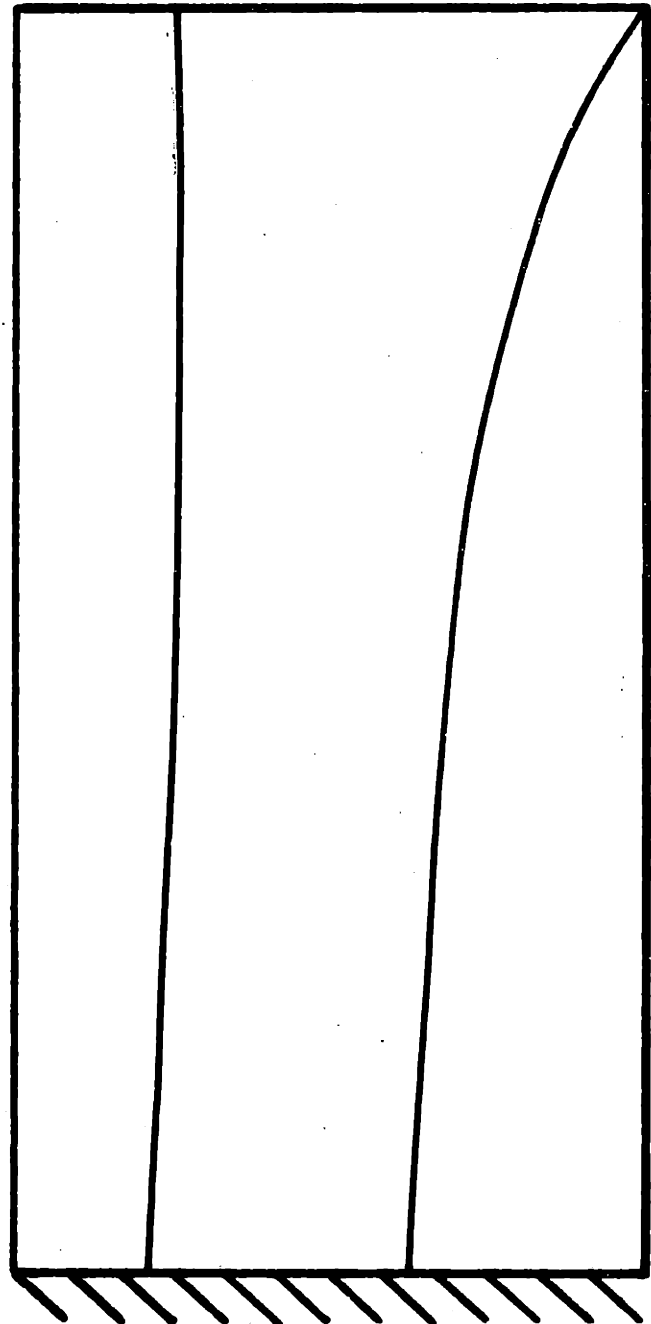
645. Hz

FIG. 67 2nd TORSION (3rd) MODE OF A
[0/+45/90]_s SHELL SECTION



CALCULATED MODE SHAPE

809.5 Hz

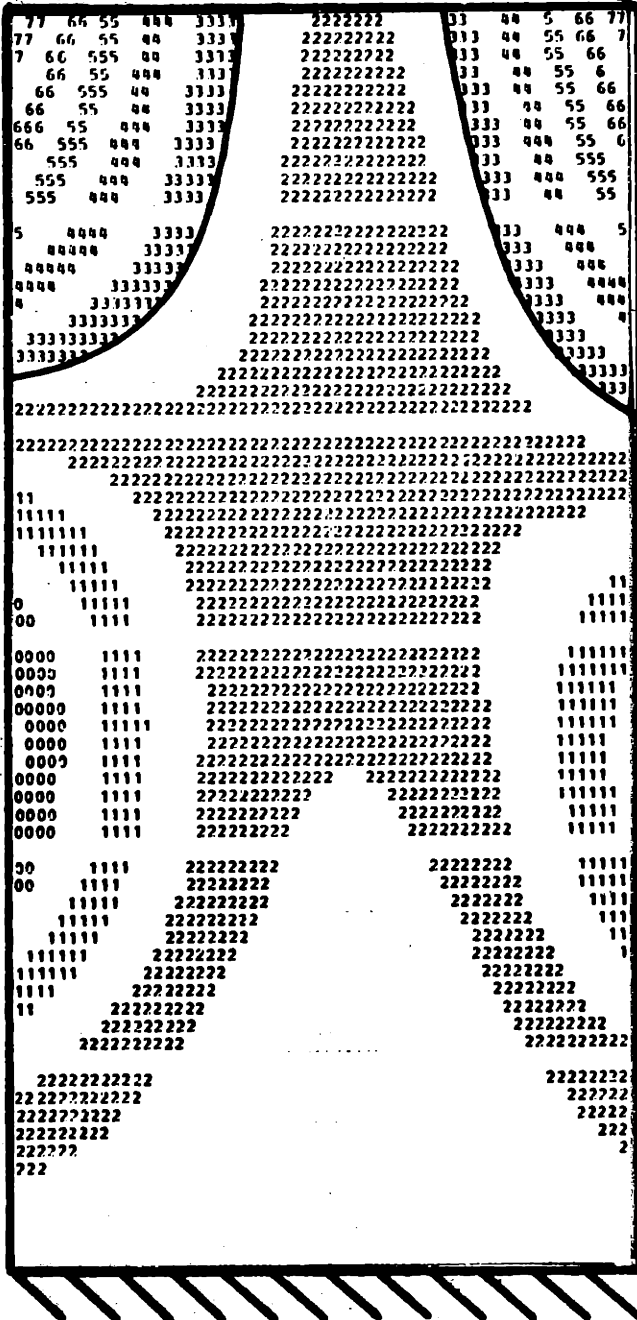


OBSERVED MODE SHAPE

754. Hz

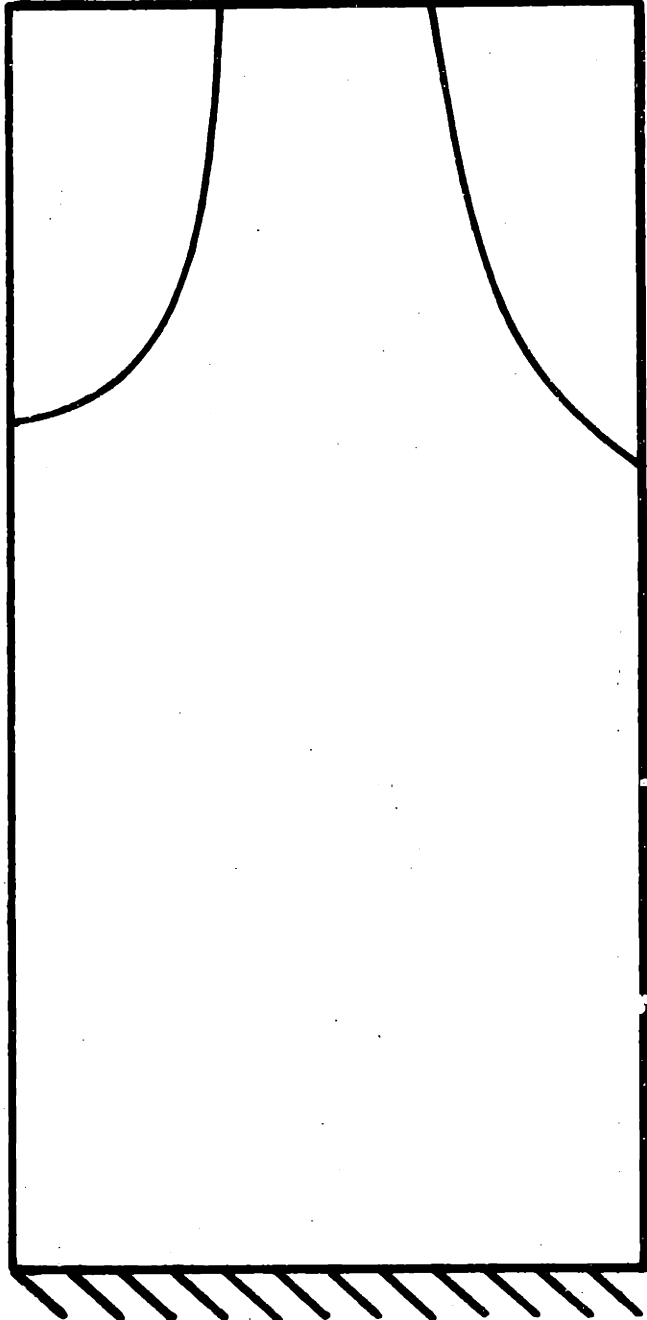
FIG. 68 1st CHORDWISE (4th) MODE OF A

[0/±45/90]_s SHELL SECTION



CALCULATED MODE SHAPE

980.1 Hz

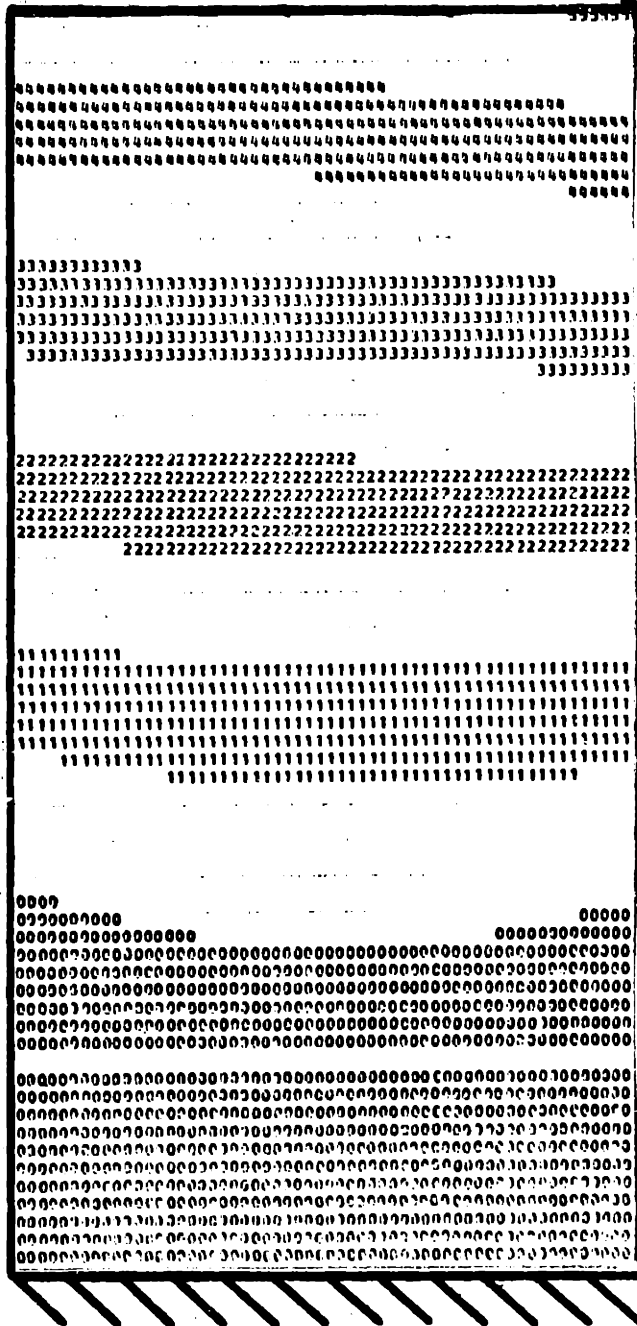


OBSERVED MODE SHAPE

884.8 Hz

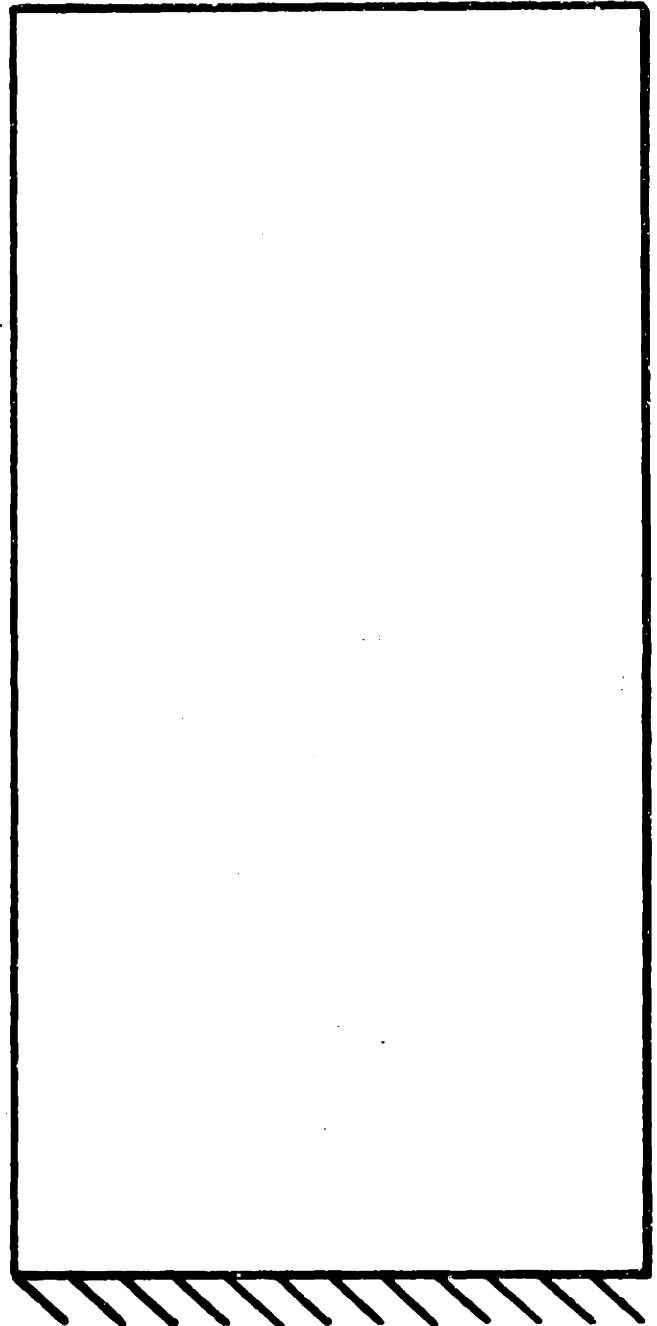
FIG. 69 5th MODE OF A $[0/_{\pm}45/90]_S$

SHELL SECTION



CALCULATED MODE SHAPE

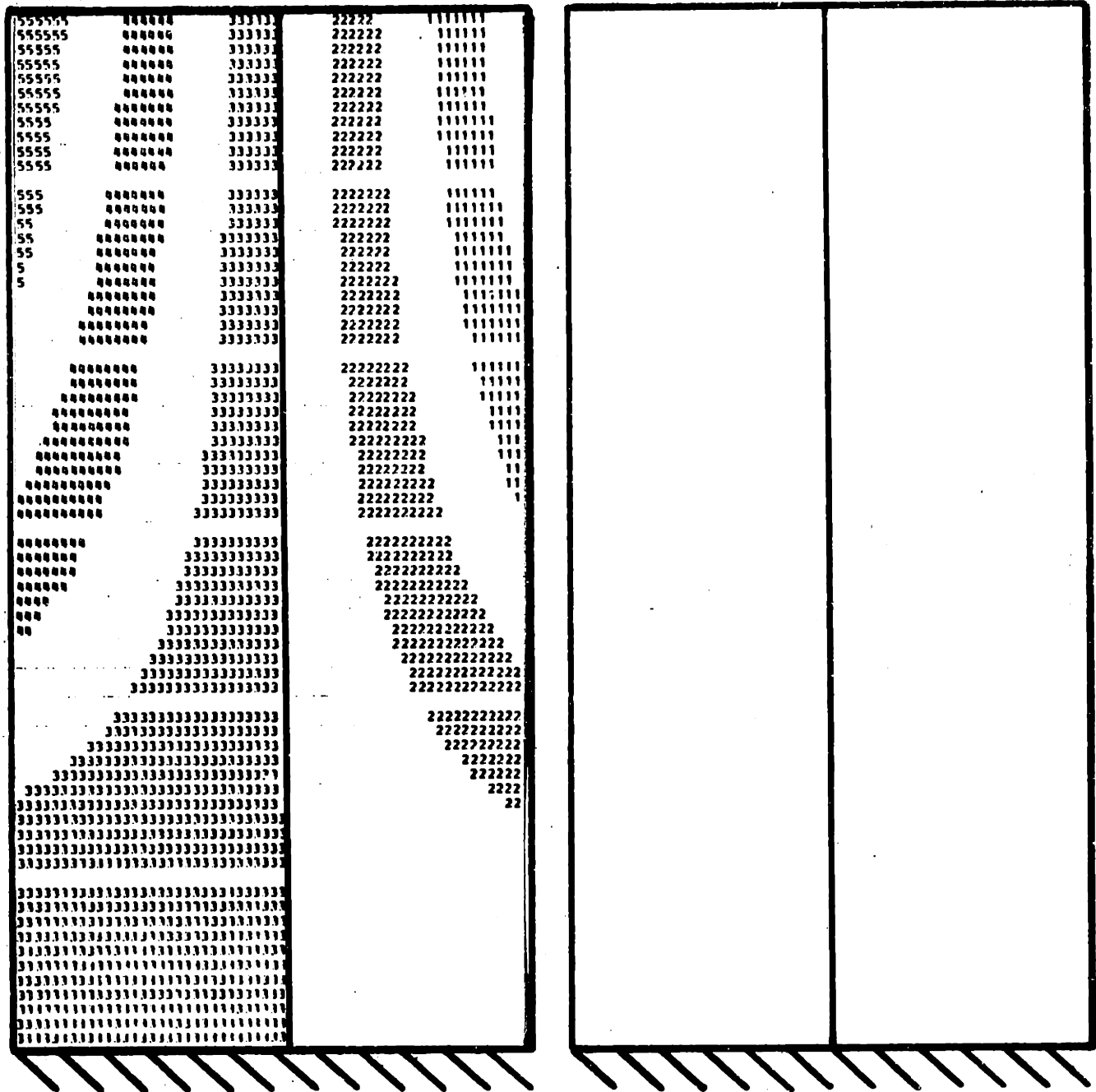
144.7 Hz



OBSERVED MODE SHAPE

145.3 Hz

FIG. 70 1st BENDING (1st) MODE OF A
 $[+45/-45]_s$ SHELL SECTION



CALCULATED MODE SHAPE

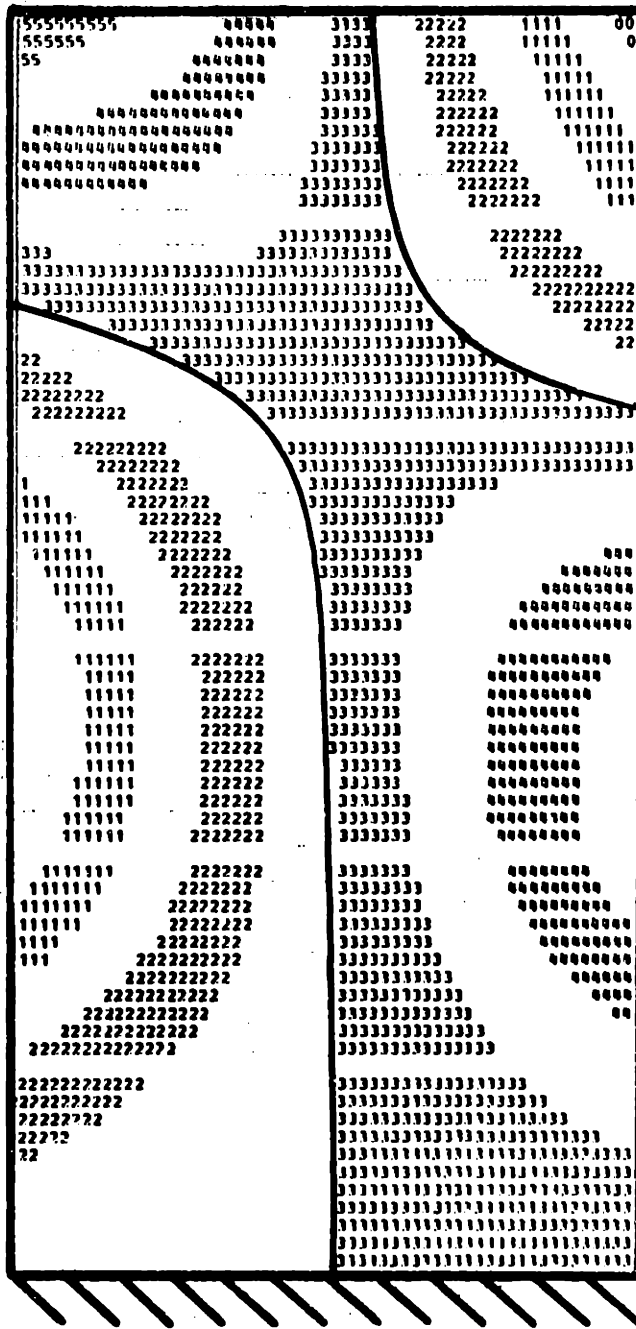
248.3 Hz

OBSERVED MODE SHAPE

222. Hz

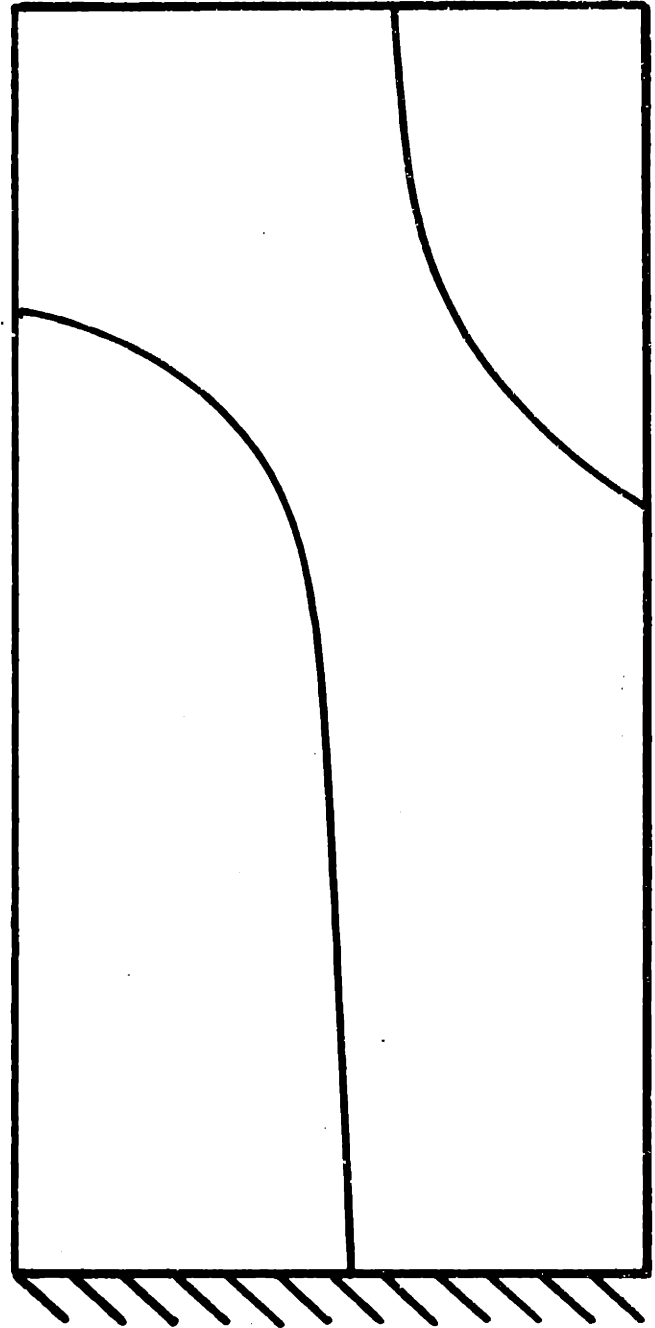
FIG. 71 1st TORSION (2nd) MODE OF A

[+45/-45]_s SHELL SECTION



CALCULATED MODE SHAPE

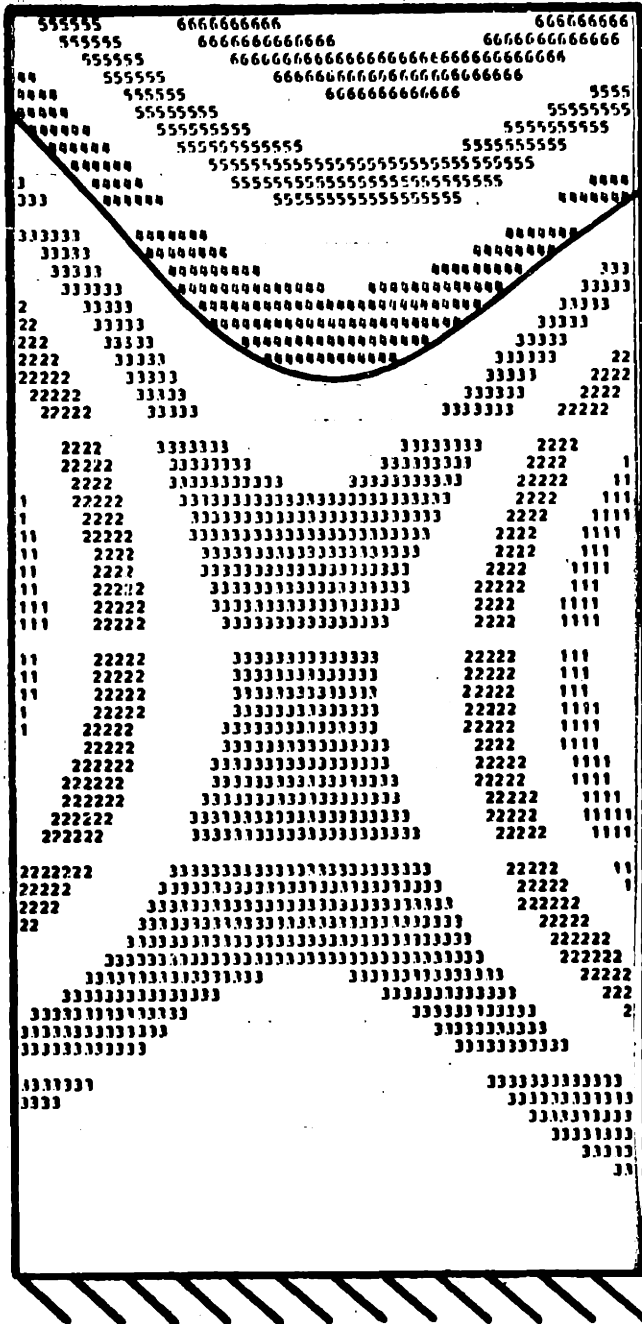
770.8 Hz



OBSERVED MODE SHAPE

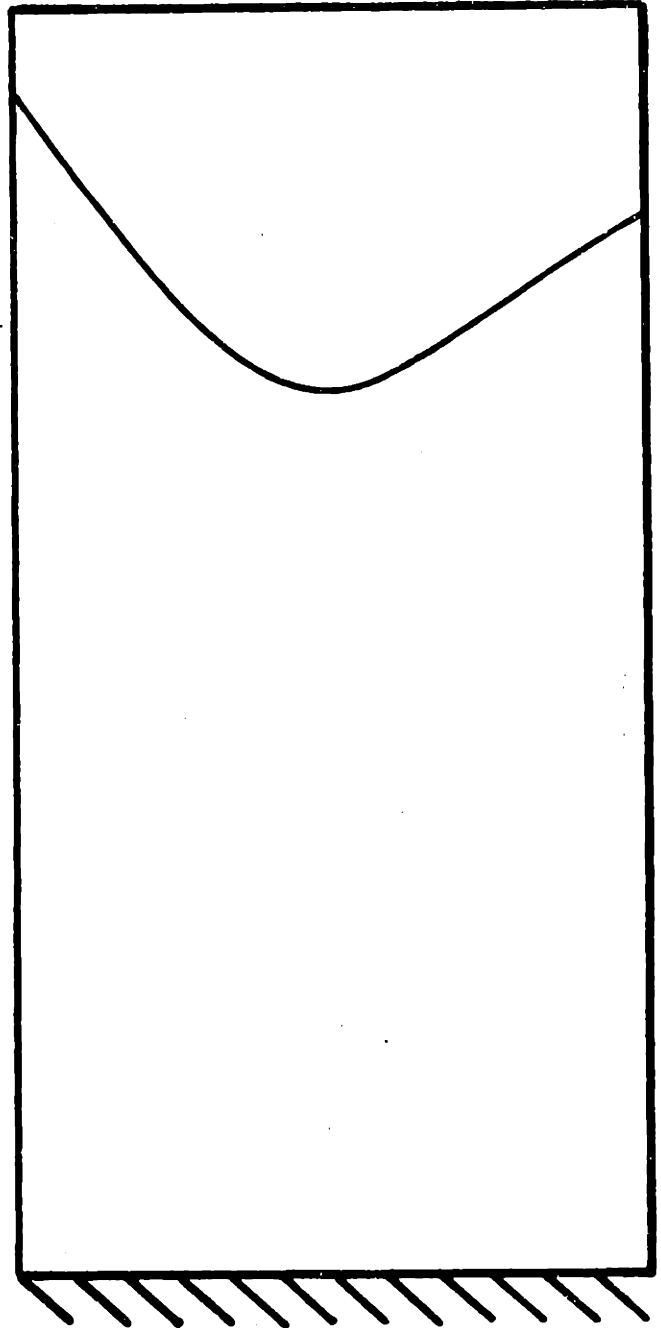
712. Hz

FIG. 72 2nd TORSION (3rd) MODE OF A
 $[+45/-45]_s$ SHELL SECTION



CALCULATED MODE SHAPE

814.1 Hz

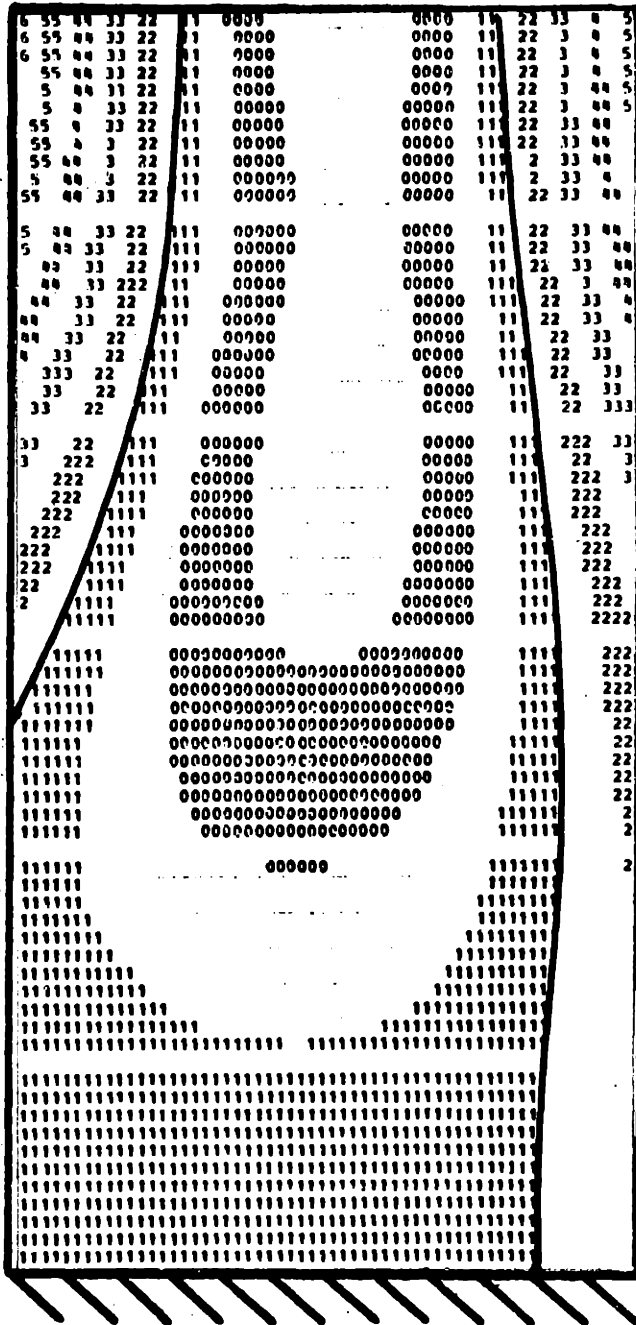


OBSERVED MODE SHAPE

774.2 Hz

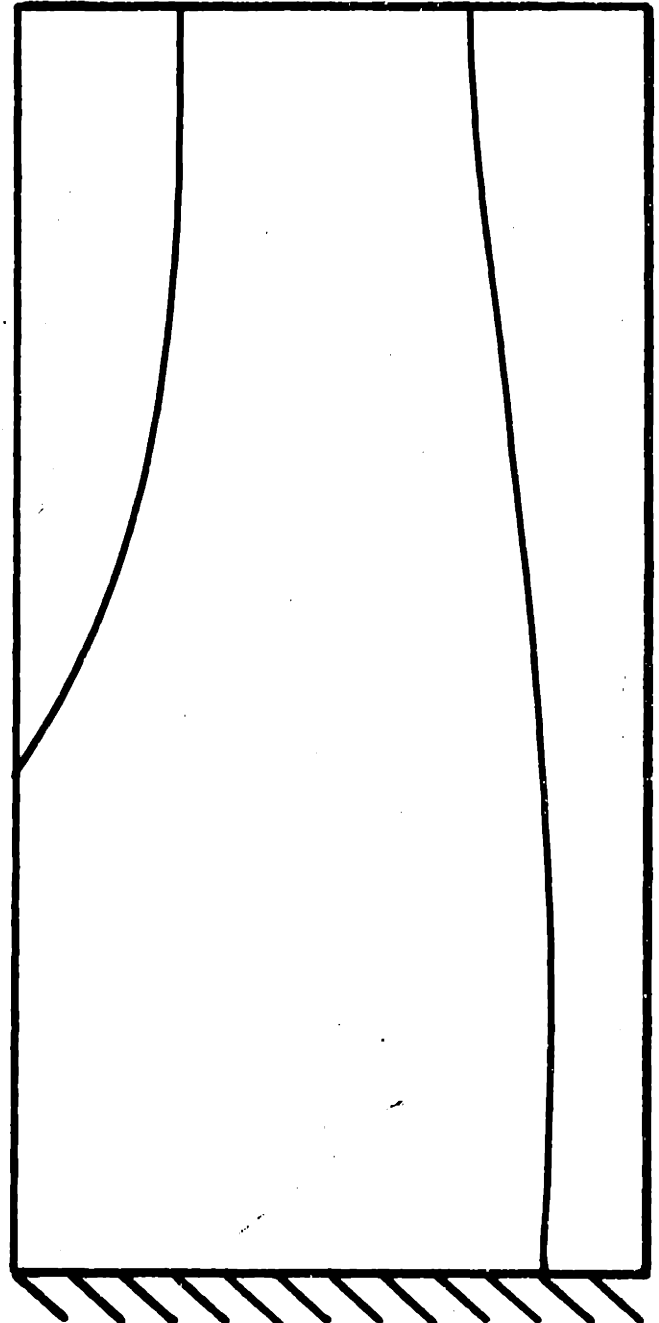
FIG. 73 2nd BENDING (4th) MODE OF A

[+45/-45]_s SHELL SECTION



CALCULATED MODE SHAPE

1042.5 Hz



OBSERVED MODE SHAPE

997. Hz

FIG. 74 1st CHORDWISE (5th) MODE OF A
 $[+45/\bar{+45}]_s$ SHELL SECTION